NEW TECHNIQUES FOR SUB-DOPPLER SPECTROSCOPY OF MOLECULAR IONS

BY

BRIAN M. SILLER

DISSERTATION

Submitted in partial fulfillment of the requirements
for the degree of Doctor of Philosophy in Chemistry
in the Graduate College of the
University of Illinois at Urbana-Champaign, 2013

Urbana, Illinois

Doctoral Committee:

Professor Benjamin McCall, Chair
Professor Martin Gruebele
Professor James Lisy
Professor Alexander Scheeline

Abstract

This thesis details research in developing new methods for performing high-resolution sub-Doppler spectroscopy of molecular ions in the laboratory. Molecular ions are of interest to a variety of fields, from astrochemistry to fundamental physics to the study of chemical reactive intermediates. The limiting factor in developing a deeper understanding of many ion systems is the quality of the available laboratory spectra. Traditional techniques for high-resolution spectroscopy of ions are limited by two factors: the precision is often limited by the Doppler-broadened linewidths of the observed spectra, and the accuracy is typically limited by the laser frequency calibration. Two new techniques are described in this thesis: cavity enhanced velocity modulation spectroscopy (CEVMS) and ion beam spectroscopy. Each of these techniques was first implemented in the near-infrared spectral region using a titanium sapphire laser, and was then extended into the mid-infrared, using an optical parametric oscillator (OPO) for CEVMS and difference frequency generation (DFG) for the ion beam. Both of these techniques allow for sub-Doppler resolution to significantly improve the precision beyond what was possible with traditional ion spectroscopy, and because both techniques are based on direct absorption spectroscopy, they require nothing of the ion of interest other than an allowed transition within the tuning range of the laser used, making them applicable to a wide variety of ions. The lasers used with both of these techniques have been referenced with an optical frequency comb for sub-megahertz absolute calibration accuracy of linecenters, which is a significant improvement beyond the 20-200 MHz accuracy that was typical of ion spectroscopy before the work presented in this thesis.

To my wonderful and loving wife, Shannon.

Acknowledgments

First of all, I'd like to thank my advisor, Ben McCall, for all of his support and guidance throughout my time in graduate school. Without him, none of the research presented in this thesis would have been possible. He has always been immensely helpful and supportive, both in big-picture vision for these projects and in helpful discussions and guidance along the way.

I have had the great pleasure of working with several groups of graduate students and post-docs through my time in graduate school, and they have been very instrumental both in the development of new techniques and in the implementation and inevitable troubleshooting along the way. Brian Brumfield helped me to get my feet wet in the lab in working on the QCL ringdown spectrometer. Andrew Mills worked side-by-side with me in the development of the cavity enhanced velocity modulation spectrometer, and Mike Porambo joined in later in the integration of NICE-OHMS into the system. Andrew and Mike, along with Manori Perera and Holger Kreckel, put all of their expertise and lots of hard work into the design and construction of the ion beam spectrometer, and Mike has continued on with the integration of the DFG system we built with the ion beam. Each member of this team has contributed in their own way: Andrew laid much of the groundwork for the ion beam before the rest of us joined the group; Holger and Manori each provided much-needed guidance in various components of the instrument; and Mike has always been, and continues to be, a shining example of hard work and professionalism.

I am also very grateful to Kyle Crabtree and Jamie Hodges for their hard work and dedication in the construction of the OPO experiment, which came together surprisingly quickly. In a matter of months, they took an office space and converted it into a state-of-the-art lab performing spectroscopy with techniques that have never before been used together. Kyle was also incredibly helpful in the many planning discussions we had leading up to the construction of that experiment.

Most of all, I'd like to thank my wife, Shannon, for coming to Illinois with me in support of my pursuit of a Ph.D. She has been immensely supportive over the last several years, and I couldn't have made it through graduate school without her love, help, and support. I would also like to thank all of my family for always being so unconditionally supportive of both Shannon and me. In particular, I'd like to thank my parents,

Bruce and Paula Siller, for introducing math and science from a very early age, and continuing to support my intellectual and personal growth throughout the years. And my mother- and late father-in-law, Wendy and Mark Fredebaugh, have also always been supportive of whatever Shannon and I have decided to do, be it adopting yet another pet or going away to graduate school or having a baby.

Last and smallest (but certainly not least), I'd like to thank my son, Corbin, for making me smile and laugh every single day, and for giving me the opportunity to re-experience the wonders of the world through his eyes.

Table of Contents

List of Figures

Chapter 1

Introduction

Molecular ions are of interest to a variety of fields, ranging from astrochemistry to fundamental physics to the study of reactive intermediates, but studying them in the laboratory often proves difficult for many reasons. First of all, it is difficult to produce them in large quantities. Some typical conditions for a laboratory positive column discharge cell are ∼1 Torr cell pressure and $\sim 10^{-6}$ fractional ionization, meaning that sensitive spectroscopic techniques must be used to detect these ions at effective concentrations of only ∼1 ppb relative to atmospheric pressure. (Of course, these numbers can vary by an order of magnitude or two depending on the exact plasma conditions, but they give a rough idea of the issues that must be considered when developing ion spectroscopic techniques.) Such low fractional ionization also means that neutral precursor molecules present in the plasma discharge cell are around a million times more abundant than the ions of interest, so ion-neutral discrimination is important not only for distinguishing ionic signals from neutral ones, but also to avoid having the potentially much larger neutral signals completely obscure the smaller ionic ones.

One of the most productive techniques for high resolution ion spectroscopy over the past several decades has been velocity modulation spectroscopy (VMS). [92] There are a few reasons that it has been much more productive than some other techniques. For one, the positive column discharge cells typically used have high ion density ($\sim 10^{10}$-10^{12} cm^{-3}) and rich plasma chemistry, so it is possible to create and observe a wide variety of ions with this technique. It also provides excellent ion-neutral discrimination through AC modulation of the discharge voltage and phase-sensitive detection. Because the ions within the cell are accelerated toward the oppositely-charged electrode, their absorption profiles are Doppler-shifted, while any neutral molecules retain the same velocity throughout the discharge cycle.

Until recently, the most advanced VMS setups have used liquid nitrogen cooled discharge cells for lower ion temperatures, and thus lower partition functions for simpler spectra and stronger lines. They have also used unidirectional multi-pass cells for up to ∼8 m of effective path length of the laser through the plasma, while still retaining the same ion-neutral discrimination that is possible with single-pass experiments.

In the completely independent field of neutral spectroscopy, cavity-enhanced techniques are commonly

used to greatly increase the effective path length and optical power through a gas sample. One of the most straightforward cavity-enhanced techniques is continuous-wave cavity ringdown spectroscopy (cw-CRDS). To perform cw-CRDS a laser is coupled into a high-finesse optical cavity. Typically, the cavity length is swept by a piezo-electric transducer (PZT) on which one of the cavity mirrors is mounted. When the cavity length matches a half-integer multiple of the laser wavelength, laser intensity builds up within the cavity, then the laser is chopped and the light intensity within the cavity decays exponentially with a time constant dependent on the intracavity losses, both from the mirror transmission/absorption/scatter, and from the absorption of the intracavity gas. Although cavity ringdown is a very sensitive technique, it does have some limitations. Detection has a very low duty cycle, and the intermittent (and to some degree, random) acquisition make it difficult to integrate with some secondary level of modulation.

An alternative cavity enhanced technique that offers continuous acquisition is cavity-enhanced absorption spectroscopy (CEAS). Because it offers continuous acquisition, it is possible for it to exceed the sensitivity of cw-CRDS. To come close to approaching the shot noise limit, some form of modulation is often needed; most often wavelength modulation is used with CEAS. The other advantage of this technique is that the optical cavity greatly enhances the intracavity optical power, making saturation spectroscopy possible for even weak transitions, such as overtones and combination bands. One of the biggest technical challenges in implementing CEAS is the need to lock the laser frequency and the cavity length to one another, which is discussed thoroughly in Chapter 2.

It was previously thought that CEAS was incompatible with VMS because the symmetry of the cavity would nullify the $1f$ demodulated signal, forcing the $2f$ signal to be used, and this $2f$ signal is sensitive to concentration modulation of excited neutral species. We have shown, however, through careful selection of the phase used for phase-sensitive detection it is possible to not only distinguish ion signals from neutral ones, but also to isolate them from one another in separate detection channels. The initial demonstration of this technique, cavity enhanced velocity modulation spectroscopy (CEVMS) is described in Chapter 3.

The initial CEVMS setup used a Ti:Sapph laser to observe N_2^+ in the near-infrared. One of the most exciting aspects of this technique was the enabling of sub-Doppler spectroscopy through optical saturation of transitions. Although the observed Lamb dips were significantly broader than are typical for neutral molecules ($\sim$50 MHz compared to $\sim$1 MHz), they were still over an order of magnitude narrower than the Doppler-broadened profiles of the same transitions. To take full advantage of the added precision that comes from narrower linewidths, the experimental setup was upgraded with optical frequency comb calibration to provide absolute laser frequency determination to better than 1 MHz. Details of the frequency comb integration and more thorough studies into the width and strength of the Lamb dips are presented in

Appendix A.

Although CEVMS provided for a factor of over 100 greater path length through the plasma discharge cell than a simple single-pass setup provided, the overall signal-to-noise of the observed spectra was no better, and in some cases, the CEVMS spectra had S/N that was significantly worse than single-pass spectra acquired with the same laser and plasma discharge cell. The primary source of noise came from the imperfect lock between the optical cavity and the laser frequency. There was a significant amount of random noise from vibrations in the cavity mirror mounts and in the laser frequency, but the largest source of noise seemed to come from the AC plasma discharge itself. When the plasma was turned on, a significant amount of noise coupled into the cavity locking electronics, and any noise in the cavity lock at the modulation frequency would get converted into cavity transmission laser intensity noise at twice the modulation frequency. This $2f$ noise was particularly problematic, as the lock-ins needed to be set to $2f$ demodulation to observe the desired CEVMS signal. All attempts to add electronic filters and Faraday cages around the plasma cell and associated electronics provided only minimal improvements, so it is thought that the primary source of noise transmission was through the grounding pins of the electronics, since the cavity locking, laser control, and plasma driving electronics all shared a common ground.

The next logical step to mitigate the effects of locking noise on the final spectroscopic signal (both random noise and plasma noise) was to upgrade the experiment to use noise immune cavity enhanced optical heterodyne molecular spectroscopy (NICE-OHMS). This technique combines the techniques of cavity enhancement for increased path length and optical power with heterodyne spectroscopy for very low noise (often approaching the shot noise limit). Before coupling the laser into an optical cavity, two sets of RF sidebands are applied to the laser frequency, one for locking and the other at an exact multiple of the cavity free spectral range for heterodyne detection. This ensures that the three laser frequencies are coupled through the cavity simultaneously, each coupling into its own cavity mode. There are several major advantages of NICE-OHMS compared to CEAS. First, as with all heterodyne spectroscopy, detection is done at high frequencies (100 MHz - 1 GHz), so $1/f$ detection noise tends to be quite small. Second, heterodyne spectroscopy is a zero-background technique, which helps the effective sensitivity even more against some types of additional noise or drifts in the system (such as laser intensity fluctuations). But the biggest advantage of NICE-OHMS over CEVMS is that it is insensitive to laser/cavity locking noise, hence the "noise immunity". There are three laser frequencies coupled through the cavity (the carrier and two RF sidebands), and all three laser frequencies are affected by cavity locking noise exactly the same way, so the net signal is unaffected by any deviations or noise in the locking system. For example, if there was some sudden laser frequency deviation that caused the cavity transmission to drop by 10%, that would create a

noise spike of 10% of the overall transmission intensity in the final spectrum of CEAS, but the NICE-OHMS spectrum would be unaffected, because the two beats between the sidebands and the carrier would both be attenuated by 10%, and would remain balanced for a null signal. A review of the various implementations of NICE-OHMS to date is presented in Appendix D.

Integrating NICE-OHMS into the Ti:Sapph CEVMS setup was straightforward. A second electro-optic modulator (EOM) was added to imprint the heterodyne RF sidebands on the laser in addition to the locking sidebands before the laser was coupled into the cavity. The cavity transmission detector was replaced with a higher bandwidth detector (faster than the heterodyne modulation frequency), and the detector output was first demodulated at the heterodyne frequency before being demodulated at twice the plasma modulation frequency. The initial demonstration of this technique, which we call noise immune cavity enhanced velocity modulation spectroscopy (NICE-OHVMS), is presented in Chapter 4. There are two different implementations presented in that chapter. The initial setup used a resonant EOM at 1.02 GHz and a 1 GHz detector to space the sidebands by 9 times the cavity FSR. Then, in preparation for moving to the mid-infrared (where 1 GHz detectors are not readily available), a different resonant EOM was used to space the sidebands at a single FSR, 113 MHz.

One disadvantage of NICE-OHVMS is that the lineshapes can be very complicated. With heterodyne spectroscopy, there are contributions to the lineshapes from each laser frequency (carrier and two sidebands), and detection is sensitive to both absorption and dispersion. With plasma modulation and demodulation at $2f$, detection is also sensitive to both velocity and concentration modulation of the ions. And with the cavity-enhanced laser power inducing saturation, there are both Doppler-broadened and sub-Doppler components to the observed lineshapes. Chapter 5 describes in detail the various considerations that must be taken into account when attempting to understand the observed lineshapes.

After characterizing and optimizing the system used in the N_2^+ NICE-OHVMS work, the same laser spectrometer was used for direct absorption spectroscopy of the ion beam as described in Chapter 6. Although the ion beam has orders of magnitude lower ion density than the positive column cell used in NICE-OHVMS, it does have some distinct advantages unique to ion beams. For one, simultaneous mass spectroscopy can be performed to optimize discharge conditions to produce optimal amounts of the ion specifically of interest. Doppler-broadened linewidths are narrowed through kinematic compression to provide precision without the obscuring of a much broader lineshape on top of the narrow one. Also, because the Doppler splitting of the two components of the observed transitions is dependent on the mass of the ion, each observed spectral line can be unambiguously assigned to a single ion mass. This can be particularly useful for complex plasmas with many different ion species that must be distinguished from one another. The final advantage of the ion

beam is that it is compatible with supersonic expansion discharge sources, potentially allowing for spectra of very cold ions to be acquired. Work is currently underway to integrate the supersonic expansion discharge source that was previously developed in our lab [18] with the ion beam instrument.

Work is also underway to interface the difference frequency generation (DFG) NICE-OHMS spectrometer described in Appendix C with the ion beam instrument. The new spectrometer was a straightforward extension of the Ti:Sapph NICE-OHMS spectrometer used for the work in Chapters 4 and 6. The Ti:Sapph beam was combined with a fixed-frequency Nd:YAG (at 1064 nm) within a periodically poled lithium niobate (PPLN) crystal. This produced a mid-infrared beam tunable from 2.8 to 4.8 μm. Because the RF sidebands were imprinted on one of the near-IR beams before the DFG process took place, the sidebands get transferred to the mid-IR beam without the need for a specialized mid-IR EOM.

In parallel to the efforts to extend the ion beam into the mid-infrared, work has also been underway to extend NICE-OHVMS to the mid-infrared as well. Because the sub-Doppler resolution of NICE-OHVMS is dependent on the ability of the laser to saturate optical transitions, a higher-power mid-IR source was needed. To this end, an optical parametric oscillator (OPO) was used to provide up to 1 W of mid-IR power, which when combined with the cavity enhancement factor of the optical power, provided more than enough power to saturate mid-IR transitions of molecular ions. The experimental setup is described in Appendix B, along with its initial demonstration with H_3^+. Because we are performing spectroscopy much more accurately than has previously been done with molecular ions in this spectral region, there aren't any 'standard' ion spectra to verify our accuracy. Rather, we used our acquired spectra with the well-studied ion HCO^+ to perform a combination differences analysis that could be directly compared to directly observed rotational transitions. The results of this HCO^+ work are presented in Chapter 7, and show that we are able to obtain sub-MHz accuracy with just Doppler-broadened observations, with the prospect of improving even further when the sub-Doppler cavity-enhanced version of the technique is optimized.

Chapter 2

Laser Locking

This chapter is intended as an introduction to the principles and practical considerations of laser frequency locking. The majority of the chapter is focused on locking lasers to optical cavities, since that is critical for all of the experiments described in this thesis, but there is also some discussion of locking to molecular absorption lines and offset locking to a frequency comb, both of which were also implemented. The specific locking systems used for the spectroscopic systems are also described in this chapter.

In designing any locking system there are a few key elements:

1. a laser with some input to control its frequency
2. something to lock the laser to
3. an error signal
4. feedback electronics to process the error signal before sending it to the laser.

An error signal is just any signal that can be used to provide information about how far the laser is from its desired wavelength and in what direction it is off. The aspect that most commonly discriminates between different types of locking systems is the way in which the error signal is generated.

There are several methods to generate an error signal, each with its own advantages and disadvantages. The types of locking described here are side-of-fringe, dither, Pound-Drever-Hall (PDH) [25], and offset frequency locking.

2.1 Side of Fringe Locking

In side-of-fringe locking, a signal with even symmetry is used, such as transmission through an optical cavity or a molecular absorption, and the laser is locked onto the side of the transmission fringe. This is the method used for locking our Ti:Sapph laser to its stable reference cell. A simulated cavity transmission with its lock point are shown in Figure 2.1.

In the example shown, the laser is locked on the left side of the fringe, with the lock point set to approximately half the height of the maximum transmission. The cavity transmission is continuously monitored; when the transmission rises above the lock point, it indicates that the frequency of the laser is too high, and a correction is sent through the processing electronics to shift the frequency back down to near its original lock point. Likewise, when the cavity transmission dips below its lock point, it indicates that the laser frequency is too low, and must be corrected to shift it back up to its lock point.

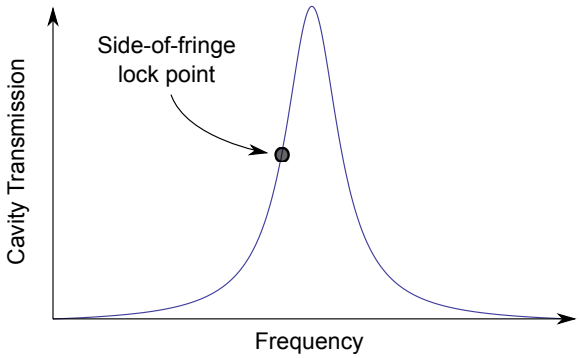

Figure 2.1: An illustration side-of-fringe locking, showing a cavity mode with a side-of-fringe lock point on the low-frequency side of the transmission fringe.

The primary advantage of using this locking method is that it is relatively simple compared to the other methods. The photodiode output *is* the error signal, with no additional processing needed. There are two significant disadvantages, though. For one, any laser intensity noise or detector noise will get converted into frequency noise by the feedback loop. This is because a drop in power laser power manifests in the error signal in the same way as a decrease in the laser frequency, and an increase in laser power appears exactly the same as an increase in laser frequency when the system is locked.

The other disadvantage is that this locking method tends not to be very tight compared to the other methods presented later. In the Ti:Sapph reference cell setup, the reference cell finesse is only $\sim$17, and the free spectral range (FSR) is $\sim$1 GHz, which makes the cavity mode linewidth $\sim$60 MHz (determined by FSR/Finesse).

Using higher finesse cavities with a side-of-fringe proves to be quite difficult. Each method of locking has a natural "capture range", defined as the furthest the laser frequency can deviate while still being corrected back to the center lock point. In Figure 2.1, the laser frequency can deviate as far down as the next cavity mode before the error signal rises above the voltage "lock point". But going in the other direction, the laser frequency can only rise by up to the cavity linewidth before the transmission signal dips down below the lock point and the laser frequency is pushed away from the desired fringe and toward the next one. For the

Ti:Sapph reference cell, this ends up giving a capture range of approximately -1 GHz to +60 MHz, but for higher finesse cavities, the upper limit on the capture range gets smaller as the finesse goes up. For very high finesse cavities, it can be as small as tens of kHz, which means that there cannot be much laser frequency noise at all, and the lock must be very tight.

The final disadvantage of side-of-fringe locking occurs when the light output through the cavity is desired for some other purpose later in the system. Perhaps the cell is being used to clean up the mode structure of the laser before sending it on, or perhaps (as is described in later chapters of this thesis), some analyte is put into the cell, and the cavity transmission is recorded to detect the absorption due to that analyte. In that case, only about half of the possible amount of light is actually available for detection (or perhaps a bit more if the lock point is set higher on the fringe), so the sensitivity is not as good as it would be if the laser was locked to the top of the fringe rather than to the side of it.

2.2 Lock-In Amplifiers

Before moving on to more complex locking schemes, it is necessary to have a basic understanding of how mixers and lock-in amplifiers work. Both dither locking and the Pound-Drever-Hall methods require some form of modulation and demodulation to generate their respective error signals.

A lock-in amplifier consists of a mixer that mixes an input signal with a sine wave at a known frequency, provided to the "reference" input of the lock-in, followed by an integration stage that essentially averages the mixer output for a period of time determined by the time constant of the lock-in.

A mixer works by using some nonlinear circuit elements (often an arrangement of diodes) to essentially multiply two signals (the reference and the signal) by one another. If we assume that the two inputs to the mixer have angular frequencies ω_{ref} and ω_{sig}, then we can use a trigonometric identity to calculate what the output of the mixer must be

$$\sin(\omega_{\text{ref}} \cdot t) \times \sin(\omega_{\text{sig}} \cdot t) = \frac{1}{2}\{\cos[(\omega_{\text{ref}} - \omega_{\text{sig}}) \cdot t] - \cos[(\omega_{\text{ref}} + \omega_{\text{sig}}) \cdot t]\} \tag{2.1}$$

This means that the output of the mixer contains frequency components at both the sum and the difference of the two input frequencies. If the two frequencies are identical, then the mixer will output a DC signal and a signal at twice the input frequency. Within the lock-in amplifier, the stage after the mixer is an integrator. The DC level is unaffected by this integrator (which takes the average signal over some period of time), as it remains at the same level regardless of the integration time. The component at $2f$, however,

gets averaged to zero, as long as the time constant averages over several cycles.

It is worth noting that in the simplified situation presented in Equation 2.2, the phases of the signals are neglected. But when the two input frequencies are identical, their relative phases can have a profound effect on the DC level output in the end. The DC level output by the mixers ends up being proportional to $\cos(\phi_{\text{diff}})$, where ϕ_{diff} is the difference in phases between the two input signals. This means that the maximum output signal comes when the two signals are exactly in phase with one another; when the phases are 180° out of phase with one another, a negative DC level is obtained, equal in amplitude to the signal obtained at 0° phase difference. When the phases are 90° out of phase with one another, no DC level is output. This phase dependence should always be kept in mind when attempting to optimize signals, since an unfortunate choice in phase could completely eliminate any signal.

2.3 Dither Locking

Another method of locking to a cavity or molecular absorption line is a "dither lock." In this method, a small dither is applied to the laser frequency, and the cavity (or absorption cell) transmission signal is demodulated at some multiple of that dither frequency to generate an error signal, as shown in Figure 2.2.

The purpose of the dither lock is to lock the laser on the peak of the cavity transmission. At the peak, the error signal is zero, as shown in Figure 2.2, since the cavity transmission signal has a frequency that is twice the frequency of the applied modulation signal ($2f$); thus, through mixing and integrating, the net lock-in output is null. When the laser frequency drops down to the low-frequency side of the cavity mode, there is some component of the cavity transmission signal at $1f$, and this component is in-phase with the applied dither; thus, a net positive signal is produced by the lock-in. Likewise, when the laser frequency rises up above the peak of the cavity transmission, a net $1f$ signal is produced, but this time, it is 180° out of phase with the applied modulation, which gives a net negative signal out of the lock-in amplifier.

The overall error signal, produced as the laser is scanned across a cavity resonance, is shown in Figure 2.2. Note the odd symmetry with a zero-crossing at the peak of the cavity transmission. This zero crossing is typically used as the lock point, as it maximizes transmission through the cavity and provides a more robust lock than offset locking to some other point on the error signal.

The biggest advantage of dither locking compared to side-of-fringe locking is that it allows for the laser frequency to be locked at exactly the peak of the reference fringe, be it a cavity transmission or a molecular absorption. When using an optical cavity, this allows for the maximum amount of light to be coupled through the cavity, and also improves the capture range of the lock, extending it in principle all the way

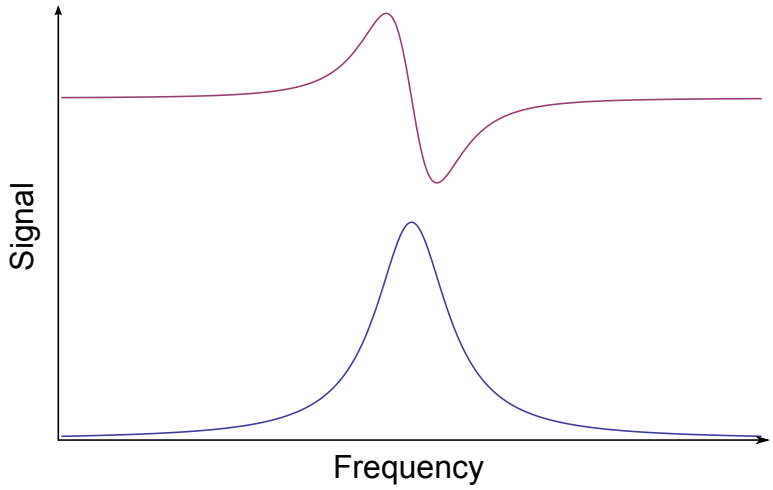

Figure 2.2: A dither locking error signal, along with a cavity mode. For sufficiently small dither, the error signal appears as the derivative of the cavity transmission.

to the next cavity modes on either side of the desired fringe; this makes the lock significantly more robust than locking to the side of a fringe, especially for higher-finesse cavities and narrower molecular absorption lines. In practice, the practical capture range of the lock is typically limited by a convolution of the cavity linewidth, the laser linewidth, and the dither amplitude, though if the laser is outside of this range, it will typically eventually drift to a point where it is within this range of the lock point.

When locking to a known molecular absorption line, this provides the added benefit of knowing the exact frequency of the laser once it is locked onto the center of the line, to within the precision that the lock point is set with. This is the method we use to lock the Nd:YAG laser from the difference frequency generation (DFG) setup onto an iodine hyperfine transition, which is described in Appendix C.

When implementing a dither lock, it is often advantageous to use some odd harmonic of the dither frequency, rather than the dither frequency itself, as the error signal in a locking system. Any odd harmonic will work in principle, since they all have an odd symmetry with a zero-crossing exactly at the line center. Using the higher-order harmonics is often advantageous for two reasons: 1) the higher harmonics tend to have a slightly steeper slope for the lock point, which makes the lock more sensitive to small deviations from the central lock point and can improve the overall quality of the lock; and 2) observing the higher order harmonics can be very useful for removing any slowly-sloping baseline that the error signal sits on top of. For example, when locking to iodine hyperfine transitions, the Doppler profile appears quite strongly in the $1f$ signal (as shown in Figure 2.3), but is very nearly completely flat in the $3f$ signal (as shown in Figure 2.4. This flatter baseline makes it much easier to properly set the lock point in the center of the Lamb dip, and also makes the system much less sensitive to changes in the Doppler profile, for instance if the temperature

of the cell changes slightly, which changes the vapor pressure of iodine within the cell, making the Doppler profile stronger or weaker.

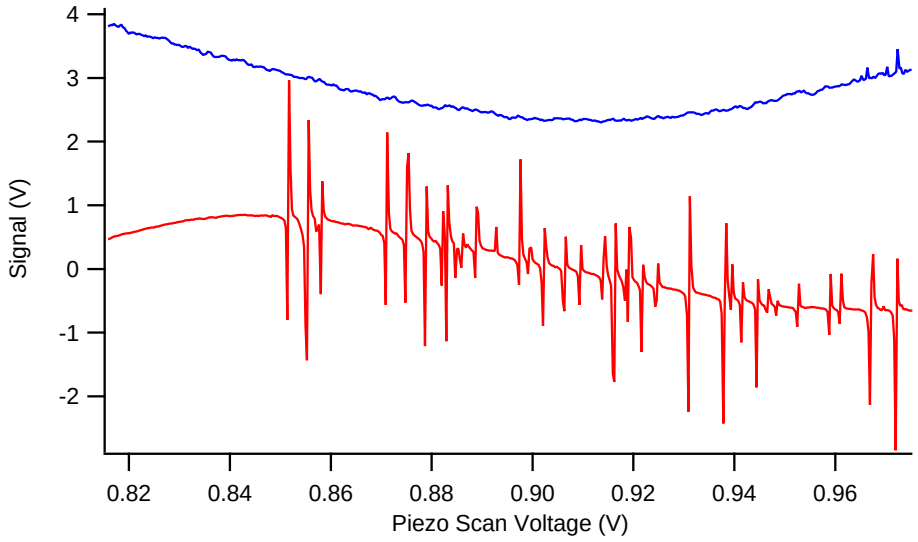

Figure 2.3: Signals from DC detection (blue) and $1f$ demodulation of iodine observed when dithering the laser wavelength by several MHz. Because the dither is small compared to the Doppler profile width but large compared to the Lamb dip widths, the Lamb dip signals are much stronger in the $1f$ dither detection than the Doppler profile, although a portion of the broad derivative-like lineshape of the Doppler profile is still apparent in $1f$ detection.

There are some limitations of dither locking, though. For one, the applied dither may interfere with any spectroscopy done with the laser. If the dither frequency is on a comparable time scale to the data acquisition the dither may appear as noise or it may be aliased to appear as fringing in the final signal. If the data acquisition is averaged over several cycles of the dither, it may effectively broaden the linewidths of any detected signals. Both of these manifestations of the dither can be minimized to some extent by making the dither amplitude as small as possible while still maintaining the desired quality of lock.

The other limitation of the dither locking technique is that it may limit the locking bandwidth available to the laser. For example, the maximum modulation bandwidth of our Nd:YAG laser through its piezo control is 10 kHz. If we apply the dither at this frequency, we must set the lock-in time constant to average over several dither cycles to get a reliable error signal without too much noise. This limits the frequency corrections that can be applied to the laser to closer to $\sim$1 kHz, rather than the full 10 kHz bandwidth that we'd be able to utilize if we were able to take advantage of the full bandwidth of the piezo rather than having to reserve some portion of it for dithering. Also, if corrections are applied too quickly relative to the dither, one risks the possibility of the lock actively canceling out some portion of the dither as it tries to correct it as it happens.

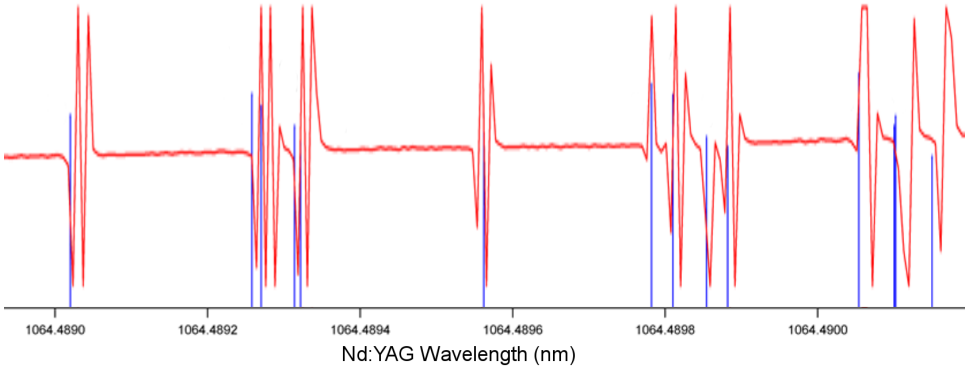

Figure 2.4: The wavemeter-calibrated signal from $3f$ demodulation of iodine observed when dithering the laser wavelength by several MHz. Compared to the $1f$ signal in Figure 2.3, the baseline is nearly completely flat and the Lamb dips appear with third-derivative-like lineshapes, compared to first-derivative-like ones in $1f$ detection. Overlaid in blue are the previously assigned hyperfine components of this transition, which are known to within ∼10 kHz (much better than the wavemeter calibration that was used to generate the current $3f$ data).

2.4 Pound-Drever-Hall Locking

The Pound-Drever-Hall (PDH) method [11, 25] is the one most commonly used for locking a laser to a high-finesse cavity. It relies on the principles of heterodyne detection to observe the dispersion of an optical cavity for generating an error signal. [11] Heterodyne detection is discussed thoroughly in Section 5.3, so it will not be discussed here.

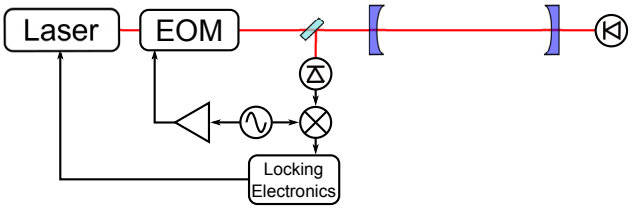

Figure 2.5: A generic experimental layout for locking to a cavity with the Pound-Drever-Hall method.

A generic PDH setup is shown in Figure 2.5. The electro-optic modulator (EOM) applies a set of heterodyne sidebands to the laser frequency. Typically these sidebands are spaced at anywhere between a few MHz to tens of MHz, with a fairly small modulation index ($\beta \sim 0.1$). The back-reflection off of the cavity is captured by a high-speed photodiode. In this setup, where the back-reflection rather than cavity transmission is observed, the cavity acts as an absorber when the laser is on resonance with a cavity mode. According to the Kramers-Kronig relations, any absorption of light must be accompanied by a corresponding dispersion. [55] Since heterodyne spectroscopy is sensitive to both the absorption and dispersion of light, we

can detect both absorption and dispersion on the back-reflection detector. As is discussed in Section 5.3, we can choose whether we are sensitive to absorption or dispersion signals by selecting the appropriate phase of demodulation for the detector signal.

Heterodyne spectroscopy is only sensitive to absorption of the sidebands, not the carrier, so no net signal will appear at the carrier frequency in the absorption detection phase. But it is sensitive to dispersion for both the carrier and the sidebands, and the overall dispersion signal has odd symmetry with a zero-crossing at the peak of the cavity transmission. The cavity transmission, back-reflection, and heterodyne signals for both the absorption and dispersion phases of the back-reflection are all shown in Figure 2.6.

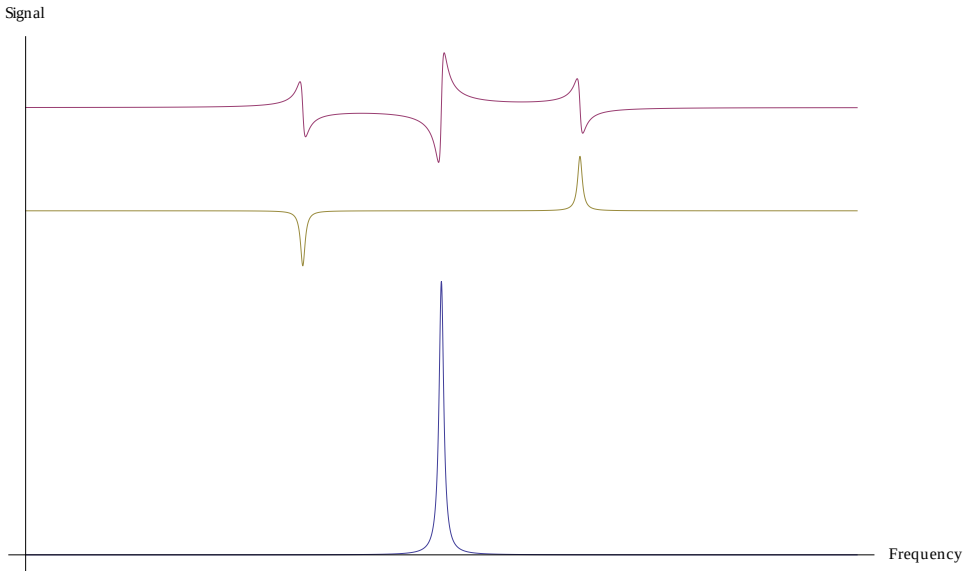

Figure 2.6: The cavity transmission (blue) and error signals for both the absorption (yellow) and dispersion (red) phases of the back reflection in a Pound-Drever-Hall setup. The heterodyne dispersion signal of the back reflection is used as the error signal for locking, as it has the appropriate symmetry and a zero-crossing at the peak of the cavity transmission.

Compared to dither locking, PDH locking has several advantages. For one, it doesn't require the extra dither to be applied, so there isn't any extraneous noise coupled into the system from the dithering. Since the PDH modulation frequency is so much higher than any dither frequency that would be applied, it doesn't limit the bandwidth available to the laser for locking. The effective capture range of a PDH lock extends all the way out to the sidebands on either side of the carrier, which are spaced at plus and minus the modulation frequency, because the points at plus and minus the sideband spacing are those at which the sign of the error signal changes from correcting the laser frequency toward the central lock point to pushing the laser frequency away from it.

2.5 Offset Frequency Locking

All of the locking schemes described above are used to lock a laser to the center of an absorption or cavity resonance. Even the side-of-fringe locking scheme gets the laser to within less than half the width of a resonance of the center of the resonance. There are times, however when it is desirable to stabilize a laser to some precision reference, but have the central frequency of the laser offset by some known frequency from the center of the reference resonance.

One method for doing this, which is fairly common in the atomic, molecular, and optical (AMO) physics community, is a straightforward extension to either the dither or the PDH methods described above. A set of sidebands is added to the laser frequency, typically using an EOM, and one of the sidebands is locked to the fixed reference, often a saturated atomic absorption of well-known frequency. The sideband can either be locked by producing a second set of sidebands, and performing a PDH-type lock, or the EOM RF modulation frequency can be dithered slightly for a dither-type lock. Then, to perform spectroscopy using the carrier frequency, the EOM modulation frequency is scanned over the range of interest. Using high-bandwidth fiber-coupled EOMs, the offset frequency can be scanned by up to several GHz, or as low as just a few MHz. The locking scheme could also be reversed, where the carrier is locked to a stable reference, and one of the sidebands is used to perform spectroscopy. Another option is that a laser could be locked to a stable reference, then frequency-shifted using a acousto-optic modulator (AOM), and use the frequency-shifted beam to perform spectroscopy, although AOMs tend to have much more limited bandwidths compared to EOMs, so this method is not as common. In either case, the offset frequency can be monitored with a simple RF frequency counter. If the counter has an internal reference that is synchronized with an absolute reference frequency, for example an atomic clock or a GPS-synchronized reference, then the measured RF offset frequency can typically be determined as precisely as the input reference frequency (on the order of 10^{-15} relative precision for a GPS reference).

The other type of offset frequency locking is the one that we use to lock our cw lasers to our optical frequency comb. It relies on detecting the beat signal between the cw laser frequency and one of the comb teeth, and using some feedback control to keep this frequency at a fixed value. We use two different methods for generating an appropriate error signal, each with its own advantages and disadvantages.

The first method utilizes the error signal generation electronics that came with the comb, and are mounted in the comb rack. There is a frequency counter with two inputs: one that increments a counter with each cycle of the input signal, and the other that decrements the same counter with each cycle of the input. The "up" counter used is the frequency-doubled GPS reference frequency, which causes the counter to count up at exactly 20 MHz. The "down" counter comes from the detector that 'sees' the beat signal of the cw

laser with a comb tooth, after some filtering and amplification electronics that clean up the signal and raise it to the appropriate amplitude to correctly trigger the actual beat signal, but not on the noise at nearby frequencies.

When the up and down counters are at exactly the same frequency, the net error signal output (the output of the counter box) is a DC level at whatever the counter value was the last time the frequencies differed at all. But if the two frequencies are at all different, the error signal with increase or decrease, depending on which input has the higher frequency. But, because the counter has a finite number of bits, if the difference in the two counts gets large enough, then the counter must reset.

Given that it is a 14 bit counter, if the frequencies are different by on the order of 1 MHz, the counter resets in a matter of milliseconds. For a free-running laser, this typically means that the counter is continuously slewing and resetting, giving an apparent sawtooth waveform out of the counter. The direction of the sawtooth tells which input is at a higher frequency: a slew up and jump down indicates the "up" input is higher in frequency, while a slew down and jump up indicates that the "down" input is higher in frequency.

To engage the lock, the two frequencies are tuned as close as possible to one another, as indicated by the slope of the sawtooth. This is done by tuning the frequency of the cw laser such that its offset from a comb tooth is as close as possible to 20 MHz. Then, if the lock is successfully engaged, the counter output should read near zero with some noise. If the counter output is still reaching the rails and resets at any point, this makes the feedback electronics prone to pushing the laser away from the lock point rather than toward it, so it is not a very robust lock. When the lock does work, it is an extremely tight lock. The carrier-envelope offset frequency (f_{ceo}) is locked with this method down to $\sim$1 Hz, and we have managed to stabilize the OPO pump beam to the comb to within $\sim$5 Hz, but the lock is very difficult to obtain and optimize without completely losing it.

With this locking scheme, the "capture range" is a bit difficult to define, since it is dependent not only on the frequency difference between the current frequency and the lock point frequency, but also on the time this difference is maintained. For example, since we have a 14 bit counter, the "up" and the "down" inputs can differ by up to $2^{13} = 8192$ "counts" at any given time without losing the lock. This means that if they differ by 1 MHz, corrections must be made within 8.1 ms to avoid losing the lock, while if they differ by 100 kHz, the system has 81 ms to correct itself before losing lock. This condition is fairly easy to meet when locking f_{ceo}, since the free-running offset frequency deviation is quite small, and the piezo that is used to lock it is quite fast. It is also possible for us to lock the ytterbium-doped fiber laser (YDFL) that acts as the seed to the OPO, since it also has good frequency stability, a very narrow free-running linewidth, and reasonably fast control through its piezo input. But we have had great difficulty in attempting to lock our

Ti:Sapph laser to the comb with this method, since it has worse frequency stability than the fiber laser, and to get its free running linewidth narrow enough to generate a reasonable error signal, it must first be locked to its reference cell rather than directly to the comb, and the reference cell piezo is very slow, so doesn't allow for very fast frequency corrections to be made.

The second method we use to lock cw lasers to the comb relies on a frequency-to-voltage converter. Compared to the counter-based system, it is substantially simpler to obtain and maintain lock, but the lock is not nearly as tight, locking to within ∼5 kHz rather than the ∼5 Hz that is possible with the counter-based lock. It is worth noting that the uncertainty in the comb repetition rate limits the determination of the exact frequency of a given comb mode to within ∼10 kHz, so the looser lock of the cw laser onto a comb mode doesn't significantly affect the precision of the laser frequency measurement. One possible detrimental effect of the looser lock comes if we start to become concerned with laser linewidth; a very tight lock to a stable reference can narrow the effective laser linewidth substantially, and thus allow for the observation of narrower spectral features (if laser linewidth is the limiting factor) or for more light to be coupled into an optical cavity (if the cavity linewidth is narrower than the laser linewidth). Currently, neither of these effects is substantial in our experimental setups, so the looser frequency-to-voltage lock is strongly preferred.

The frequency-to-voltage converter works exactly how it sounds: it takes an input signal at some frequency, and using a combination of digital logic and analog signal processing, it gives an output voltage at a level that scales with the frequency of the input signal. Integrated circuits that perform this functionality within a single chip are readily available at frequencies of up to a few MHz, but for our application, we would prefer to be able to offset lock at a frequency of around 20 MHz, so we use a custom circuit to perform the frequency-to-voltage conversion for us.

Using the F-to-V converter for offset locking is straightforward: a DC offset is added to the output of the circuit (generally within the lock box), and the lock is engaged, with the feedback being sent to control the cw laser frequency. The DC offset determines exactly what frequency is used for the offset; for example, if no DC offset is applied to our circuit, the circuit zeros out at around 20 MHz input frequency, with a transfer function of around 1 V/MHz. So if an offset frequency of 25 MHz is desired, a DC offset of 5 V is added to the error signal input.

One consideration that must be kept in mind whenever using any sort of digital logic circuitry, either with the counter-based system or the F-V converter one, is that the RF input signals must have an amplitude that is large enough to trigger the logic gates with each cycle, while keeping the noise levels at other frequencies low enough to not cause false triggers. Noise can be a particular issue at very low as well as very high frequencies. Low frequency noise can cause the overall level of the desired signal to drift too low or too

high to reach the proper digital trigger thresholds, giving a reported frequency that is lower than the actual frequency. High frequency noise can cause each zero-crossing of the desired signal to effectively trigger multiple zero-crossings, giving a reported frequency reading that is higher than the actual frequency. To minimize both of these noise-induced effects, a bandpass filter is typically used to only allow through a fairly narrow range of frequencies: a Mini-Circuits BBP-21.4+, which passes frequencies in the range 18-25 MHz. We also amplify the signal just enough to trigger the counters while still keeping the noise at nearby frequencies below the trigger threshold; given that the typical signal-to-noise for the beat signal is ∼30 dB, this gives a fairly large dynamic range to work in.

2.6 Feedback Electronics

Every feedback system described here, regardless of the method of error signal generation, requires some amount of signal processing to convert the generated error signal into a feedback signal that can be applied to some frequency transducer in the system. This is more of an electrical engineering problem than a scientific one, but building and optimizing the feedback electronics is often the most challenging and time-consuming aspect of building a locking system. Described in this section are some general design principles that should be taken into account that can make this process much easier, as well as the description of the general lock box design used for most of the locking systems in our lab.

There are some system parameters that, if known ahead of time, make the designing of the locking electronics significantly easier: the transfer function and the frequency response of each of the frequency transducers of the system.

The transfer function defines how much the laser frequency shifts given some applied voltage or current to the input of the transducer. It is typically given in terms of MHz/Volt, but could equivalently be given in terms of cm^{-1}/mA or any similar units. When the actuator is a piezo-electric transducer (PZT), the transfer function is defined in terms of piezo sweep per voltage, and using that sweep along with the length of the cavity, a change in the FSR can be computed and used as the voltage-to-frequency transfer function for the transducer.

Knowing the transfer function enables you to at least have some rough estimate of the amplitude of corrections that need to be applied to the system, and what the total scanning range needs to be to scan the desired frequency range.

For example, if the transfer function is very steep for some transducer, let's say 1 GHz/V, and we want to make fast corrections with amplitudes ranging from 1 kHz to 1 MHz, this means that the voltage applied

directly to the transducer needs to be in the range of 1 μV to 1 mV. In such a case, one would not want to use a general-purpose locking circuit with a range of 10 V, since only 0.1% of the total range would be used, and the electronic noise in the locking circuit would need to be kept down to a level of around 1/1000 of that.

At the other extreme, if DC corrections are desired to a given actuator to enable scanning, the output range of the locking circuit needs to cover at least enough voltage range to cover the desired frequency scanning range. This means that if one wants to scan over the width of a Doppler-broadened line, which can be anywhere from a few hundred MHz to a GHz or more, one needs to plan ahead to make sure the lockbox can output the voltages across the entire desired scanning range.

The other aspect of the frequency transducers that needs to be taken into account, especially when multiple transducers are used in a single locking setup, is the frequency response of each one. This information determines what frequency components of the error signal should be sent to which transducers, as well as which filters should be put on which signals for optimal locking performance without oscillation. When designing the locking electronics, the bandwidth of each transducer can typically be estimated from the associated specification sheet. For PZTs, the limiting bandwidth is the lower of the specified bandwidth and that determined by a combination of the piezo driver output impedance combined with the piezo capacitance, which is given by $1/2\pi$RC. For AOMs, there is a similar restriction, where the minimum of the time limitation determined by the speed of sound of the acoustic waves propagating through the crystal, and the driving electronics determines the effective frequency response of the AOM.

Once the locking system is completely built and operational, the bandwidth of each frequency transducer in its completed feedback circuit can be determined by turning up the gain on the associated loop to the point where the lock starts to 'ring', which means it oscillates at a very regular frequency as the lock continuously overshoots the lock-point and gets caught in a positive feedback cycle where it keeps overshooting the desired lock point. The frequency of this ringing is typically at the upper bandwidth limit of the control loop that is ringing. Note that this is the bandwidth of the entire loop, not just of the physical transducer, so it may be limited by the electronics or detector response or whatever the lowest bandwidth element in the loop is. Ringing can also be induced when two control loops have too much bandwidth overlap and compete with one another, and it is important to not get confused by these two effects when troubleshooting or optimizing the system.

Once the bandwidth response and transfer functions for each frequency transducer have been determined, the actual locking electronics can be built. When designing the electronics with multiple loops, it is important to make sure they don't have too much frequency overlap so they don't try to compete with one another. It

is especially important that only a single control loop can make DC corrections to the system; the actuator with the broadest wavelength tuning range is generally selected for this purpose.

The design of the electronics themselves does not need to be very complex at all. Most of the lock loops assembled in our lab have used the same locking circuit, with some slight modifications from one instance to another. The original design of the circuit was done by Jun Ye at JILA for use with a tunable diode laser, so its two control loops were designed to control a PZT with a bandwidth of ∼70 Hz (the "PZT" loop) and the current of the diode laser with an adjustable bandwidth that can go up to ∼1 MHz (the "LD" loop). The actual printed circuit board was designed by Mingwu Lu from Ben Lev's lab in the physics department here at the University of Illinois.

Because this circuit is designed around a series of individual operational-amplifier-based sub-circuits, the overall operation can be determined by first understanding each of the sub-circuit's response functions, then multiplying all of the response functions together to get the final response of the full circuit.

2.7 Titanium:Sapphire System

This is the laser system that initial tests were done on for all major techniques described in this thesis: CEVMS (Chapter 3), NICE-OHVMS (Chapter 4), and ion beam spectroscopy (Chapter 6). Two different locking configurations were used.

In the first incarnation of this system, the included software for controlling the Ti:Sapph internal frequency actuators was used to lock the laser directly to the external cavity. This software was designed to perform a side-of-fringe lock of the Ti:Sapph laser onto a temperature- and pressure-controlled reference cell, which has a finesse of ∼17 and a FSR of ∼1 GHz.

The general procedure for locking to the reference cell was to sweep the reference cell length to see several cavity resonances, set the lock point to approximately half the height of the tallest fringe, and then stop sweeping the cavity and engage the lock. The laser frequency would slew up or down until it "caught" onto a cavity resonance, and it would then remain locked as the cavity was slewed to perform spectroscopy. This procedure had to be modified to implement PDH locking onto our external spectroscopy cavity.

The cavity used for spectroscopy in this initial setup had a finesse of ∼100, limited by an intracavity iris that was used to both decrease the finesse (to make locking easier) and to spatially filter out transverse modes and make sure the TEM_{00} was the only mode with significant transmission through the cavity. Locking sidebands spaced at ∼20 MHz were applied to the laser using an EOM, and the resulting error signal was sent to the laser control electronics. Because the laser electronics had no control over the external

cavity length, it had to be swept manually with a function generator. If the lock point was set to 0 V immediately (corresponding to the zero-crossing of the center of the error signal), the laser was as likely to lock onto one of the sidebands as it was to lock onto the carrier. Rather, the lock point was set high enough to be above the peaks of the sideband contributions to the error signal while still being low enough to catch the top of the carrier error signal. The lock was then engaged, and after the laser was firmly locked onto the cavity, the lock point was slewed down to the zero-crossing to maximize cavity transmission. Scanning was accomplished by slewing the length of the external cavity and having the laser frequency follow the cavity length to remain locked.

The bandwidth of this locking scheme was ∼12 kHz, limited by the fastest frequency actuator within the Ti:Sapph laser cavity: the tweeter mirror that was mounted on a small piezo-electric transducer. This setup worked well for our initial demonstration of CEVMS, but it did have a couple of key limitations. First, the laser was locked directly to a relatively unstable cavity rather than to the stabilized reference cell, so its frequency stability wasn't very good, as it was prone to shift with changing temperature and pressure in the lab, as well as with mechanical vibrations in the cavity mirrors and mounts. Second, the 12 kHz bandwidth of the lock limited the possible finesse to only ∼100. When the intracavity iris was opened to increase the finesse (up to the intracavity Brewster window limited finesse of ∼300), the lock would become so noisy that it was essentially unusable, with maximum deviations so large that the cavity transmission dipped as low as half of its peak value.

To improve upon the system, a second generation locking setup was implemented using a double-pass AOM. [24] In this system, the Ti:Sapph laser was locked onto its reference cell as intended by the manufacturer, and two external actuators were used to lock the cavity and laser to one another. The error signal is split into slow (<70 Hz) and fast (>70 Hz) control loops by electronics. This allows the stability of the reference cell to be transferred to both the laser and the external cavity length on slow time scales, while allowing for the enhanced locking bandwidth that comes from the AOM setup. The vast majority of laser frequency and mechanical noise in the laser and the external cavity happens at low frequencies, due to drift over time as well as vibrations picked up through the table as well as picked up acoustically through the air.

The fast corrections are added to a DC offset before being sent to the input of a voltage controlled oscillator (VCO). This DC offset ensures that the average frequency of the signal being sent to the AOM is one at which the diffraction efficiency is near a maximum, 85 MHz for this particular AOM. The output of the VCO is then amplified with an RF amplifier to ∼1 W total power before being sent to the AOM. By monitoring the corrections being sent to the VCO input while locked, it was found that the maximum magnitude of correction being sent to the laser through the fast loop was <1 MHz. And because the slowest

laser frequency corrections (via AOM) are much faster than the timescale of detection for the experiment (lock-in time constants are typically >100 ms), these fast corrections just broaden the effective linewidth of the laser. Because the laser linewidth is not the limiting factor for any of the spectroscopic techniques we employ, the broader laser linewidth has no significant effect on the final spectroscopic signals.

2.8 DFG System

The difference frequency generation (DFG) system is a straightforward extension of the Ti:Sapph system described in the previous section. The mid-infrared DFG is created by combining the Ti:Sapph beam and a beam from a Nd:YAG (at 1064 nm) in a periodically poled lithium niobate (PPLN) crystal. Because the Ti:Sapph is used as one of the pumps of the DFG system, we used the same double-pass AOM setup for fast frequency corrections, and the same cavity piezo for slow corrections. The only change to the Ti:Sapph beam path (other than the addition of the PPLN) was that the EOMs were moved from the tunable Ti:Sapph to the fixed-frequency YAG. This was done to mitigate the effects of frequency-dependent RAM and etalons that can interfere with the locking and heterodyne sidebands. The one disadvantage to this design choice was that the modulation efficiency of EOMs tends to decrease with increasing laser wavelength, but this in turn could be fixed to some degree by increasing the RF power applied to the EOMs, up to the maximum level they could take without causing damage.

The cavity mirrors and detectors (both for cavity transmission and back-reflection) also needed to be switched out for mid-infrared components. In the initial DFG setup, we used a relatively slow 1 MHz bandwidth InSb detector for detecting the cavity back-reflection and generating a PDH error signal. This worked reasonably well, and we found that we could push the locking sideband modulation frequency as high as 2 MHz while still retaining a strong error signal, but this is still a much lower frequency than the ∼20 MHz that was used with the Ti:Sapph system. A low modulation frequency makes for a narrow capture range when first acquiring a lock, which doesn't interfere with the quality of the final lock, but does make it somewhat more difficult to initially acquire the lock, as the cavity is prone to slewing to one extreme or another, or locking on to some transverse mode, depending on where in frequency space the laser and TEM_{00} cavity mode happen to be when the lock is engaged. To improve this, we later added a 20 MHz bandwidth InSb. The actual bandwidth of the detector appears to be somewhat lower than the specified value of 20 MHz, but it does enable locking with sidebands spaced at ∼10 MHz, which makes locking significantly easier, as frequency jitter in the system tends to be less than 10 MHz, so it is simple to position the laser to stay within the capture range of the desired cavity mode long enough to engage the locking circuit.

2.9 OPO System

The optical parametric oscillator (OPO) system works similar to the DFG system. Both use near-infrared lasers with PPLN crystals to create mid-infrared beams. The main difference is that the DFG requires two near-IR pump beams, while the OPO only requires one, with the second one generated within a resonant cavity. The OPO works as follows: a 1064 nm fiber laser (the seed) is sent through a fiber-coupled EOM to add RF sidebands for both cavity locking and heterodyne spectroscopy. The modulated seed is then sent through a fiber amplifier to boost the total power to 10 W, creating the pump for the OPO. The pump is then sent to the OPO head, where it is coupled through a fan-out PPLN crystal. Around the PPLN is a ring cavity that is resonant with the signal beam (tunable from 1.5 to 1.6 μm); the frequency of the signal beam is selected by a combination of the poling period of the PPLN and the angle of an intracavity etalon.

The major advantage over the OPO system compared to the DFG one is the much higher power output. The DFG produces up to 500 μW of tunable mid-IR power, while the OPO can output up to 1 W. This allows for much faster, cheaper, and more readily available detectors to be used for locking and for heterodyne spectroscopy. The detectors used for the OPO system have nearly twice the bandwidth and less than half the cost of the high speed InSb detectors needed for the DFG, while having the added advantage of not needing to be cooled with liquid nitrogen.

This system uses the exact same locking electronics as the Ti:Sapph and DFG systems. The slow loop actuator is still one of the cavity mirrors, but the fast loop controls a mirror within the signal cavity inside the OPO head. This mirror has a tuning range of a few MHz, and a modulation bandwidth of $\sim$10 kHz. Although this is not as fast as the AOM used in the other systems, the frequency stability of the OPO is significantly better than that of the Ti:Sapph, so not as many high frequency corrections are needed to obtain a good cavity lock. We have found that this system can lock onto a cavity with finesse $\sim$700, limited by the reflectivity of the cavity mirrors, so it could likely lock onto an even higher finesse cavity if we had the appropriate mirrors.

One innovation that we implemented in the OPO system was an "auto-relocker" system, which would automatically pause a scan, unlock the cavity, and re-obtain lock before resuming the scan. Two electronic circuits were required for this system: a comparator circuit, to indicate to the computer whether cavity transmission was "high" (locked) or "low" (unlocked or locked onto a smaller transverse mode); and digital control over the integrator switch of the lockbox. This integrator switch turns the DC gain of the lockbox to 0 when disengaged, effectively disabling the lock.

The auto-relocker works as follows: When the piezo voltage approaches one of its limits or the comparator senses that lock was lost, the scan is paused and the integrator is disabled. The cavity then slews back to

its initial length (the length it was at before being locked and scanned), and the integrator is re-enabled. If lock is obtained, then the scan continues. Otherwise, the integrator is disabled once again, a small DC offset is applied to the piezo driver (in hopes of shifting to cavity to within the capture range of the laser), and the integrator is re-enabled. This process continues until the lock is re-acquired and the scan can continue. If the piezo driver scans by more than a cavity FSR ($\sim$10 V for this system) and lock is never regained, the control program gives up and the user must manually adjust the locking parameters to relock the system. The most common cause of this is a drift in the DC offset of the error signal (often due to RAM) that needs to be manually corrected by a compensating DC offset.

This auto-relocker system drastically improved the time it takes to acquire scans, especially those over broad frequency ranges, as are typical for initially discovering lines and recording Doppler profiles. For some of the faster scans we've done (short time constant and relatively large frequency steps), the auto-relocker has sped up the scan rate by a factor of 2-3. It has been so useful that we have also implemented a copy of this system on the DFG setup.

Chapter 3

Cavity Enhanced Velocity Modulation Spectroscopy

3.1 Abstract

The spectroscopic study of molecular ions is of great importance to a variety of fields, but is challenging as ions are typically produced in plasmas containing many orders of magnitude more neutral molecules than ions. The successful technique of velocity modulation permits discrimination between ion and neutral absorption signals and has allowed the study of scores of molecular ions in the past quarter century. However, this technique has long been considered to be inappropriate for use with cavity-enhanced techniques, owing to the directional nature of the velocity modulation. Here we report what we believe to be the first demonstration of cavity-enhanced velocity modulation spectroscopy, utilizing a $2f$ phase-sensitive demodulation scheme. This approach offers the promise of combining very high-sensitivity spectroscopic techniques with ion-neutral discrimination, which could extend the applicability of velocity modulation to intrinsically weak transitions and to ions that cannot be produced in high abundance. The use of a cavity also permits Lamb dip spectroscopy, which offers higher resolution and precision in frequency measurements and may be useful in measuring collisional rate coefcients.

3.2 Introduction

Molecular ions play important roles in many fields, ranging from chemistry to propulsion to astrophysics, but they pose significant challenges to the laboratory spectroscopist. Two of the greatest challenges are preparing ions in sufficient quantities in the gas phase and detecting absorption lines of ions in the presence of interfering transitions of neutral molecules, which are typically several orders of magnitude more abundant. The production of large quantities of ions has been most successfully addressed by exploiting the positive

This chapter was first published as: B. M. Siller, A. A. Mills and B. J. McCall,"Cavity-Enhanced Velocity Modulation Spectroscopy", *Optics Letters*, **35**, 1266-1268 (2010).[89]

column of a glow discharge, as first demonstrated by Claude Woods group in the microwave [23] and later by Oka in the IR [72]. But it was not until the development of the velocity modulation technique by Saykallys group [41] that absorptions owing to neutral molecules could be avoided, so that these discharges could be fully exploited for ion spectroscopy. In the past quarter century, nearly 50 molecular ions have been studied by using velocity modulation, as reviewed in [93].

Much of the recent development work on velocity modulation has focused on improving the signal-to-noise ratio (S/N), to permit the study of trace ions or intrinsically weak transitions. The combination of optical heterodyne modulation with velocity modulation [38, 71] has pushed the noise level close to the shot noise limit with moderately intense lasers. Further improvement in the S/N therefore will require an extension of the optical path length through the plasma. The typical state of the art in this respect is a modified White cell [38, 71] that affords a total path length of ∼8 m. This path length could, in principle, be increased dramatically by enclosing the positive column in a high-finesse optical cavity, as has been employed for the NICE-OHMS technique [114]. However, traditional velocity modulation spectroscopy relies on the difference in the ion drift velocity between the two half-cycles of an AC discharge, so the $1f$ signal vanishes in a cavity (or any bidirectional multipass cell). In this work, we demonstrate that ion-neutral discrimination can be preserved in cavity-enhanced velocity modulation spectroscopy by using a $2f$ demodulation scheme.

3.3 Experimental

Our experimental setup is illustrated in Fig. 3.1. Molecular ions (N_2^+) are produced in an uncooled positive column discharge cell in a continuous flow of nitrogen at a pressure of ∼3.4 Torr. The cell used is identical to that described in [102], with the exception that the cavity ringdown mirrors in that reference have been replaced by BK7 Brewster windows to allow the insertion of an intracavity iris. The plasma is produced by an AC sine wave (3.8 kV_{pp}, 40 kHz) delivered to two water-cooled electrodes spaced by ∼40 cm, and generated by a step-up transformer, the primary loop of which is driven by an audio amplifier (AE Techron 5050) in series with a 5Ω resistive load for plasma stabilization. The cell is placed inside an optical cavity that consists of two fused silica dielectric mirrors with 1 m radii of curvature and reflectivity 99.7%, separated by ∼1.3 m. One of the mirrors is mounted to a cylindrical piezoelectric transducer (Piezomechanik), which controls the length of the cavity. The finesse of the cavity is reduced to ∼100 by using the intracavity iris, to facilitate locking.

A ring Ti:sapphire laser (Sirah Matisse-TS) is locked to the cavity by using the Pound-Drever-Hall (PDH) method [25]. The back-reflection from the cavity is sampled by using an ordinary beam splitter,

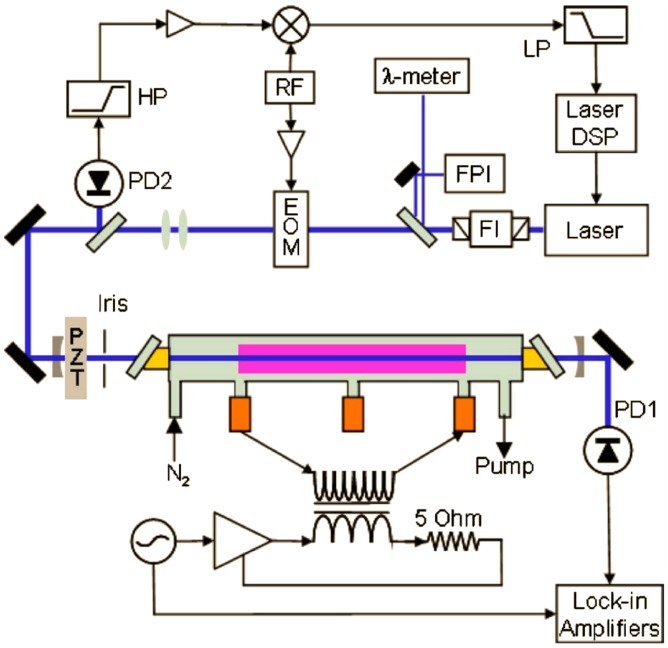

Figure 3.1: Experimental Setup.

and a Faraday isolator is placed at the output of the laser to prevent mode hops owing to optical feedback. Sidebands are generated by using an electro-optic modulator (at 8.1 MHz), and the output of the photodiode monitoring the back-reflection is sent through a high-pass (1.6 kHz) filter, amplified (24 dB), and then mixed with the RF modulation frequency and low-pass filtered (1.9 MHz) to produce an error signal that can be fed into the lasers control circuitry to keep the laser on resonance with the cavity. The laser is scanned by applying a DC voltage to the cavity piezo; a continuous tuning range of ∼3.5 GHz has been routinely achieved. The laser frequency is measured by using both a FabryPerot interferometer (Toptica FPI-100) and a wavemeter (Bristol 621A-IR) with an accuracy of 70 MHz, and multiple contiguous ∼3.5 GHz scans can then be stitched together.

The transmitted light from the cavity is sent through bandpass filters to reduce plasma emission and then focused onto a photodiode, which is placed ∼2 m away from the plasma to further reduce the plasma emission. The output of this photodiode is sent to two lock-in amplifiers, both referenced to the plasma frequency, but with different sensitivities and different phases to optimize the discrimination between ion and neutral signals.

3.4 Results

A representative spectrum is shown in Fig. 3.2. One lock-in amplifier is primarily sensitive to molecular ion signals, in this case a close blend of the $Q_{11}(14)$ and $Q_{12}(6)$ transitions of the ν=1←0 band of the Meinel system ($A^2\Pi_u$-$X^2\Sigma_g^+$) of N_2^+. The observed frequency of this blend is in excellent agreement with that reported in a previous Fourier transform spectroscopy study of this band [30] and is illustrated by the vertical line in Fig. 3.2. The other lock-in is sensitive to neutral signals, in this case an unassigned transition that is likely part of the ν=4←4 band of the first positive ($B^3\Pi_g$-$A^3\Sigma_u^+$) system of N_2^* [81]. In contrast to direct absorption studies [102, 30, 81], in which neutrals and ions can be separated only by quantum mechanical assignment or by their differing response to plasma conditions such as pressure, they are clearly separable by their different line shapes and phases in the present experiment.

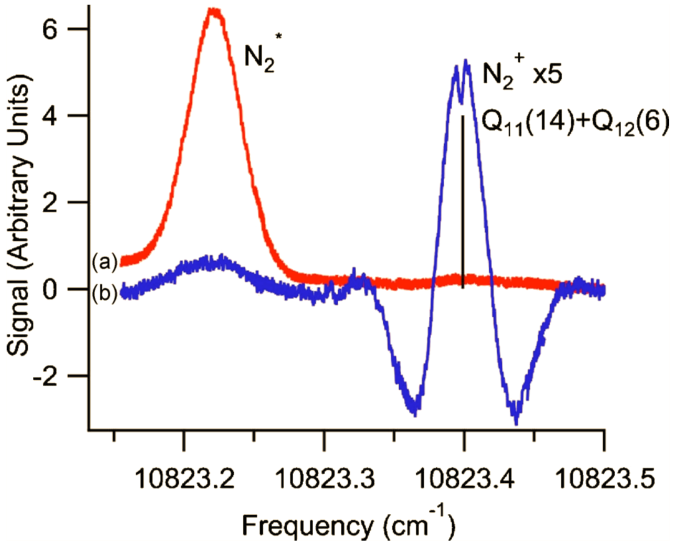

Figure 3.2: Spectral lines of (a) N_2^* and (b) N_2^+, recorded simultaneously by using two lock-in amplifiers with different phase settings.

The N_2^+ transitions show a line shape that is well described as a second derivative of a Gaussian (with a Lamb dip, discussed below). The velocity modulation of the ions could be viewed as a wavelength modulation of the two counterpropagating laser beams in the cavity (in the ions rest frame), thus yielding a familiar $2f$ line shape. The lock-in signal from the velocity modulation can also be simulated by assuming that the ions have a Gaussian (thermal) distribution of velocities, but that the center velocity oscillates in time, in phase with the discharge voltage. Trace a in Figure 3.3 shows the time-dependent absorption of N_2^+ at line center, owing to ions with zero velocity along the cavity axis; such ions are most abundant at the zero crossing of the discharge voltage, as there is no electric field to cause a net drift velocity. Trace c shows the N_2^+ absorption far from the line center, owing to ions with a large velocity along the cavity axis; such ions are

most abundant at the maxima of the discharge voltage, and thus appear 180° out of phase from the ions in trace a. This qualitatively explains why the wings of the N_2^+ line show up with the opposite sign from the line center in the lock-in signal shown in Fig. 2. The N_2^+ transitions do not show significant concentration or amplitude modulation, which would appear as an ordinary Gaussian line shape.

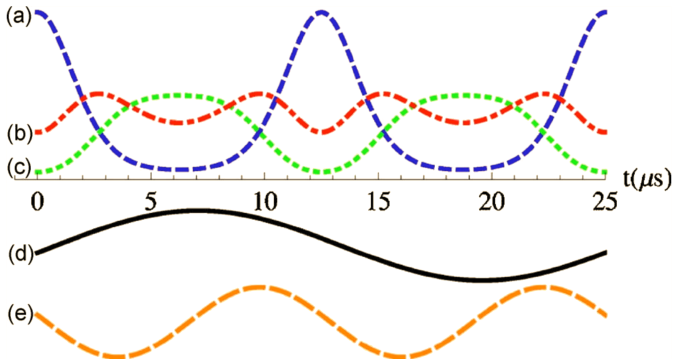

Figure 3.3: Simulated time-dependence of the N_2^+ absorption, a, at line center; b, at the zero-crossing; and, c, at the minimum, compared with, d, the electric field. Trace e, time-dependent concentration of N_2^*.

In contrast, the N_2^* lines do appear with ordinary Gaussian line shapes, approximately 78° out of phase from the N_2^+ lines. These electronically excited nitrogen molecules are produced by impact with energetic electrons $\gtrsim$6.2 eV in the plasma, and their concentration is modulated by the discharge, but their velocity is unaffected. The observed value of the phase difference between N_2^* and N_2^+ is not understood at present, but is likely to be pressure dependent.

Because of the high-intensity laser field inside the cavity, many of the observed transitions exhibit Lamb dips, as evident in the N_2^+ line in Fig. 3.2. To our knowledge, this is the first time Lamb dips have been observed in molecular ion spectra by using tunable laser absorption spectroscopy. The only previous report of a Lamb dip in a molecular ion (DBr^+ [44]) involved a laser magnetic resonance approach, which may be less generally applicable than the present approach. With improved frequency calibration (e.g., with an optical frequency comb), it will be possible to measure the transition frequencies of molecular ions with greatly enhanced resolution and precision, relative to Doppler-limited spectroscopy. Accurate measurements of the width of the Lamb dips as a function of laser power and discharge pressure may also allow measurement of the pressure broadening coefficients, and thereby the ion-neutral collisional rate coefficients. At present, the observed linewidth of the Lamb dips ~130 MHz appears to be dominated by the frequency jitter of the cavity, as it is independent of the pressure of the discharge and it is considerably larger than is expected from unresolved hyperfine structure.

3.5 Discussion

The present work demonstrates the feasibility of cavity-enhanced velocity modulation spectroscopy, but several improvements to the current system will be needed before this technique can exceed the sensitivity of other established velocity modulation experiments (e.g., [71]. First, the noise level must be substantially reduced from the present value of an equivalent fractional absorption of $\sim 10^5$. When measurements are taken with the plasma off, the noise level is $\sim 10^7$, which indicates that our biggest source of noise is either electrical pickup or optical emission from the plasma. It should be possible to mitigate this noise by a combination of better shielding and/or a wavelength modulation scheme. The use of heterodyne spectroscopy with a sideband frequency equal to the free spectral range of the cavity, as in [114], may be especially useful in improving the noise level.

Second, the finesse of the cavity must be increased, to extend the effective absorption path length. The maximum finesse of our cavity is currently limited by the quality of our laser lock, which can be significantly improved by adding an acousto-optic modulator for high-frequency corrections. Additionally, we can improve the frequency stability of the system by locking the cavity to the laser instead of the reverse. The laser itself can then be locked either to its internal reference cavity or to an optical frequency comb. Another limit to our finesse is the presence of the Brewster windows, which could be avoided by mounting the cavity mirrors directly to the plasma cell, as in [102]. Ultimately, our current mirrors can be replaced by supermirrors to further increase the finesse. Finally, the signal can also be enhanced by using a longer discharge cell and by employing liquid nitrogen cooling to reduce the partition function of the molecular ions and the Doppler linewidth.

3.6 Conclusions

In this Letter we have demonstrated, for the first time to our knowledge, the use of cavity-enhanced spectroscopy together with velocity modulation. This combination offers the promise of substantially increasing the effective path length in velocity modulation experiments and permitting the study of extremely weak transitions of ions that can be produced in abundance, as well as the study of ions that are difficult to produce in quantity. In the limit of a high-finesse cavity combined with heterodyne spectroscopy [114], the S/N of the most sensitive velocity modulation experiments [38, 71] could be improved by a factor of 10^3 or more. Furthermore, the presence of Lamb dips in the cavity-enhanced spectra opens the door to high-precision molecular ion spectroscopy as well as measurements of ion-neutral collisional rate coefficients.

The authors are grateful to Prof. Benjamin Lev and Mr. Mingwu Lu for their advice concerning laser

locking electronics and techniques. This work has been supported by the NASA Laboratory Astrophysics program (NNX08AN82G), by an NSF CAREER award (CHE-0449592), by an Air Force Young Investigator award (FA9550-07-1-0128), and by the David and Lucile Packard Foundation.

Chapter 4

Noise Immune Cavity Enhanced Optical Heterodyne Velocity Modulation Spectroscopy

4.1 Abstract

The novel technique of cavity enhanced velocity modulation spectroscopy has recently been demonstrated as the first general absorption technique that allows for sub-Doppler spectroscopy of molecular ions while retaining ion-neutral discrimination. The previous experimental setup has been further improved with the addition of heterodyne detection in a NICE-OHMS setup. This improves the sensitivity by a factor of 50 while retaining sub-Doppler resolution and ion-neutral discrimination. Calibration was done with an optical frequency comb, and line centers for several N_2^+ lines have been determined to within an accuracy of 300 kHz.

4.2 Introduction

4.2.1 Velocity Modulation Spectroscopy

Laboratory spectroscopy of molecular ions is of great interest to a variety of fields, but is typically difficult because even in laboratory plasmas designed to observe a particular ion, the ion of interest has a very low concentration, typically orders of magnitude lower than that of any ambient neutral molecules in discharge cells. Velocity Modulation Spectroscopy (VMS) in positive column discharge cells has been the most commonly used technique in this field over the past several decades because it combines the advantages of relatively high ion density and ion-neutral discrimination. [93]

Recently, a new method of performing VMS has been demonstrated by placing the plasma discharge cell within an optical cavity in a technique we call Cavity Enhanced Velocity Modulation Spectroscopy (CEVMS). [89, 68] The optical cavity provides two major advantages over traditional VMS: greatly increased path length (about an order of magnitude greater than any previous VMS experiments, even with a cavity

This chapter was first published as: B. M. Siller, M. W. Porambo, A. A. Mills, and B. J. McCall, "Noise Immune Cavity Enhanced Optical Heterodyne Velocity Modulation Spectroscopy", *Optics Express*, **19**, 24822-24827 (2011).[90]

finesse of only 300) and the ability to observe a sub-Doppler Lamb dip for each spectral line (due to the high intracavity laser power and the perfectly overlapped counterpropagating beams induced by the optical cavity).

Although CEVMS showed much promise, its sensitivity was ultimately limited by noise in the laser-cavity lock, particularly noise that was induced by the high voltage AC plasma discharge. In the current work, the sensitivity limitations of CEVMS have been greatly improved by combining the technique with Noise Immune Cavity Enhanced Optical Heterodyne Molecular Spectroscopy (NICE-OHMS).

4.2.2 NICE-OHMS

NICE-OHMS is a technique that was first developed in the late 1990s [114], and has since been used with great success by several groups to observe spectra of many different neutral molecules with sensitivity unprecedented by other direct absorption spectroscopic techniques. [33]

The principle of NICE-OHMS is that while the laser carrier frequency is locked to an optical cavity mode, a set of FM sidebands are added to the laser, spaced at an integer multiple of the cavity free spectral range (FSR). Thus the carrier (laser center frequency) and both sidebands get coupled into, and out of, the cavity simultaneously. The transmitted beam is detected with a fast photodiode and demodulated at the heterodyne modulation frequency.

Because the two sidebands have the same intensity when no absorbers are present within the cavity and are 180° out of phase with one another, the positive and negative RF beat signals created by the sideband frequencies beating against the carrier frequency cancel each other out, causing NICE-OHMS to be a zero-background technique. When the frequency modulated laser is coupled through the optical cavity, any noise in the laser-cavity lock is the same for the carrier and both sidebands, so the demodulated signal is unaffected. Thus, NICE-OHMS allows for the path length enhancement of an optical cavity, a factor of $(2 \cdot Finesse/\pi)$, while not introducing any additional noise in the system beyond that of ordinary single-pass heterodyne spectroscopy.

An absorption signal is observed when one of the RF sidebands is absorbed more than the other, causing an imbalance in the two heterodyne beats, so they no longer add to zero. For any absorption, there is a corresponding dispersion, related by the Kramers-Kronig relations. [55] With heterodyne detection, it is possible to observe this dispersion signal, because a phase shift in the carrier frequency or either of the sideband frequencies also creates an imbalance in the beat signals, leading to a net signal. The net signal obtained from a phase shift of one of the laser frequencies is 90° out of phase with that obtained from absorption of one of the sidebands, so through phase-sensitive detection, it is possible to observe absorption

and dispersion independently of one another.

4.3 Experimental

The experimental setup is shown in Figure 4.1. It is similar to that previously used for cavity-enhanced velocity modulation experiments [89, 68], with the addition of a second electro optic modulator (EOM) and a high speed photodiode for heterodyne detection.

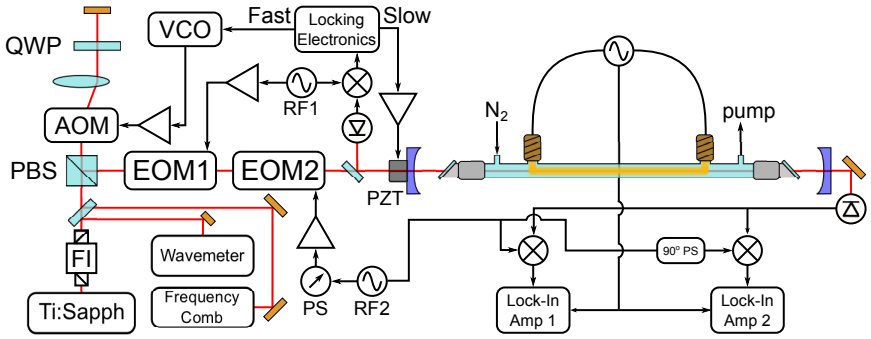

Figure 4.1: Experimental Layout. FI: Faraday isolator; PBS: polarizing beam splitter; AOM: acousto optic modulator; QWP: quarter wave plate; VCO: voltage controlled oscillator; EOM: electro optic modulator; PZT: piezo electric transducer; RF: radio frequency generator; PS: phase shifter.

The laser is double-passed through an acousto optic modulator that is resonant at 85 MHz, which red-shifts the laser frequency by 170 MHz and makes the pointing of the beam immune to changes in the AOM drive frequency. [24]

The laser is then passed through two electro optic modulators, which add two sets of RF sidebands to the laser frequency. The first EOM, which is non-resonant, adds 30 MHz sidebands with a small modulation index ($\beta \sim 0.01$). These sidebands are detected in the back-reflected signal off of the cavity, and are demodulated with an RF mixer to generate a Pound-Drever-Hall [25] error signal. That error signal is then processed with analog electronics, and split off into two components; slow corrections (up to 100 Hz) are sent to the cavity piezo, while faster corrections (up to 60 kHz) are sent to the voltage controlled oscillator (VCO) that drives the acousto optic modulator (AOM).

The second EOM, which is resonant, adds sidebands spaced at an integer multiple of the FSR of the optical cavity. The light transmitted through the cavity is detected with a fast photodiode. The AC portion of the detector signal is sent through an RF amplifier, then a power splitter that sends the signal to two mixers. The mixers are referenced to the sideband RF signal, but are set to be 90° out of phase with one another through a phase delay induced by a difference in cable lengths between the reference signal and the local oscillator (LO) input of the mixers. The overall detection phase is adjusted using an RF phase shifter

in the line between the RF generator and the amplifier that drives the heterodyne EOM.

Two different experimental setups were used to observe several lines in the $v = 1 \leftarrow 0$ band of the Meinel system ($A^2\Pi_u - X^2\Sigma_g^+$) of N_2^+. One setup used a 1 GHz resonant EOM to space the heterodyne sidebands at 9 cavity FSRs for observation of Doppler profiles and demonstration of ion-neutral discrimination. The other setup used a 113 MHz resonant EOM to space the sidebands at 1 cavity FSR for sub-Doppler studies of the observed Lamb dips.

The optical cavity used in both setups had a finesse of 300, which gave a cavity linewidth of 450 kHz. Throughout the course of a scan, the cavity length would change by 12 μm as the piezo was scanned, causing the FSR to change by approximately 1 kHz. To avoid increased noise near the end of the piezo travel, a feed-forward loop was implemented, in which the piezo voltage was scaled down, inverted, and sent to the DC FM input of the RF driver so the sideband spacing would track with the cavity FSR as the cavity length was scanned.

4.4 Results & Discussion

4.4.1 Sub-Doppler Lineshape Analysis

The general sub-Doppler NICE-OHMS lineshape function is somewhat complex because there are three laser frequencies amplified within the cavity, each with enough power to saturate a transition, but to different degrees. Each laser frequency present in the cavity can act as a pump and/or a probe for sub-Doppler spectroscopy. For example, the carrier can act as a pump while a sideband acts as a probe, producing a Lamb dip spaced halfway between the two frequencies. Thus, Lamb dips are observed spaced at half the sideband spacing. For significant modulation depth ($\beta \sim 1$), where maximum heterodyne signal intensity is obtained, second-order sidebands also add small contributions to the outer edges of the signals. The overall

sub-Doppler lineshape function is given by

$$\begin{aligned}\chi_{subDop}(\nu_d) = \{&A_1[\chi_{abs}(\nu_d - \frac{1}{2}\nu_{fm}) - \chi_{abs}(\nu_d + \frac{1}{2}\nu_{fm})] \\ &+A_2[\chi_{abs}(\nu_d - \nu_{fm}) - \chi_{abs}(\nu_d + \nu_{fm})] \\ &+A_3[\chi_{abs}(\nu_d - \frac{3}{2}\nu_{fm}) - \chi_{abs}(\nu_d + \frac{3}{2}\nu_{fm})]\}\sin\theta_{fm} \\ +\{&A_0[\chi_{disp}(\nu_d)] \\ &+A_1[\chi_{disp}(\nu_d - \frac{1}{2}\nu_{fm}) + \chi_{disp}(\nu_d + \frac{1}{2}\nu_{fm})] \\ &+A_2[\chi_{disp}(\nu_d - \nu_{fm}) + \chi_{disp}(\nu_d + \nu_{fm})]\} \\ &+A_3[\chi_{disp}(\nu_d - \frac{3}{2}\nu_{fm}) + \chi_{disp}(\nu_d + \frac{3}{2}\nu_{fm})]\}\cos\theta_{fm}\end{aligned} \tag{4.1}$$

where $\nu_d = \nu - \nu_0$ is the detuning of the laser center frequency, ν, from the transition center frequency, ν_0. ν_{fm} is the heterodyne modulation frequency and θ_{fm} is the heterodyne detection phase. $A_{0,1,2,3}$ are amplitudes related to the overall laser power and the modulation depth. In this work, these amplitudes are used as fit parameters with the constraint $A_i > A_{i+1}$.

χ_{abs} and χ_{disp} are general lineshape functions for absorption and dispersion profiles, respectively. In this work, pseudo-Voigt profiles [103] are used for both the absorption and dispersion lineshapes. χ_{abs} is simply a linear combination of the peak-normalized Gaussian and Lorentzian lineshape functions, while χ_{disp} is derived from χ_{abs} transformed by the Kramers-Kronig relations [55]. The lineshape functions are given by

$$\chi_{abs}(\nu) = \eta e^{-4\gamma^2} + (1-\eta)(\nu_0 w)\frac{\nu w}{(\nu^2 - \nu_0^2)^2 + \nu^2 w^2} \tag{4.2}$$

$$\chi_{disp}(\nu) = \eta\frac{2}{\sqrt{\pi}}e^{-\gamma^2}\int_0^\gamma e^{\gamma'^2}d\gamma' + (1-\eta)(\nu_0 w)\frac{\nu^2 - \nu_0^2}{(\nu^2 - \nu_0^2)^2 + \nu^2 w^2} \tag{4.3}$$

where w is the full width at half maximum (FWHM) for both Gaussian and Lorentzian profiles, ν_0 is the linecenter, η is the fractional Gaussian character of the lineshape, $(1-\eta)$ is the fractional Lorentzian character, and $\gamma = 2(\ln 2)^{1/2}(\nu - \nu_0)/w$.

The combination of concentration and velocity modulation of N_2^+, both of which occur at $2f$, causes the observed Doppler profile to be much different from those seen in other *fm*- and *wm*-NICE-OHMS setups that observe neutral molecules. In this work, no attempt was made at fitting the overall Doppler broadened lineshapes; the Doppler broadened profile was approximated by a third order polynomial near the linecenter that was used as a baseline for sub-Doppler fitting.

4.4.2 1 GHz Sideband Spacing

The 1 GHz system, with sidebands spaced at 9 FSRs, was used for Doppler-broadened scans. Figure 4.2 shows a typical scan with this system, collected with a 300 ms lock-in time constant, 100 ms delay between points, and approximately 10 MHz step size. With this setup, only a single mixer and lock-in amplifier were used, and the RF phase was set to be nearly pure dispersion, as evidenced by the presence of a strong central Lamb dip, which is expected to be absent from the pure absorption signal.

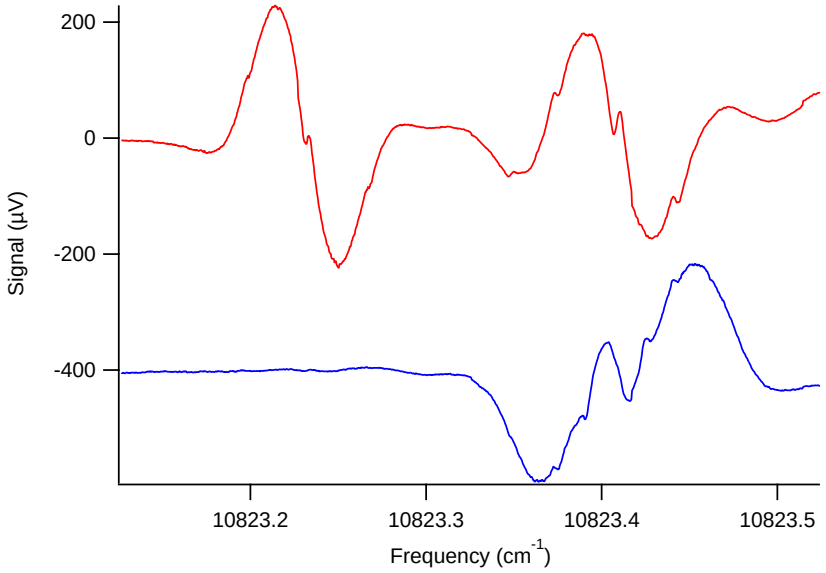

Figure 4.2: A scan with 1 GHz sideband spacing, demonstrating discrimination between N_2^+ and N_2^*. At the left is an unassigned transition of electronically excited neutral N_2. At the right is an unresolved blend of two N_2^+ lines, $Q_{12}(6)$ and $Q_{11}(14)$. The top and bottom traces are the X and Y channels of the lock-in amplifier, rotated in post-processing by 64°.

During data collection, the lock-in amplifier phase was set to zero. After collection of the data, computer software was used to rotate the phase of the signal with respect to the plasma frequency in order to minimize the amount of N_2^* signal present in the Y channel. The optimal angle was found to be $\theta = 64°$. This differs somewhat from the previously measured 78° [89], likely due to slightly different plasma conditions. Note that just the concentration of N_2^* is modulated in the plasma, so its Doppler-broadened profile is similar to other *fm*-NICE-OHMS lineshapes that are typically observed for neutral molecules. [63] With N_2^+, however, both the velocity and concentration are being modulated simultaneously, which leads to a more complex lineshape that cannot be isolated into a single phase.

4.4.3 113 MHz Sideband Spacing

For spectroscopy with sidebands spaced at a single cavity FSR, both RF mixers were used, and the lengths of cables going to the LO inputs of the two mixers were made such that the relative phases were 90° apart. The overall phase of the system was adjusted to optimize the isolation of absorption and dispersion signals using an electronic phase shifter on the input to the amplifier that drives EOM2.

A typical scan with the 113 MHz system, calibrated with an optical frequency comb, as described in [68], is shown in Figure 4.3. A single scan produces four orthogonal signals: absorption and dispersion, each with X and Y components. Absorption and dispersion signals are first separated using the 90° phase difference in the RF mixer references, then each of these is split into two components separated by 90° relative to the plasma frequency by mixers within the lock-in amplifiers. Fits were performed on the Lamb dips of the comb-calibrated scans using Equation 4.1, along with a cubic sloped baseline to approximate the Doppler profile near the line center.

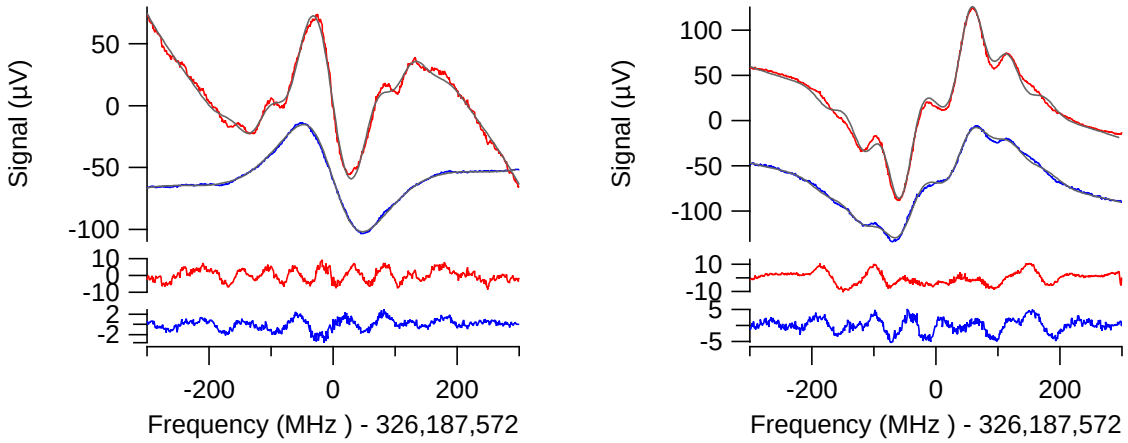

Figure 4.3: Dispersion (left) and absorption (right) Lamb dips of the $Q_{22}(13)$ line of N_2^+ observed in the 113 MHz configuration, calibrated with an optical frequency comb. Top, red: Y channel outputs of lock-ins. Bottom, blue: X channel outputs of lock-ins, offset vertically for clarity. Residuals are shown at the bottom.

Based on fits of several scans in alternating directions, calibrated with an optical frequency comb, the measured line center frequency was found to have a standard deviation of approximately 2 MHz. Because of the delayed response of the lock-in amplifiers used for demodulation, the determined line centers tend to be shifted in the direction of the scanning. By pairing and averaging pairs of scans in opposite directions, the measurement standard deviation can be reduced to ∼300 kHz. It was found that the linecenter frequencies determined previously in Ref [68] were all too high by 20 MHz due to an ambiguity in the determination of the sign of the comb carrier-envelope offset.

4.5 Conclusions and Future Work

The technique of cavity enhanced velocity modulation spectroscopy has been further improved by the addition of heterodyne detection to minimize the noise induced by the laser-cavity lock. This improvement has improved upon the achievable sensitivity of CEVMS by nearly two orders of magnitude while retaining ion-neutral discrimination. Combined with an optical frequency comb, linecenters can be determined to within 300 kHz.

Further improvement to this technique can be realized by moving to a higher finesse cavity to increase both the effective path length and the intracavity optical power. Moving to a higher finesse cavity would cause this technique to be more sensitive to mismatches in the cavity FSR and RF sideband frequency due to the narrower cavity resonances. This effect could be compensated for by actively locking the RF sideband frequency to the cavity FSR using the DeVoe-Brewer [22] method, rather than the less precise feed-forward loop that was used in this work. This technique could also be extended to the mid-infrared wavelength region by using a high power optical parametric oscillator (OPO) to observe a much greater variety of molecular ions.

Chapter 5

Lineshape Analysis

5.1 Introduction

The lineshapes produced by the techniques described in this thesis are quite complex, so a thorough discussion explaining the current state of our knowledge in the simulation and fitting of these lineshapes is presented in this chapter. The topics discussed here include absorption and dispersion, which can both be detected through heterodyne spectroscopy, as well as the lineshapes that result from the various types of modulation and demodulation that were utilized in this thesis work.

Concentration and velocity modulation were used from Chapter 3 onward, while heterodyne detection was first utilized in Chapter 4, and was used from that point onward. The introduction of heterodyne detection drastically improved the attainable S/N of the various spectroscopic systems, but also significantly complicated the observed lineshapes, not only from the addition of another level of modulation, but also from the introduction of sensitivity to dispersive signals, rather than just absorptive ones. Wavelength modulation was used only for the neutral methane spectroscopy presented in Appendix C. For all of the work presented in this thesis, both Doppler-broadened and sub-Doppler signals are observed, so analysis of both types of signals are presented in this chapter.

5.2 Absorption and Dispersion

When heterodyne detection, described in Section 5.3, is used, it is possible to observe absorption signals, or dispersion signals, or both absorption and dispersion simultaneously through separate detection channels. [10] The purpose of this section is to provide a physical explanation of absorption and dispersion, and how they relate to one another. The next section explains how the fundamental lineshapes of absorption and dispersion produce experimental lineshapes in heterodyne spectrometers.

Physically, dispersion and absorption correspond to the real and imaginary components of the index of refraction, respectively. A change in the real part of the index of refraction of light induces a net phase

shift of that light relative to the phase without the dispersive element in the system. The Kramers-Kronig relations [55] describe the relationship between absorptive and dispersive lineshapes. These lineshapes can be derived from the condition of causality, and one of the simplest equations directly relating absorption and dispersion is given by [97]

$$n(\omega_r) = 1 + \frac{c}{\pi} \lim_{\epsilon \to 0^+} \int_0^\infty \frac{\alpha(\omega_a) \mathrm{d}\omega_a}{\omega_a^2 - (\omega_r + \imath\epsilon)^2} \tag{5.1}$$

This equation can be used to compute the dispersion profile for any possible absorption profile, no matter how obscure, although it may not be possible to evaluate the integral symbolically. The two most common lineshapes, Gaussian and Lorentzian, are those that are used for the basis of all following lineshape simulation in this chapter. Lorentzian dispersion profiles have a simple symbolic representation that can be derived from the Lorentzian absorption profile and Equation 5.1, while the same is not true for Gaussian profiles. Rather, computation of the Gaussian dispersion lineshape requires numerical integration. Fortunately, the form of this numeric integral is very common in mathematics, and is called the Dawson Function, or Dawson Integral. This function is built into many mathematical modeling and data processing programs, so manual numerical integration is not generally necessary. Gaussian and Lorentzian profiles are shown in Figures 5.1 and 5.2, respectively; each figure shows both absorption and dispersion profiles

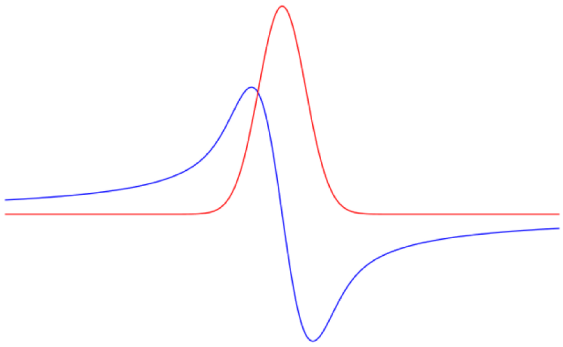

Figure 5.1: Gaussian absorption (red) and dispersion (blue) profiles.

5.3 Heterodyne Spectroscopy

Heterodyne techniques are often used in laser spectroscopy in an attempt to minimize experimental noise in a given spectrometer, as many sources of noise (laser intensity, acoustic, etc.) tend to scale proportional to 1/frequency. Heterodyne modulation is typically performed by modulating either the laser frequency or

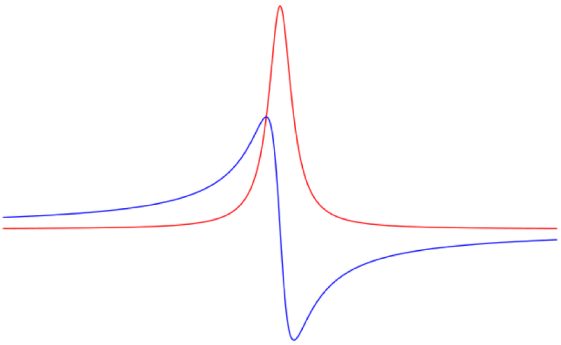

Figure 5.2: Lorentzian absorption (red) and dispersion (blue) profiles.

phase at radio frequencies (RF), most often in the range of ∼100 MHz to 1 GHz. In addition to decreasing the detection noise in a system, heterodyne detection provides the added advantage of enabling detection of both absorption and dispersion profiles for each observed molecular transition.

The basic idea of heterodyne spectroscopy is to modulate the laser frequency (or phase) fast enough to generate RF sidebands on the primary (carrier) laser frequency, as shown in Figure 5.3. The spacing of the sidebands from the carrier is determined by the frequency of the applied modulation, while the amplitude of the sidebands is dependent on the amplitude of the applied modulation, typically expressed in terms of the modulation index (β).

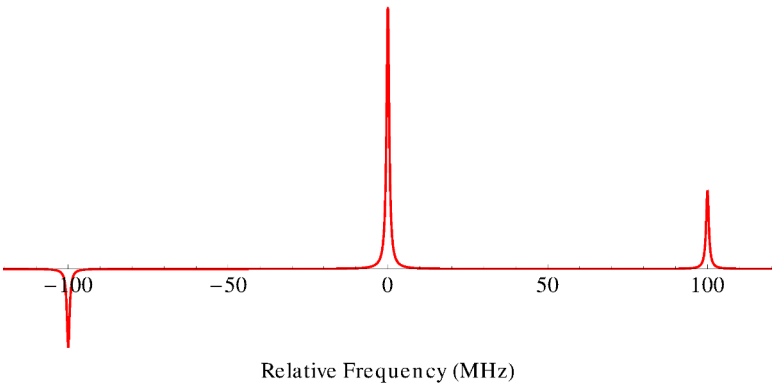

Figure 5.3: The spectrum of an RF-modulated laser. Note the strong carrier at the laser center frequency and the smaller sidebands spaced from the carrier at a frequency equal to the applied modulation frequency (100 MHz in this example).

The amplitudes of the carrier and all orders of sidebands are given by the simple expression $E_0 \times J_n(\beta)$, where n is the order of sideband, E_0 is the overall laser amplitude and $J_n(\beta)$ is the n^{th} order Bessel function of the first kind. Most implementations of heterodyne spectroscopy attempt to keep the value of β small

enough to make 2nd, while still keeping it large enough to detect the desired beat signal between the carrier and each sideband.

A beat signal is generated between each pair of laser frequencies present. Two of these beats occur at the heterodyne modulation frequency: the one between the carrier and the positive sideband, and the one between the carrier and the negative sideband. When none of the frequencies are absorbed or dispersed, the intensity of the positive and negative beats are given by $I_0 J_0(\beta) J_1(\beta)$ and $I_0 J_0(\beta) J_{-1}(\beta)$, respectively. Because Bessel functions have the property $J_{-n}(x) = -J_n(x)$, it is easy to see that these two beats have the same absolute intensity, but are 180° out of phase with one another, and thus add to zero.

When one of the sidebands is absorbed so that the two sidebands are no longer exactly equal in amplitude, the two beats no longer balance each other out, and a net RF signal is generated, as shown in Figure 5.4. This generated signal is exactly in-phase with the unabsorbed sideband beat phase, and its amplitude is determined by the magnitude of the absorption responsible for it. Note that absorption of the carrier frequency has no effect on the net beat signal, because both sideband beats are affected by the same amount, and no imbalance is created.

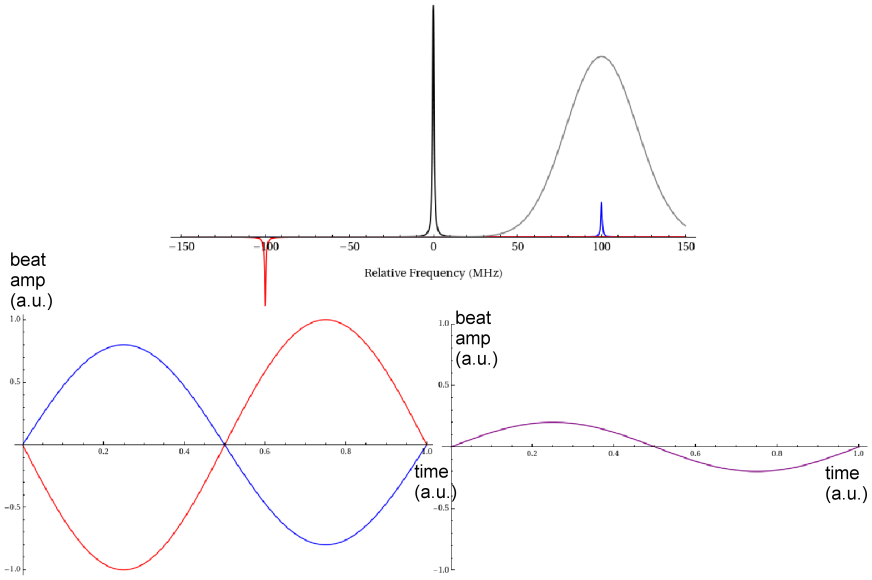

Figure 5.4: A graphical representation showing how absorption of one heterodyne sideband leads to a net beat signal over the course of one cycle of the RF modulation. Top: the laser spectrum, showing the positive (blue) sideband being slightly absorbed. Lower left: the color-coded beat signal generated by the positive (blue) and negative (red) sidebands beating with the carrier; note the difference in amplitude. Lower right: the net beat signal (purple) from adding the two individual beats. Note the difference in phase between this net beat signal and the one shown in Figure 5.5

Likewise, when one of the sidebands is dispersed (phase-shifted), the beats generated by the two sidebands no longer cancel one another out, and a net beat signal is generated, as shown in Figure 5.5. The generated

net beat signal is exactly 90° out of phase with the two contributing beats in the limit of small phase shifts. Even for large phase shifts, this net signal is still approximately 90° out of phase with any generated absorption signal. Unlike the case of absorption, the net signal is also sensitive to dispersion of the carrier frequency. Because shifting the phase of the carrier has the opposite effect on each beat as shifting the sideband, the phase of the carrier dispersion signal is 180° out of phase with the net signals from sideband dispersion. And because a phase shift in the carrier affects both sideband beats, it has twice the amplitude of the net beat from a phase shift of just one of the sidebands.

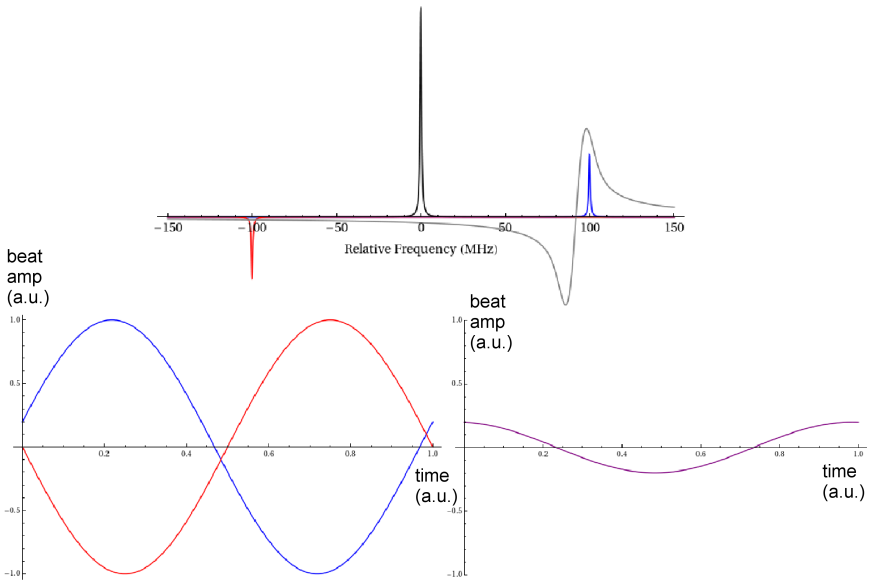

Figure 5.5: A graphical representation showing how dispersion of one heterodyne sideband leads to a net beat signal over the course of one cycle of the RF modulation. Top: the laser spectrum, showing the positive (blue) sideband being slightly dispersed. Lower left: the color-coded beat signal generated by the positive (blue) and negative (red) sidebands beating with the carrier; note the difference in phases. Lower right: the net beat signal (purple) from adding the two individual beats. Note the difference in phase between this net beat signal and the one shown in Figure 5.4

By comparing the net beat signals in Figures 5.4 and 5.5, which represent absorption and dispersion, respectively, we can see that the net beats generated by these two phenomena are 90° out of phase with one another with respect to the heterodyne modulation frequency. Typically, heterodyne experiments use phase-sensitive detection in the form of an RF mixer to demodulate the signal. By tuning the phase of the mixer reference signal, it is possible to selectively observe either absorption or dispersion, or some linear combination of both. Often, the detector signal is split into two separate mixers referenced to be 90° out of phase with one another, and the overall detection phase is tuned to isolate the absorption signal in one detection channel and dispersion in the other detection channel.

With the physical understanding of the mechanism behind heterodyne beat signal generation, it is

straightforward to determine overall lineshapes for detection at any phase. In the pure absorption phase, each of the two sidebands samples the overall absorption profile in turn as the laser wavelength is scanned. The net result is two independent contributions, one positive and one negative, from the two sidebands, as shown in Figure 5.6. Likewise, the dispersion profile shows the sidebands each sampling the lineshape in turn, but with the addition of the carrier contribution that is inverted with respect to the sideband contributions, and is also twice the intensity. For each absorption and dispersion, the net overall signal is simply the sum of the contributions of the three laser frequency components.

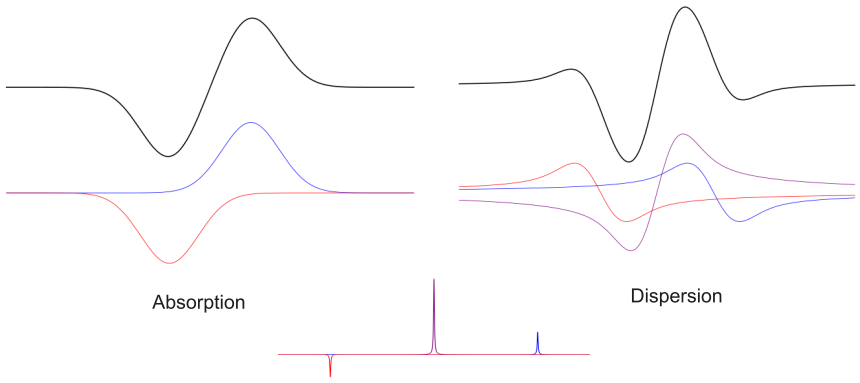

Figure 5.6: Black: net absorption and dispersion signals for a typical heterodyne experiment. Red, Blue: contributions of the negative and positive sidebands to the overall signal profiles. Purple: carrier contribution to the dispersion profile. Below: a laser frequency spectrum with colors of the various frequency components corresponding to the lineshape contributions above.

The lineshape depiction shown in Figure 5.6 shows how the signals appear when the heterodyne sideband spacing is comparable to the FWHM of the line being scanned over, but the lineshapes may look significantly different when the heterodyne modulation frequency is either much larger or much smaller than the transition linewidth.

In the limit of small heterodyne modulation frequency, the absorption profile appears as a simple first derivative of the natural absorption lineshape, while the dispersion profile appears as a second derivative of the natural dispersion lineshape. In this case, heterodyne absorption can be thought of as sampling two points along the absorption profile and subtracting one from another, which is one of the simplest ways of taking a numerical derivative of a function. Dispersion, on the other hand, has a third component, the carrier frequency, which is twice as large as the other two. Thus, sampling dispersion relies on taking some central point, multiplying the function at that point by two, then subtracting the values of the function that are on either side of the central point. In this way, probing dispersion is probing the curvature, or second derivative, of a function.

The other limit, in which heterodyne sidebands are spaced by much more than the linewidth of the feature of interest, is common in sub-Doppler saturation spectroscopy, where linewidths are often sub-MHz while heterodyne modulation frequencies are still typically $\gtrsim$100 MHz. In this case, each laser frequency essentially probes its own lineshape for both absorption and dispersion, with essentially no contributions from the other components of the overall lineshape.

5.4 Velocity Modulation Spectroscopy

Velocity modulation spectroscopy (VMS) was first developed in 1983 [41], and since that time, has been used to study over 50 molecular ions in the laboratory. [92] This technique relies on striking a plasma discharge with alternating polarity while passing a laser through the discharge cell parallel to the electrode-induced electric field. Any ions present are Doppler-shifted toward the oppositely charged electrode, i.e. positive ions move toward the cathode while negative ions move toward the anode.

The ions' absorption profiles are alternately shifted red and blue with respect to the laser. When the laser frequency is slightly detuned from an ionic absorption, the ions' Doppler profile moves in and out of resonance with the laser frequency. This causes the velocity modulation of the ions to be translated into an intensity modulation of the laser, which can be detected using a lock-in amplifier on the detector output.

Detecting the velocity-modulated signal rather then the DC absorption of the plasma has several advantages. First and foremost, it enables ion-neutral discrimination, which comes from the fact that neutral molecules are not directly accelerated by the electric field. This aspect is very important given than neutral molecules tend to be $\sim$6 orders of magnitude more abundant than ions in these plasma discharges. Neutral molecules can be slightly modulated, however, by electron impact or by having an ions recombine while retaining its prior velocity, so it is possible for them to interfere somewhat with ion detection, but certainly not to the degree they would interfere in a DC detection scheme.

Oftentimes, scans are collected multiple times (or signals are split to multiple lock-in amplifiers) with lock-in settings of $1f$ and $2f$. The $1f$ detection is primarily sensitive to velocity modulation, while $2f$ detection is sensitive primarily to concentration modulation. Thus, any signals that appear significantly stronger in $2f$ detection are typically attributed to neutral molecules, while the ones that are stronger in $1f$ are attributed to ions. Velocity modulation spectroscopy also allows for easy determination of which signals are from positively charged ions and which are from negatively charged ones, because these two signals are 180° out of phase with one another.

5.5 Velocity and Concentration Modulation

Traditionally, the lasers used for VMS have either been set up with a single pass through the cell, or in a unidirectional multipass configuration. Sometimes, the laser is split into two paths and directed separately through the multipass cell in opposite directions, with the signals from the counterpropagating beams subtracted from one another before going through the lock-in amplifier demodulation to double the total amount of signal while subtracting noise. Recently, there has also been work done using a unidirectional ring cavity. [91] All of these methods rely on the laser only passing through the cell in one direction at a time, so they are only sensitive to velocity modulation, and not concentration modulation (except perhaps for any asymmetry in the plasma discharge, which is typically small). Technically, the multipass cells can have counterpropagating beams, but because the two directions are subtracted from one another, this works out to be functionally equivalent to the other unidirectional techniques in terms of lineshapes and detection schemes.

With the technique of cavity enhanced velocity modulation spectroscopy (CEVMS), which uses a two-mirror cavity positioned around a plasma discharge cell, the laser is passing through the plasma both directions simultaneously, and the net signal encoded in the laser intensity is the sum of the absorptions from the entire round trip. The major advantages of this technique are path length enhancement and the enabling of saturation spectroscopy. Even with a fairly modest finesse of $\sim$200, we are able to attain an order of magnitude greater effective path length through the cell than was previously possible with the best non-cavity-enhanced multipass cells. Not only is the path length enhanced, but so is the intracavity power. This power enhancement factor of F/π is necessary to saturate transitions of molecular ions, which have much larger relaxation rates (and thus lower saturation parameters for given laser power) than most neutral molecules.

The biggest disadvantage to integrating cavity enhancement with VMS is that the $1f$ demodulated signal vanishes due to the symmetry of the cavity, so $2f$ demodulation must be performed. This makes detection sensitive to concentration modulation, both of excited neutral species and of the ions of interest. We have shown that the phase of detection can be set to reduce or eliminate neutral contributions in at least one of the detection channels, while still retaining ion signal in that channel. [89, 90] This means that ion-neutral discrimination is retained, although it takes a bit more work in setting the detection phase appropriately, which may prove more difficult in more complex plasmas with multiple neutral species each being modulated at its own phase.

The other disadvantage with CEVMS is that the lineshapes of ions end up being significantly more complicated than the ones observed with ordinary VMS due to the sensitivity to both velocity and concentration

modulation of the ions of interest. In ordinary VMS, the observed lineshapes can be approximated quite well by the first derivative of an ordinary Gaussian function. Extending that idea to CEVMS would imply that an ordinary second derivative would fit the acquired data nicely, given that it is the natural extension from $1f$ to $2f$, but we have observed that that is not the case. Rather, we must explicitly take into account the effects of concentration modulation to be able to model anything even closely resembling the observed lineshapes. Here I will describe my efforts to model the lineshapes, starting with simple lineshape functions, then factoring in velocity modulation, and finally adding in concentration modulation as well. Unfortunately, the final solutions will be in integral notation with no apparent analytical simplification, so the final equations won't be in a convenient notation for performing fits of acquired data, but they do at least provide qualitative comparisons with observed data.

For simplicity, all of the following equations will be centered at zero on the frequency axis, and all frequency deviations (heterodyne splitting, velocity modulation amplitude) will be relative to the transition Doppler linewidth. The derivation is in very general terms, so it is almost trivial to substitute different lineshape functions in the end, but including those from the start makes the equations somewhat more cumbersome to work with and understand.

First, we'll start with the general absorption and dispersion lineshape functions:

$$\chi_{\text{abs}}(\nu_d) = e^{-\nu_d^2} \tag{5.2}$$

$$\chi_{\text{disp}}(\nu_d) = e^{-\nu_d^2} \int_0^{\nu_d} e^{x^2} dx \tag{5.3}$$

where ν_d is the laser detuning from the transition center frequency and x is an integration variable that falls out of the equation upon evaluation of the integral. Note that χ_{disp} is simply the Dawson function $D_+(\nu)$, which is built into many computer graphing and mathematical modeling programs. Now, if we want to factor in heterodyne detection, we have

$$\chi_{\text{absHet}}(\nu_d) = \chi_{\text{abs}}(\nu_d - \nu_h) - \chi_{\text{abs}}(\nu_d + \nu_h) \tag{5.4}$$

$$\chi_{\text{dispHet}}(\nu_d) = 2\chi_{\text{disp}}(\nu_d) - \chi_{\text{disp}}(\nu_d - \nu_h) - \chi_{\text{disp}}(\nu_d + \nu_h) \tag{5.5}$$

where ν_h is the heterodyne modulation frequency. From this point forward, I will use the generic lineshape function $\chi(\nu)$, where any of the lineshapes from equations 5.3 or 5.5 can be substituted for $\chi(\nu)$, depending on the mode and phase of detection. For a single-pass velocity modulation experiment, the time-dependent

velocity distribution is simply

$$F(t) = A \times \chi(\nu_d + \nu_a \cos(2\pi t)) \tag{5.6}$$

where t is time, ν_a is the maximum frequency deviation of the center of the Doppler distribution induced by the electric field upon the ions, and A is an amplitude determined through Beer's law by the ion density, transition strength, and effective path length through the plasma. This assumes that the velocity modulation is purely sinusoidal, which may or may not be the case for a given system. At low frequencies (a few kHz or less), the velocity modulation tends to be more square than sinusoidal. [29] But the systems described in this thesis work at sufficiently high frequencies ($\sim$40 kHz) that sinusoidal modulation seems reasonable. Equation 5.6 is valid for single-pass or unidirectional multipass systems, but to describe our cavity-enhaced spectrometers, we need to take into account the bidirectionality of the laser. When the Doppler distribution is red-shifted with the forward-propagating laser passes, it is blue-shifted with respect to the reverse-propagating passes. This makes the two directions see Doppler distributions that are effectively 180° out of phase with one another. The sum of the absorptions of both directions of beams is given by

$$F(t) = A \times \{\chi(\nu_d + \nu_a \cos(2\pi t)) - \chi(\nu_d - \nu_a \cos(2\pi t))\} \tag{5.7}$$

where the two terms being added together correspond to the forward- and reverse-propagating components of the laser through the velocity modulated discharge cell. Equation 5.7 assumes a constant ion population throughout the course of a discharge cycle. To account for the time-dependent concentration, we can replace the constant A with a time-dependent function

$$A(t) = (1 - \alpha) + \alpha \cos^2(2\pi t + \phi) \tag{5.8}$$

where α is the depth of the concentration modulation and ϕ is the phase difference between the peak ion concentration and the peak ion velocity. Values of α can range from 0, corresponding to constant ion density, to 1, corresponding to the ion population being completely destroyed and re-created with each half-cycle of the plasma discharge. Like the average drift velocity of the ions, the concentration of the ions may or may not vary sinusoidally with the plasma discharge, so a functional form that was easy to work with was chosen. In the future, we may experiment with a square wave concentration modulation or a ramp, with rise and fall rates corresponding to formation and destruction rates. But because the lock-in demodulation selects a single Fourier coefficient of the signal modulation, we don't expect that different functional forms will have large effects on the qualitative analysis of these results.

Several simulations of CEVMS signals for various levels of concentration modulation are shown in Figure 5.7. This initial simulation was performed with concentration and velocity modulation phases set equal to one another. Although this simple assumption probably isn't entirely correct, it does allow for a series of graphs to be generated that shows an interesting trend. With pure velocity concentration (top graph of Figure 5.7), the lineshape approximates a second derivative of a Gaussian lineshape function. This is to be expected, as traditional VMS experiments, which are insensitive to concentration modulation, produce first derivative lineshapes, and the higher level of demodulation adds a second derivative to the overall lineshape. When concentration modulation dominates (in the lower graphs in Figure 5.7), the lineshape appears almost purely Gaussian. This lineshape is also not surprising because that is the lineshape that the excited neutral molecules, which are only concentration modulated, produced.

Adding in heterodyne detection in a NICE-OHVMS setup further complicates the lineshape, both through the extra layer of modulation/demodulation and through enabling the detection of dispersion in addition to absorption signals. Figure 5.8 shows the same simulations that were done in Figure 5.7, but with heterodyne lineshapes. This initial simulation was also done assuming that the concentration and velocity modulation were exactly in phase with one another. Although this is likely not the case for real-world conditions, it does show an interesting trend. Absorption and dispersion each start with 4 "lobes" contributing to the overall lineshape without any concentration modulation. As more concentration modulation is added into the simulation, the outer lobes become larger while suppressing the inner lobes, until the lineshape evolves to the point of having only two lobes.

The simulations presented in Figures 5.7 and 5.8 were performed with the velocity and concentration phases set equal to one another, meaning that the peak ion concentration occurs at the same time as the peak ion velocity, with both concentration and velocity varying sinusoidally over time. This condition allows for all of the signal going to each lock-in amplifier to be isolated into a single detection phase, so careful selection of lock-in demodulation can nullify one of the two lock-in channels in a two-channel lock-in set to X/Y demodulation mode. From our experimental studies, this is typically not possible, indicating that the concentration and velocity modulation phases are not identical.

Figures 5.9 and 5.10 show the effects of varying the velocity/concentration relative phase while holding the absolute amount of concentration modulation fixed at 25% of the total ion population. Note that each graph now has a second trace, corresponding to the quadrature lock-in detection channel. This second trace was not shown in Figures 5.8 and 5.7 because it was zero for all frequencies and all levels of concentration modulation.

One interesting trend in these simulations is that the total peak-to-peak signal actually increases in the

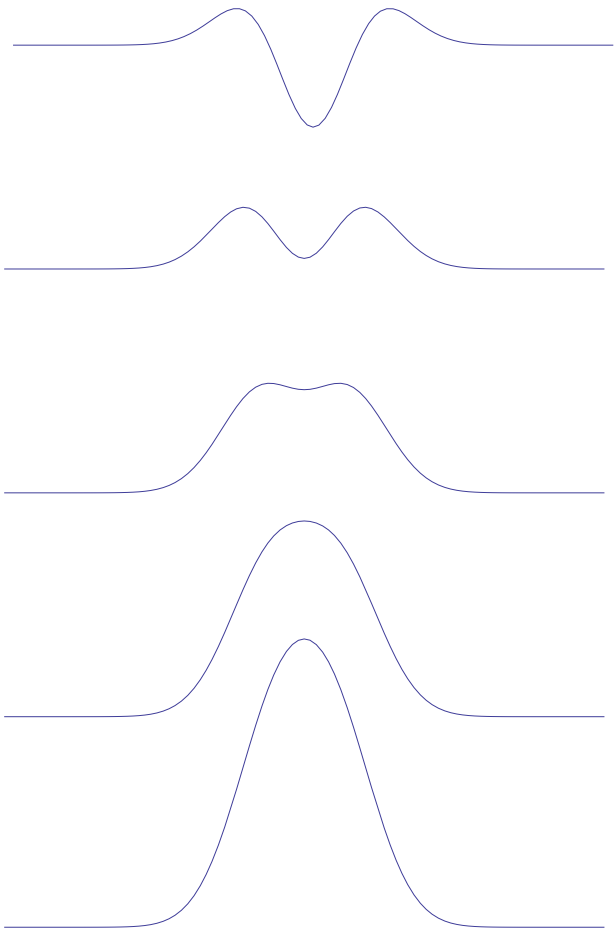

Figure 5.7: Simulations of CEVMS lineshapes for various levels of concentration modulation: (from top to bottom) 0, 25, 50, 75, and 100% concentration modulation depth ($\alpha = 0$ to 1 in steps of 0.25). For these simulations, the concentration modulation was set to be in phase with the velocity modulation, so all of the signal can be isolated into a single channel for each simulation. Both horizontal and vertical axes are the same for all graphs.

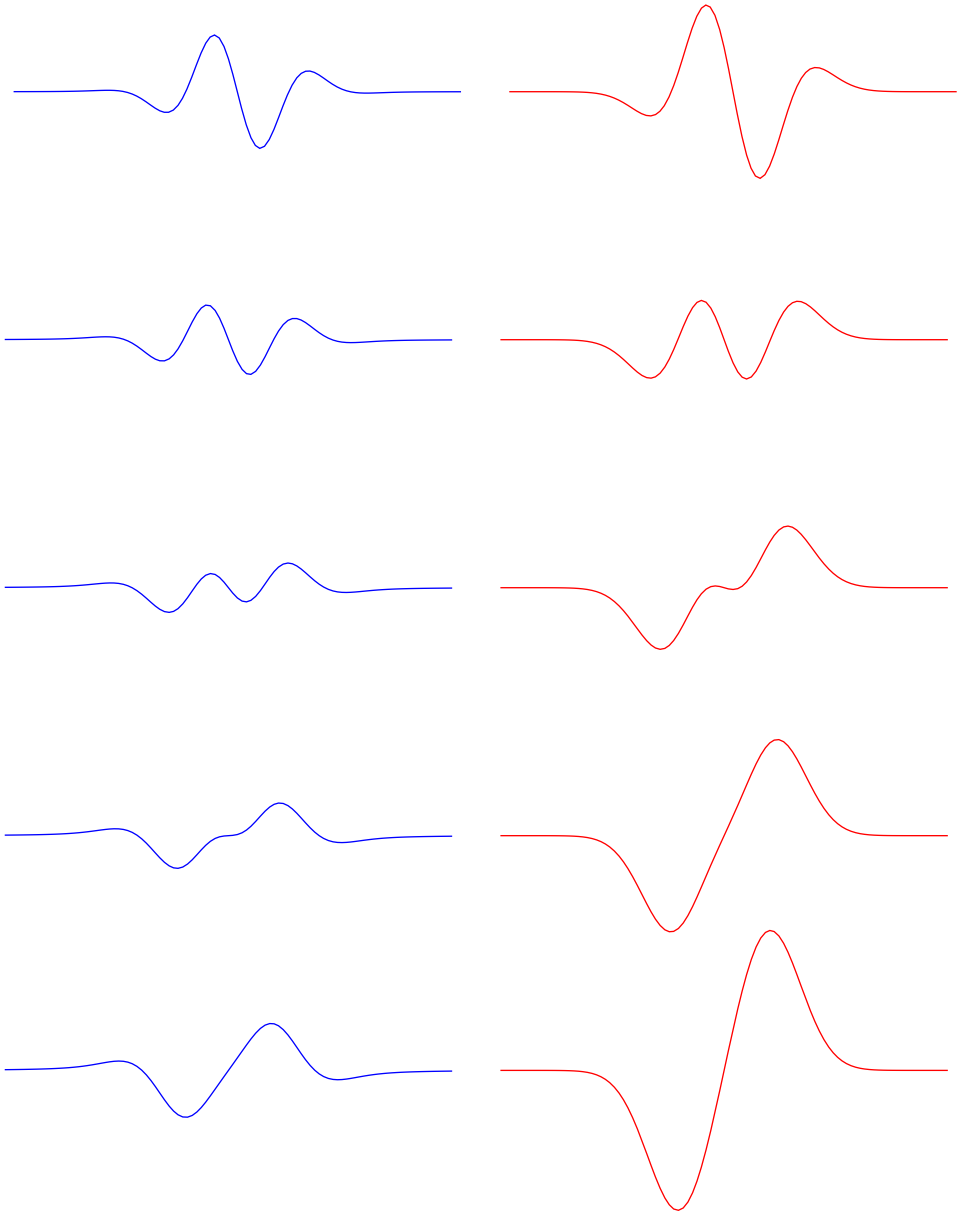

Figure 5.8: Simulations of NICE-OHVMS lineshapes for both dispersion (blue) and absorption (red) detection phases for various levels of concentration modulation: (from top to bottom) 0, 25, 50, 75, and 100% concentration modulation depth (α = 0 to 1 in steps of 0.25). For these simulations, the concentration modulation was set to be in phase with the velocity modulation, so all of the signal can be isolated into two channels for each simulation. Both horizontal and vertical axes are the same for all graphs.

in-phase channel as the concentration and velocity modulation become more and more out of phase with one another, leading to the maximum amount of signal when the two modulations are 90° out of phase with one another. It is also interesting that the quadrature detection channel is nullified not only at 0°, but also at 90° separation of concentration and velocity modulation phase separation. In our work, both with N_2^+ and with H_3^+, we have seen that the two lock-in channels tend to be somewhat comparable in signal amplitude, differing by less than a factor of 4, and often by much less than that. This would seem to indicate that concentration modulation is moderately phase shifted from velocity modulation, rather than being near 0 or 90° shifted.

Although the simulations presented in this chapter provide a qualitative picture showing that we understand the physical processes contributing to the overall Doppler-broadened lineshapes for both CEVMS and NICE-OHVMS experiments, they have not yet been used to provide any quantitative measure of the various parameters that go into creating the simulations. There are two major challenges with providing a more quantitative analysis than was presented here. First, all of the simulations rely on numerical integration rather than producing analytical expressions for lineshapes, making fitting to actual data difficult. Second, there is a very large parameter space that needs to be explored if any attempt at determining actual experimental parameters is to be made. The simulations presented here have only explored the effects of concentration modulation amplitude and phase. There is still overall detection phase (for both heterodyne and plasma frequency demodulation), peak velocity modulation Doppler shift, and heterodyne sideband spacing relative to Doppler width. Even beyond these simple parameters, it is also possible that the velocity and concentration modulation are not purely sinusoidal, and that the overall Doppler lineshape is not a pure Gaussian throughout the course of a discharge cycle, as it may be not only shifted but also distorted by the applied voltage. In short, the work presented in this chapter is only a first step into the larger problem of someday being able to actually fit real experimental data using this type of analysis.

5.6 Sub-Doppler Features

The sub-Doppler features of the observed lineshapes are somewhat simpler than the overall Doppler broadened shape. Because sub-Doppler Lamb dips are dependent on just the zero-velocity ion population, we don't have to be concerned with that population shifting in frequency with respect to the laser. The zero-velocity population does change throughout the course of a discharge cycle, both with the overall ion population (fewer total ions correspond to lower zero-velocity population) and with shifting of the Doppler profile (smaller shift corresponds to larger zero-velocity population).

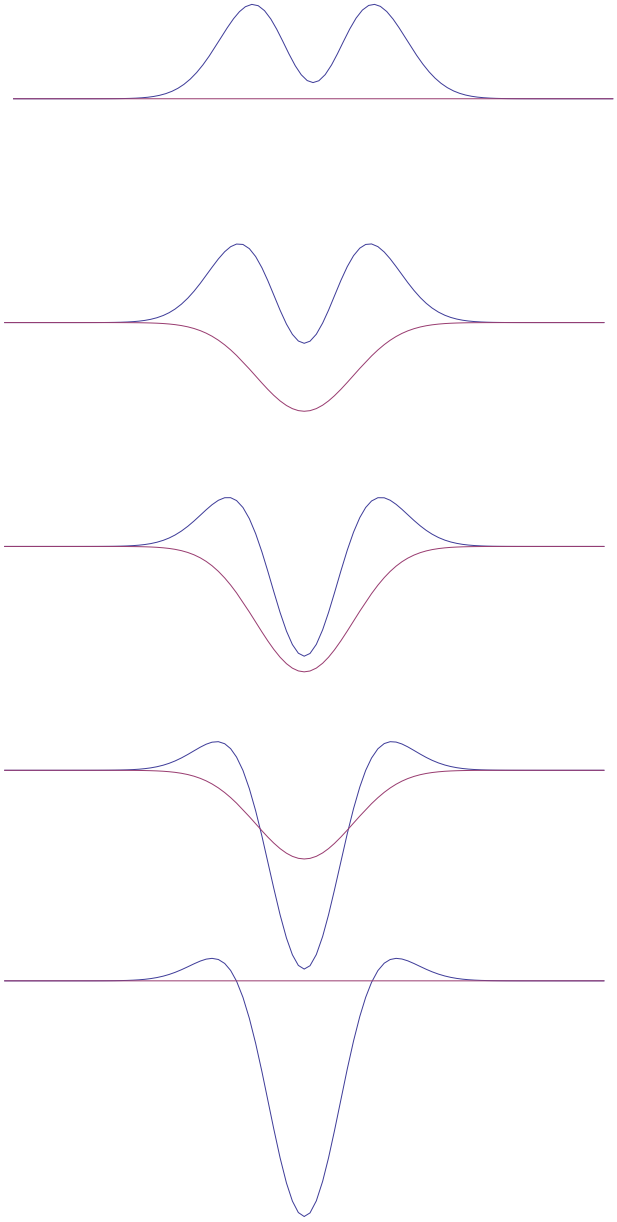

Figure 5.9: Simulations of CEVMS lineshapes with a constant 25% concentration modulation, for various phases of concentration modulation relative to velocity modulation. From top to bottom, the phase differences are: 0, 22.5, 45, 67.5, and 90°. The two traces of each graph correspond to lock-in demodulation in phase (blue) and 90° out of phase (red) with the velocity modulation.

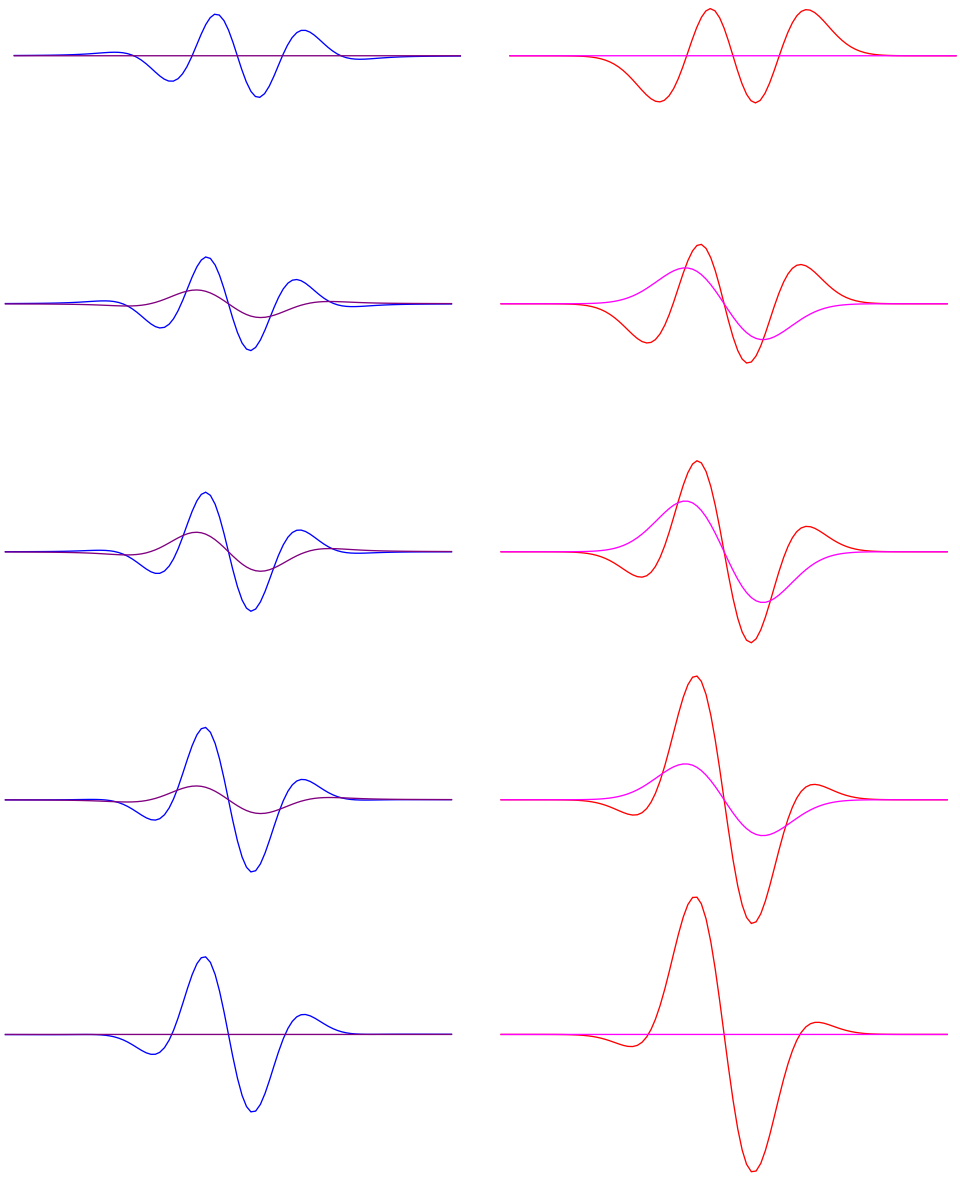

Figure 5.10: Simulations of NICE-OHVMS lineshapes with a constant 25% concentration modulation, for various phases of concentration modulation relative to velocity modulation. The left traces (blue, purple) correspond to dispersion signals, while the right traces (red, magenta) correspond to absorption signals. The two traces of each graph correspond to lock-in demodulation in phase (blue, red) and 90° out of phase (purple, magenta) with the velocity modulation. From top to bottom, the phase differences are: 0, 22.5, 45, 67.5, and 90°.

Thus, the sub-Doppler features essentially experience purely concentration modulation. A simple sinusoidal modulation of concentration leads to the exact same lineshapes as no modulation at all, so the Lamb dips would be expected to have ordinary unmodulated lineshapes, overlaid on the modulated Doppler profile. In fact, ordinary Voigt profiles tend to work fairly well at fitting, as can be seen in Chapter 4, but the fits still aren't perfect.

Although the center of the Lamb dips cannot shift with plasma modulation, it may be that the widths of the Lamb dips are not constant throughout the course of each cycle of the discharge. When the discharge voltage is at a zero-crossing, the collisional relaxation rate is determined primarily by ion-neutral collision dynamics, which have been well studied and are modeled quite well with Langevin dynamics. But when the discharge voltage is at a maximum, the ions are being accelerated through a bath of neutral molecules that are at rest (to within the Doppler distribution), so the collision rate may increase during that portion of the cycle, causing the Lamb dip linewidth to increase as well. Investigating the effects of varying Lamb dip width will be the target of future research and simulation.

Chapter 6

Ion Beam Spectroscopy

6.1 Abstract

We present the design and construction of a direct absorption ion beam spectrometer with several improvements over previous designs[17]. Recent advances in electrostatic optics have been implemented, along with a time of flight mass spectrometer that can be used simultaneously with optical spectroscopy. A noise immune cavity enhanced optical heterodyne molecular spectroscopy (NICE-OHMS) setup with a noise equivalent absorption of $2.3 \times 10^{-11}\,\mathrm{cm}^{-1}\,\mathrm{Hz}^{-1/2}$ is used to observe several N_2^+ transitions in the ion beam with linewidths of 120 MHz. An optical frequency comb is used for absolute laser frequency calibration to determine transition rest frequencies to within 1 MHz. This instrument provides rigorous ion/neutral discrimination and this work represents the first direct-absorption equivalent spectra of an electronic transition in an ion beam.

6.2 Introduction

The study of molecular ions is important in a number of fields, including physical chemistry, combustion chemistry, atmospheric chemistry [31], and astrochemistry [45, 73]. Ions are transient and reactive species, so even in plasma discharges, neutral molecules are typically around six or more orders of magnitude more abundant than the ions of interest. Early spectroscopic studies on glow discharges were often hampered by interfering signals from neutral absorbers [93]. The invention of velocity modulation spectroscopy (VMS) [41], which involves using a high voltage AC discharge to modulate the velocity of ions and a lock-in amplifier

This chapter was first published as: A. A. Mills, B. M. Siller, M. W. Porambo, M. Perera, H. Kreckel, and B. J. McCall,"Ultra-Sensitive High-Precision Spectroscopy of a Fast Molecular Ion Beam", *Journal of Chemical Physics*, **135**, 224201 (2012).[69]

Unlike the other chapters of this thesis that were written entirely by me (with input from coauthors), this chapter was written piecewise, with each author taking the sections which they were most knowledgeable of. I personally wrote the parts pertaining to optical spectroscopy, both in the experimental description and the results and discussion. I also did the final editing of all the sections together to make one cohesive document.

to isolate the modulated ionic absorption signals from the unmodulated neutral signals, has allowed for the spectroscopic study of several cations and anions [93].However, due to harsh plasma conditions, molecular ions produced in VMS experiments often have high rotational and vibrational temperatures, typically on the order of several hundred Kelvin. For instance, CH_3^+ has been studied by the Oka group in a liquid nitrogen cooled discharge cell, where the rotational, vibrational, and translational temperatures were reported as 371, 700, and 830 Kelvin, respectively [49].

Until recently, all VMS experiments produced Doppler-limited line widths of $\gtrsim$1 GHz. [89] For small diatomic molecules, the spectra remain relatively simple to assign and line intensities are fairly strong, but larger molecular ions become much more complicated and lose intensity due to quantum dilution at increased rotational temperatures. Supersonic expansion discharges have also been used to study molecular ions, as they produce ions with reduced rotational temperatures through adiabatic expansion of a gas. This reduced rotational temperature comes with the price of lost ion/neutral discrimination, because the same discharge that produces the ions of interest also produces excited radicals and neutral molecules. Although concentration modulation can provide some discrimination from background precursors [21], radicals [3] and excited Rydberg states can still congest and complicate the recorded spectrum.

A fast ion beam spectrometer that provided rigorous ion/neutral discrimination and sub-Doppler line widths was developed in the late 1980s [17], with the hope of combining a supersonic expansion with the ion/neutral discrimination and narrow linewidths of a fast ion beam. In this instrument, ions were first produced in a plasma, then extracted from the discharge source, accelerated, and deflected 90° from the initial flight path, creating an ion beam that was spatially separated from any neutral molecules that were present in the source, and that was collinear with a laser beam. Within the laser-ion overlap region, the velocity of the ion beam was modulated using an AC voltage applied to a drift tube around the beams, providing rigorous ion-neutral discrimination when the detected signal from the laser was demodulated with a lock-in amplifier. A Wien filter (velocity filter) was used after the drift region to determine the species of the ion beam, but always at a much lower beam velocity than was typically used for spectroscopy. Absorption spectra in the mid-IR of HF^+, HN_2^+, HCO^+, H_3O^+ and NH_4^+ were recorded [17, 74, 50]. Supersonic discharges were attempted, but no rotational temperatures lower than 100 K were achieved. [51]

There have been a number of technological advances over the past 20 years that could allow for significant improvements over the previously developed ion beam spectrometer. Difference Frequency Generation (DFG) lasers are much more tunable than the previously used color center laser. Novel cavity enhanced spectroscopic techniques have been developed, more accurate and precise frequency measurements have been made possible with optical frequency combs, and ion optical components have been simplified and improved.

In this paper, we describe a new ion beam instrument that uses a Ti:Sapphire laser (the future pump of a DFG) for Noise Immune Cavity Enhanced Optical Heterodyne Molecular Spectroscopy (NICE-OHMS) as a sensitive spectroscopic probe of the ion beam. This instrument uses a time-of-flight mass spectrometer (TOFMS) to provide mass analysis of constituents of the ion beam at spectroscopically relevant beam energies. Lastly, a frequency comb is used to accurately measure the frequencies of the optical transitions.

The initial proof of concept system studied in this work is the fundamental band of the $A^2\Pi_u - X^2\Sigma_g^+$ system of N_2^+, which is an important species in atmospheric aurorae and electrical discharges. Because the line centers of many transitions in the fundamental band of this system are known [30], N_2^+ can serve as an easily understood benchmark of the capabilities of our fast ion beam spectrometer.

6.3 Experimental Approach & Performance

6.3.1 Overview of the experimental setup

The experimental setup can be divided into two functional groups: i) the ion beam setup, including the ion source, the ion optics and the mass spectrometer; and ii) the spectroscopic setup, consisting of the laser system and signal detection electronics. The two parts of the system interact in the central overlap region, where the laser cavity and the ion beam are superimposed. Figure 6.1 shows an overview of the entire experiment.

In order to minimize vibrations in the spectroscopic setup, the optical components are mounted on a pneumatically stabilized laser table that is mechanically isolated from the ion beam setup. The mirrors of an optical cavity are positioned on breadboards that overhang the edge of the laser table and surround the ion beam drift region. Within the optical cavity, the laser is coupled through Brewster windows mounted on the ion beam chamber, and is overlapped with the ion beam within the drift region.

A cold cathode ion source, described in detail in Section 6.3.2, is used to produce a beam of N_2^+ at an energy of 2-6 keV. After the beam is extracted from the source, it is focused by an Einzel lens and steered by two sets of parallel electrostatic plates into a cylindrical electrostatic double-focusing deflector [54]. When this deflector is biased, the ion beam is turned 90° and focused into the drift tube. When the deflector plates are grounded, the ion beam proceeds straight through a hole in the outer deflector plate and into a Faraday cup that is used to optimize source conditions for maximum ion current, which is generally $\sim$10 μA.

After exiting the deflector chamber, the ion beam proceeds through a 27 cm long drift tube and two metal plates that are spaced 13 cm apart, centered in the drift region. The metal plates are attached to vertical linear manipulators; each plate has three 3 mm diameter apertures that are spaced 1.5 cm vertically and

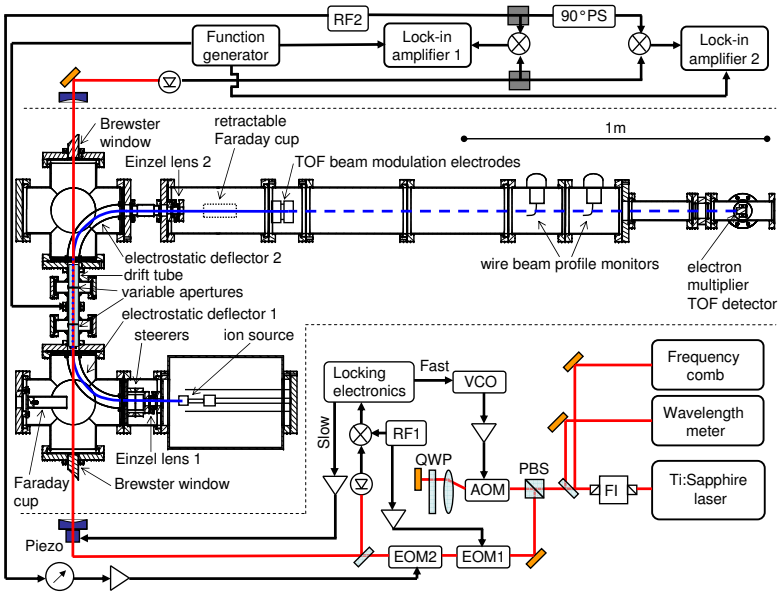

Figure 6.1: Complete schematic of the NICE-OHMS setup with fast ion beam.

1 mm horizontally. The apertures are aligned with the laser horizontally by choosing the hole that doesn't spoil the cavity finesse, and vertically within a hole by fine-tuning the vertical translation of the plates. After the appropriate apertures are centered on the laser, the ion beam is steered through the same apertures to make the laser and the ion beam collinear. The drift tube and the aperture plates are all electronically isolated from the surrounding chamber and connected to one another so they can all be used to modulate the velocity of the ion beam with an applied voltage.

After the drift region, the ion beam enters the second 90° bender which guides the ions out of the laser cavity into the time of flight mass spectrometer, which is described in detail in Section 6.3.4

Optical spectroscopy of the ion beam is done using the technique of noise immune cavity enhanced optical heterodyne molecular spectroscopy (NICE-OHMS) [114], which combines the long effective path length of cavity enhanced spectroscopy with the noise suppression of heterodyne spectroscopy. Further noise suppression is obtained my modulating the velocity of the ions by applying a square wave voltage to the drift tube. A more thorough description of the detection system is given in Section 6.3.5.

6.3.2 Cold Cathode Ion Source

A modular cold cathode discharge source was used for simplicity and low pumping throughput requirements. Our cold cathode source was made with a fused silica tube held by two electrodes, with an opening at the

back for sample gas inlet, and another at the front through which ions are extracted.

The electrodes are constructed using stock Ultra-Torr unions from Swagelok. High temperature silicone O-rings are used to make seals to the fused silica tube with polished ends. The front electrode includes a sustom ferrule with a 1 mm diameter aperture to allow ions to be extracted, and a 22° bevel to reduce beam expansion induced by space-charge interaction [70, 77]. A small circle of stainless steel mesh was used in the back electrode to produce a more uniform electric field while still allowing gas to flow through the inlet.

A schematic view of the source is shown in Figure 6.2. The aluminum cap that holds the back electrode provides mechanical stability and allows for electrical and water-cooling connections. The ions are extracted through a 0.25" diameter hole in a grounded stainless steel plate after the front electrode.

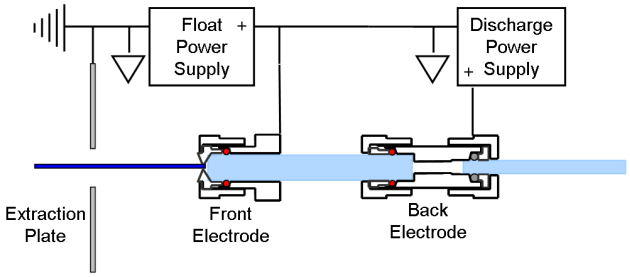

Figure 6.2: A schematic of the cold cathode with attached power supplies.

High voltage is applied to both electrodes. The front electrode is connected to the power supply that determines the beam energy. That power supply is also connected to the ground of the floating power supply, which is powered through an isolation transformer, and insulated by a plastic box.

6.3.3 Vacuum & Ion optical system

The vacuum system, with the exception of the ion source chamber, is made from standard stainless Conflat components in order to achieve high vacuum conditions. The homebuilt ion source chamber, which is pumped by a 2000 L/s turbomolecular pump, has a pressure of $\sim 5 \times 10^{-6}$ Torr during operation.

The overlap and mass spectrometry regions are pumped by two 500 L/s turbomolecular pumps situated below the 90° deflector chambers, establishing typical pressures during operation of 6×10^{-7} Torr at deflector 1 and 8×10^{-8} Torr at deflector 2. The vacuum cross that houses the mass spectrometer detector is pumped by a 250 L/s turbomolecular pump, and has a typical pressure of $\sim 2 \times 10^{-8}$ Torr.

The ion optical configuration was designed to optimize the ion density in the laser/ion overlap region between the two electrostatic deflectors. All ion optical elements are electrostatic, so all particles with the same kinetic energy and charge state are guided on the same trajectory regardless of particle mass. The

positive ions that emerge from the ion source with an energy V_{BEAM} are initially focused by the first Einzel lens. In the next short vacuum nipple the ion beam traverses a set of two parallel plate steerers. Each set of steerers can be used to deflect the ion beam both horizontally and vertically, allowing for an adjustment of the beam angle as well as for parallel offsets to the ion beam position. Each steerer plate is supplied by an independent bipolar power supply with voltages up to ± 1000 V. By applying voltages of the same sign to opposing steerer plates, it is also possible to induce additional horizontal or vertical focusing in the steerer section.

The cylindrical 90° deflectors follow a new design that provides control of the ion beam focusing in both dimensions [54], unlike traditional cylindrical or quadrupole deflectors that create an astigmatic output beam. Our cylindrical deflectors use plates of differing plate heights to mimic the field of a spherical deflector at the ideal ion beam orbit without the cost and size of a true spherical deflector.

In operation, about 50% of the 10 μA ion beam current that is measured in the Faraday cup in the first ion deflector chamber can be transported through the overlap region and both deflectors and collected in the retractable Faraday cup after deflector 2. But once the 3 mm apertures are put into place in the drift region, only 1-2 μA of beam current make it through the system. After traversing the overlap region, the ion beam is turned by the second deflector, collimated by a second Einzel lens, and directed into the time-of-flight mass spectrometer.

6.3.4 Beam-modulated TOFMS

MS Design

Previous ion beam spectroscopists used a Wein velocity filter as a mass analyzer to identify the ion species and to optimize the ion current at a lower beam energy than that at which the optical spectroscopy was performed, [74, 17, 50] mainly because of the limited resolving power of a Wien filter. A linear time-of-flight mass spectrometer (TOFMS), however, has the resolving power to characterize the ion beam simultaneously with the optical spectroscopy.

The linear TOFMS uses the well characterized beam modulation technique [6, 7] to create an ion packet from a continuous ion beam. Figure 6.1 shows the TOFMS region, consisting of an Einzel lens and a pair of vertical electrostatic deflector plates. The deflection plates are held at an equal voltage but with opposite polarity. The polarity of the plates is then quickly reversed to sweep the ion beam over a 5 mm diameter aperture located near the detector. Two beam profilers aid in aligning the ion beam through the 1.53 m drift tube and onto the electron multiplier tube detector.

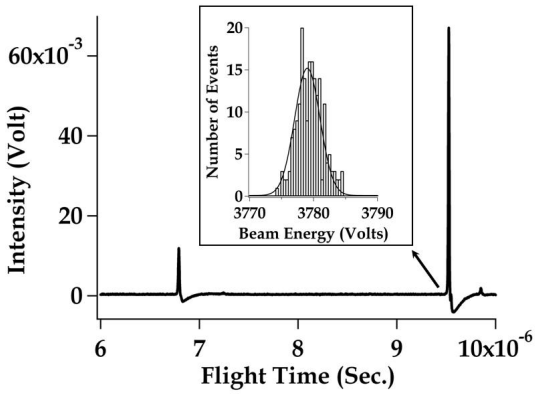

Figure 6.3: Mass spectrum take of N_2 plasma and the inset shows the energy spread

The mass spectrometer is used to (i) identify the ion species in the plasma, (ii) estimate the beam energy and (iii) calculate the energy spread of the ions created by the cooled cold cathode plasma source. In a nitrogen plasma under typical conditions, the source produces mostly N_2^+ and N^+ in a ratio of 10:1, as shown in Figure 6.3. The field-free flight tube length combined with arrival times of individual ions can be used to estimate both the average beam energy as well as the energy spread of the ions in the beam, as shown in Figure 6.3. For a beam energy of ∼3780 V, the energy spread was found to be 4.7 V, which is consistent with the spectroscopic linewidths presented in Section 6.4.1.

6.3.5 Optical Spectroscopy

The Ti:sapphire laser, optical cavity, and locking scheme, [89, 68] and the NICE-OHMS has been described previously [90] so only a brief overview is given here. Two sets of RF sidebands are added by two electro optic modulators (EOM). The first non-resonant EOM adds sidebands at ∼30 MHz with a small modulation index. The signal from a back reflection off of the cavity is demodulated with an RF mixer to generate the Pound-Drever-Hall [25] error signal. An analog lockbox splits corrections from the error signal into slow and fast components. The slow corrections are sent to the cavity piezo while the fast corrections are sent to the voltage controlled oscillator (VCO) that drives the AOM. As shown in Figure 6.1, the laser is double passed through a 85 MHz resonant acousto optic modulator (AOM), which makes the pointing of the laser beam immune to changes in the AOM frequency [24] and induces a 170 MHz redshift to the laser light.

The second EOM, resonant at 113 MHz, adds sidebands at exactly the FSR of the optical cavity with a

modulation index $\beta \sim 1$. The laser is coupled into the cavity, and the light transmitted through the cavity is detected with a fast photodiode.

Heterodyne spectroscopy (including NICE-OHMS) is sensitive to both absorption and dispersion signals, which are related to one another through the Kramers-Kronig relations. Since the two signals appear 90° out of phase with one another with respect to the RF modulation, it is possible to independently observe each signal with phase sensitive detection. To take advantage of this aspect of the spectroscopy, the AC component of the detector signal is amplified, split into two paths, and demodulated with two separate mixers which are set to be 90° out of phase with one another. The overall detection phase is adjusted using an RF phase shifter in the line between the RF generator and the amplifier that drives the 113 MHz EOM. The RF phase shifter is used to separate the absorption and dispersion signals from one another.

Modulation Scheme

Because residual amplitude modulation (RAM) induced by the EOM or external etalons can limit the sensitivity of NICE-OHMS, it is advantageous to use a second form of modulation. [33] In this work, the velocity of the ions is modulated by a square wave voltage at 4 kHz applied to the drift tube and aperture plates.

Because the ions travel at a high velocity, the observed lines are blue- and red-shifted according to

$$\frac{\nu'}{\nu_0} = \sqrt{\frac{1 \mp v/c}{1 \pm v/c}} \tag{6.1}$$

where ν' is the Doppler shifted frequency, ν_0 is the rest frequency, and v is the velocity of the ions, given by

$$v = \sqrt{\frac{2qV}{M}} \tag{6.2}$$

where q is the charge of an electron, V is the energy of the ion beam, and M is the mass of the species. For a 3.86 kV ion beam of N_2^+, the Doppler splitting is ~180 GHz. Under velocity modulation, the 5 V_{pp} square wave induces an additional doppler splitting of ~120 MHz.

Frequency Comb Calibration

The frequency of the laser can be determined at every point by measuring the beat frequency of the Ti:Sapphire laser against the nearest comb mode. [68, 90]. In order to characterize the precision of the spectroscopic measurements, several frequency comb calibrated scans are shown. **Insert graphs of comb calibrated scans.** After the line center for the red shifted ν_- and the blue shifted ν_+ components are

measured, the central line position can be calculated by taking the geometric mean $\nu_0 = \sqrt{\nu_- \nu_+}$.

6.4 Results

6.4.1 Spectroscopic Results

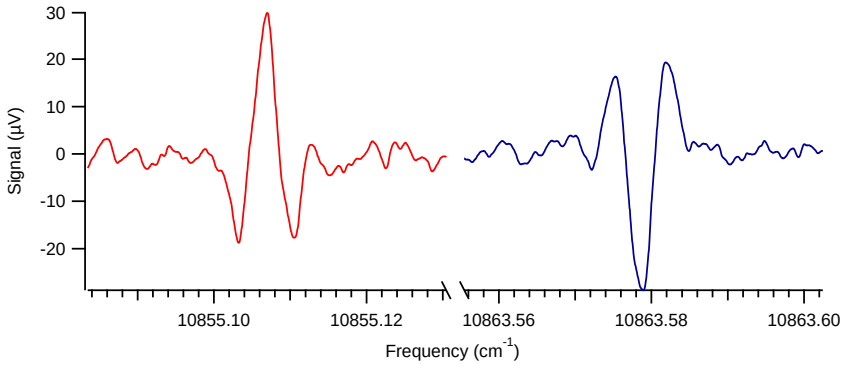

Figure 6.4: Scans of red- and blue-shifted components of the $Q_{22}(15)$ line. Note the two components are 180° out of phase with one another, allowing for identification of Doppler shift direction without observation of both components. Also note that the two components are separated by $\sim 8.5\,\mathrm{cm}^{-1}$.

Two typical scans of the $Q_{22}(15)$ line are shown in Figure 6.4. Only the dispersion phase is shown, because there is no observable signal at the absorption detection phase. Due of the large amount of laser power present within the laser cavity and the low ion density, we believe that the absorption signal is saturated to the point of being below the noise level of the instrument. The dispersion component, however, is unaffected by optical saturation. The line shape function for the NICE-OHMS velocity modulated dispersion signal the ion beam is given by

$$\begin{aligned} \chi^{disp}_{vm,D} =& \chi^{disp}(\nu_d - \nu_{fm} - \nu_{vm}) - 2\chi^{disp}(\nu_d - \nu_{vm}) + \chi^{disp}(\nu_d + \nu_{fm} - \nu_{vm}) \\ & - \chi^{disp}(\nu_d - \nu_{fm} + \nu_{vm}) + 2\chi^{disp}(\nu_d + \nu_{vm}) - \chi^{disp}(\nu_d + \nu_{fm} + \nu_{vm}) \end{aligned} \tag{6.3}$$

where χ^{disp} is the general dispersion line shape function, ν_d is the de-tuning of the carrier from the transition center frequency ($\nu_d = \nu - \nu_0$), ν_0 is the line center, ν_{fm} is the RF modulation frequency, and ν_{vm} is the velocity modulation spacing.

The Gaussian dispersion line shape, derived from a peak-normalized Gaussian line shape, is given by [34]

$$\chi^{disp}(\nu) = -\frac{2}{\sqrt{\pi}} e^{-\gamma^2} \int_0^{\gamma} e^{\gamma'^2} d\gamma' \tag{6.4}$$

where $\gamma = 2\nu_d\sqrt{\ln 2}/\text{FWHM}$ and FWHM is the full width at half maximum for the Gaussian profile.

When the spectra are fit to Equation 6.3, the line center, FWHM, and peak-normalized Gaussian amplitude are obtained. An example of the red- and blue-shifted components of a NICE-OHMS signal are shown in Figure 6.4. The average linewidth was ∼120 MHz, which is consistent with the beam energy spread observed with the TOFMS. Some slight asymmetry is seen between amplitude of the positive and negative velocity modulation components, and appears to be dependent on the alignment and overlap of the ion beam with the laser beam.

6.4.2 Sensitivity

For a baseline scan obtained with a 3 s lock-in time constant, the observed noise equivalent absorption is $\sim 1.3 \times 10^{-11}\,\text{cm}^{-1}$, which is a factor of 30 lower than the original ion beam instrument [17]. The improvement comes from several factors: a lower fractional noise level at the detector (5×10^{-8} vs 2×10^{-7}), thanks in part to heterodyne detection; a higher cavity finesse (450 vs 100); and a longer laser/ion overlap length (27 cm vs 15 cm). Unfortunately, our S/N is not improved by this same factor, mostly due to the fact that our ion density within the drift region is about an order of magnitude than that of the previous instrument.

The shot noise limit for the instrument is given by [113]

$$\sigma_{\text{shot noise}} = \frac{\pi}{F \times L}\sqrt{\frac{qB}{\eta P_0}}\frac{1}{J_0(\beta)J_1(\beta)} \tag{6.5}$$

where q is the charge of an electron, B is the bandwidth of detection, η is the detector responsivity, P_0 is the power incident on the detector, and $J_n(\beta)$ are Bessel functions of the heterodyne modulation index, β. The effective path length through the ion beam is the laser/ion beam interaction length (L=27 cm) times the number of round trip passes (F/π, where finesse∼450).

At a typical power level of 0.82 mW and a 3 s time constant, the expected fractional shot noise is $4 \times 10^{-12}\,\text{cm}^{-1}$. Thus, the observed noise in the instrument is within a factor of 4 of the shot noise limit. Because the noise level appears to be independent of laser power on the detector, it is believed that electronic noise limits the sensitivity of the instrument.

6.4.3 Discussion

In order to obtain a rotational temperature, spectra of the $^qQ_{22}$(J) lines (with J=4.5, 7.5, 10.5, 14.5 and 21.5) with lower energies ranging from 60 to 970 cm^{-1} were collected. The spectra were fit to Equation

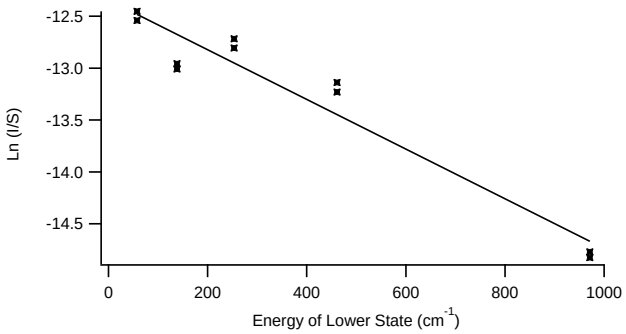

Figure 6.5: Boltzmann plot showing the temperature analysis.

6.3. The intensities were normalized to the strength of the transition, which was obtained along with the lower state energies, from PGopher [104] using constants from Reference [30]. Figure 6.5 shows a Boltzmann distribution plot for the five lines. From the slope of the linear regression, the rotational temperature is calculated to be 601±52 K.

While only a handful of lines were observed, there is no reason why more lines could not be observed with this more highly resolved technique. As the previous work [30] observed Doppler limited transitions with linewidths of 1-1.4 GHz, the line centers were only determined to a precision around 60 MHz, with an accuracy of 150 MHz. It is expected that the line center determination accuracy could be increased by at least a factor of 60. This is expected to have a positive effect on the overall RMS of the current fit (100 MHz) and the individual observed-calculated values for many blended lines. However, as N_2^+ has been studied extensively, other molecules may provide more scientifically interesting results.

Finally, it should be noted that the spectra shown have a completely rigorous ion/neutral discrimination both from the spatial separation and the applied velocity modulation. As the spectroscopy is only sensitive to the ions whose velocity is being modulated, the neutrals cannot contribute to the absorption signal. While previous cavity-enhanced velocity modulation technique studies [89, 68, 90] showed a discrimination between ions and neutrals in the detection phase, the ion beam technique is rigorously insensitive to absorbing neutrals.

6.5 Conclusions and Future Directions

We have demonstrated the construction of a fast ion beam spectrometer which provides the rigorous spatial and velocity modulation discrimination against background neutrals and radicals. We have demonstrated the instrument's capabilities by showing example spectra from the $A^2\Pi_u - X^2\Sigma_g^+$ system of N_2^+, and in so doing, have demonstrated the first direct absorption equivalent spectra of an electronic transition in an ion beam.

We have demonstrated that the ion beam produces sub-Doppler spectra with dispersion features equivalent to absorption features. The ion beam instrument has a mass spectrometer with high time-resolution that resolves mass spectra at spectroscopically relevant beam energies. The line shape of the NICE-OHMS signal has been described, as well as the sensitivity and the observed noise. With the current detectors and laser power, the noise is within a factor of 4 of the shot noise limit. The NICE-OHMS instrument reported in this article has been shown to be a factor of 30 more sensitive than previous direct absorption ion beam instruments [17]. The rotational temperature of ions in the ion beam was found to be $\sim$600 K.

The laser spectroscopy reported here was based on using two EOMs on a frequency tunable Ti:Sapphire laser. By combining the output the Ti:Sapphire with a Nd:YAG laser in a periodically-poled Lithium Niobate crystal, a mid-IR laser with sidebands NICE-OHMS will be produced. This will allow the extension of this NICE-OHMS technique into the mid-IR to record the fundamental vibrations of other molecular ions.

Finally, it is expected that a continuous supersonic expansion discharge source [18] and skimmer will replace the cold cathode ion source in the near future. Using a supersonic expansion will enable the spectroscopy of larger molecular ions, for which quantum dilution at high temperatures is a serious problem.

Chapter 7

Indirect Rotational Spectroscopy of HCO^+

7.1 Abstract

Spectroscopy of the ν_1 band of the astrophysically relevant ion HCO^+ is performed with an optical parametric oscillator calibrated with an optical frequency comb. The sub-MHz accuracy of this technique was confirmed by performing a combination differences analysis with the acquired rovibrational data and comparing the results to known ground-state rotational transitions. A similar combination differences analysis was performed from the same data set to calculate the previously unobserved rotational spectrum of the ν_1 vibrationally excited state with precision sufficient for astronomical detection. Initial results of cavity-enhanced sub-Doppler spectroscopy are also presented, and hold promise for further improving the accuracy and precision in the near future.

7.2 Introduction

Molecular ions are a particularly challenging group of species to study with optical spectroscopy. Even in laboratory plasmas that are designed to observe only a specific ion, neutral molecules are still orders of magnitude more abundant than their charged counterparts. This is why the most productive techniques for ion spectroscopy tend to have some method for discriminating ionic absorption signals from neutral ones. Since the late 1980s, the predominant tool for this has been velocity modulation spectroscopy (VMS). The groundwork of VMS was laid by Wing *et al.* in a velocity modulated ion beam [107], and the first application of VMS as it is known today was by Gudeman *et al.* in a velocity modulated positive column discharge cell. [41] Since the initial work, the technique has become a mainstay in ion spectroscopy and has been extensively reviewed. [93, 39]

Protonated carbon monoxide, HCO^+, was the first ion whose spectrum was acquired using VMS. The

This chapter was submitted for publication in the *Journal of Physical Chemistry A* as: B. M. Siller, J. N. Hodges, A. J. Perry, and B. J. McCall,"Indirect Rotational Spectroscopy of HCO^+"

R-branch of the ν_1 C-H stretch band was first measured by Gudeman *et al.* in a positive column discharge cell out to R(18). [41] Shortly after, the P-branch was also observed out to P(10) in a modulated DC glow. [2] After these lines were published it was another 24 years before any work revisited the ν_1 band, when Verbraak *et al.* used a continuous wave optical parametric oscillator (cw-OPO) operating in the mid-infrared and a supersonic expansion discharge source to rotationally cool the ions. [100]

The first observation of an HCO^+ rotational transition was via telescope rather than in a laboratory in 1970 by Buhl and Snyder. [15] Because the line that they observed was unidentified at the time, it was referred to as "X-ogen". Later that year, Klemperer suggested that the "X-ogen" line was due to the J = 1←0 transition of HCO^+. [53] Five years later, Woods *et al.* confirmed its identity by microwave spectroscopy. [109] Since that time, HCO^+ has been found in a variety of astronomical environments including protoplanetary nebulae [82], star forming regions [79], the interstellar medium [61], and even the comet Hale-Bopp [67]. The abundance of HCO^+ makes it an important participant in the rich chemistry that exists in the interstellar medium. Due to the large rotational constant of HCO^+, its higher rotational transitions exist in the sub-millimeter/terahertz region. Newer telescopes such as The Atacama Large Millimeter and sub-millimeter Array (ALMA) and the Stratospheric Observatory For Infrared Astronomy (SOFIA) have sub-millimeter/terahertz capability. These new astronomical capabilities lend necessity to a relatively simple way to gain laboratory information in that spectral region, a challenging region for laboratory spectroscopy, due in part to the relative scarcity of quality sources and detectors compared to the microwave and infrared spectral regions. In this work, we present a demonstration of how precision rovibrational spectroscopy can be used to infer rotational transitions to precision sufficient to facilitate astronomical searches.

In the case of HCO^+, most of the ground state transitions have been observed up to J = 17←16, with the exception of a few gaps in coverage. [16] Additionally, only a few pure rotational lines have been observed in vibrationally excited states. One such transition is the J = 3←2 rotational transition in the ν_1 first vibrationally excited state. [56] With this single transition combined with our high-precision IR spectrum, the entire rotational spectrum of the ν_1 state can be calculated, limited only by the number of rovibrational lines that have been observed. The technique demonstrated here is also useful for determining high precision rotational constants in excited states.

In this work, we present spectra of the ν_1 fundamental band of HCO^+ acquired using optical heterodyne spectroscopy coupled with VMS (OH-VMS). This technique combines the advantages of the low noise of heterodyne spectroscopy with ion-neutral discrimination of VMS. Our instrument utilizes a cw-OPO tunable from 3.2 to 3.9 μm, and produces ions within a liquid nitrogen cooled positive column discharge cell. Optical

frequency comb calibrated scans were acquired and fit with sub-MHz precision, and the resulting fits were used to calculate rotational transitions for the ground state and the first vibrationally excited C-H stretch state. These calculations result in the first experimental observation, albeit indirectly, of the J = 3←2 transition in the ground state and the complete determination of the of the rotational spectrum up to J = 10←9 in the ν_1 first excited state.

7.3 Experimental

The experimental setup, shown in 7.1, has been described previously [19] with the exception of the frequency comb integration, so it will be discussed only briefly here. A Ytterbium-doped fiber laser is frequency modulated with a fiber-coupled electro optic modulator (EOM) using two RF generators: one at ∼80 MHz for heterodyne detection, and the other at ∼2 MHz for locking to the optical cavity around the discharge cell. After the modulation is applied, this seed laser is amplified to 10 W total power using a fiber amplifier, and this amplified beam acts as the pump for the optical parametric oscillator (OPO).

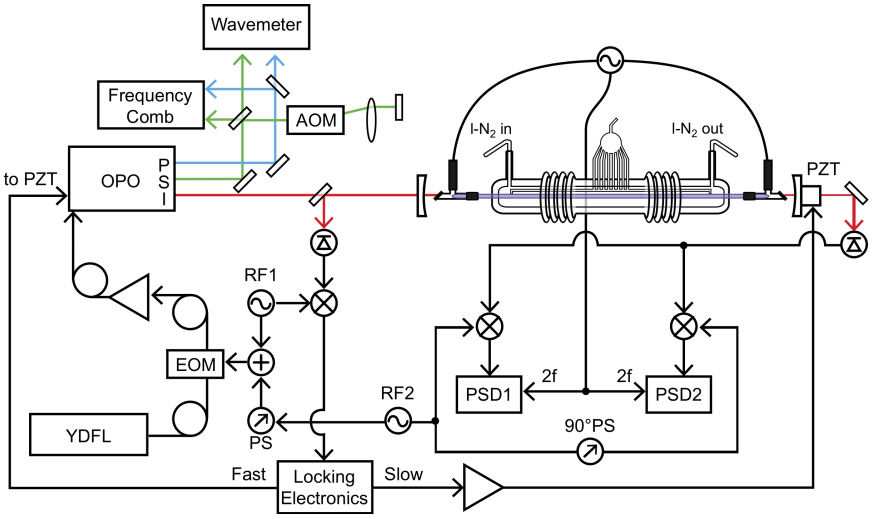

Figure 7.1: The Experimental Layout. YDFL: Ytterbium-doped fiber laser; EOM: electro-optic modulator; PS: phase shifter; RF: radio frequency generator; OPO: optical parametric oscillator; P: pump; S: signal; I: idler; PZT: piezo-electric transducer; PSD: phase-sensitive detector

Three beams exit the OPO head: the pump (∼1064 nm), the signal (tunable from 1.5 to 1.6 μm), and the idler (tunable from 3.2 to 3.9 μm). The idler is used for spectroscopy of HCO^+ while the other beams are used for frequency measurements using a near-infrared wavemeter and frequency comb. For the comb-calibrated scans, the wavemeter is only used prior to a scan to determine which comb modes the pump and signal are each closest to, while the comb is used throughout the scan to take frequency readings at each

acquired data point.

7.3.1 Comb Integration

The optical frequency comb used in this work (Menlo FC1500) has been described previously in operation with a different laser system. [68] Scanning the OPO with the comb is accomplished by first tuning the carrier-envelope offset of the comb to approximately 20 MHz and determining its sign. Then the comb repetition rate is tuned to make the signal offset beat lie within the range of 25-35 MHz from the nearest comb mode, limited by the RF bandpass filter built into the frequency counter used to record that beat. Then the frequency of the pump is tuned to approximately 20 MHz from its nearest comb mode, and the signs of the offset beats for both the pump and the signal are determined and recorded. Finally, the pump is offset-locked to the comb using a frequency-to-voltage converter circuit that generates an appropriate error signal for offset locking.

The nearest comb mode numbers are determined for the pump and the signal before each scan using the wavemeter, then are recorded (and incremented/decremented for the signal when necessary) as the scan progresses. At each frequency step, the data acquisition program pauses for 1.5 seconds, then the comb repetition rate and offset beats are recorded by frequency counters with 1 Hz refresh rates, and the lock-in amplifier outputs are recorded. With the lock-in amplifier time constant set to 300 ms, the lock-in amplifiers have 5 time constants to respond before the reading is polled for each point, so any scanning direction dependent line center pulling is smaller than the random scan-to-scan variability in line center determination.

After each point, the repetition rate is tuned by an amount sufficient to slew the pump frequency by $\sim$5 MHz ($\sim$1.8 Hz change in repetition rate). The pump remains offset locked to the same comb mode throughout the course of each scan. The total continuous scanning range of the pump (and therefore for the idler) for comb-calibrated scans is limited to $\sim$800 MHz by the comb scanning electronics; the comb repetition rate can only be changed by a relatively small amount while still retaining its lock onto the direct digital synthesizer (DDS) that stabilizes the repetition rate.

To keep the signal offset within the frequency counter bandpass filter at each point, a feed-forward system is used to tune the signal frequency using a double-pass acousto-optic modulator (AOM) setup. In a double-pass configuration, the frequency shift induced by the AOM is doubled, while making the pointing of the beam independent of the frequency applied to the AOM. [24] Stable pointing is crucial to the operation of the system, as good spatial overlap between the comb light and each of the cw beams is important for generating offset beat signals on the high speed detectors.

After the counters are read for a data point and the repetition rate is slewed to the next point, the amount the signal frequency needs to be shifted by is calculated using the change in the repetition rate, the signal comb mode number, and the amount the signal was away from the 30 MHz target offset frequency for the previous point; this frequency shift is then applied to the frequency of the RF generator that drives the AOM. The AOM diffraction efficiency is high enough to provide reliable signal/comb offset beat measurements in the driving frequency range of 150-210 MHz, which corresponds to a frequency shift of 300-420 MHz when taking into account the double-pass configuration. When the calculated desired AOM frequency lies outside this range, the drive frequency is shifted by 50 MHz (corresponding to a 100 MHz change in the shifted signal frequency, matching the comb repetition rate), and the signal mode number is incremented or decremented by one, depending on whether the 100 MHz shift was positive or negative.

This signal-shifting scheme allows the shifted signal frequency to be determined using the frequency comb at each point, despite the fact the signal frequency is fixed (with the exception of some slow drift) while the comb repetition rate is slewing. The unshifted signal frequency can then be determined simply by subtracting the AOM frequency shift, which is precisely known from the digital setting of the RF generator at each point, and this unshifted signal frequency is subtracted from the directly measured pump frequency to determine the idler frequency.

7.3.2 Spectroscopy Configuration

The plasma cell used in this work, Black Widow, shown in 7.2, was the same cell used by Takeshi Oka in many of his velocity modulation experiments. It allows for liquid nitrogen cooling of the plasma to reach an estimated rotational temperature of ∼166 K for HCO^+, as shown in the Boltzmann plot in 7.3, using plasma conditions of 30 mTorr CO in 500 mTorr H_2 with a 35 kHz, 140 mA discharge. The idler beam is coupled through Brewster windows on either end of the cell into the central bore of the discharge cell. For this work, three different optical configurations were used: single-pass, double-pass and cavity-enhanced, all of which relied on heterodyne modulation and detection at ∼80 MHz.

The comb calibrated scans presented in this paper used a simple single-pass configuration, where the cavity mirrors shown in 7.1 were removed and the cavity-locking RF modulation and feedback circuit were disabled. This allowed for the acquisition of Doppler-broadened scans with signal-to-noise ratios of ∼300 for the strongest lines and ∼100 for the weakest ones, but due to the lack of a bidirectional beam and sufficient laser power, did not allow for the observation of Lamb dips. A typical comb-calibrated scan is shown in 7.4.

A series of double-pass wavemeter-calibrated scans were collected for the previously unobserved P(11) through P(17) transitions. In the double-pass configuration, a single mirror was placed on the far side of

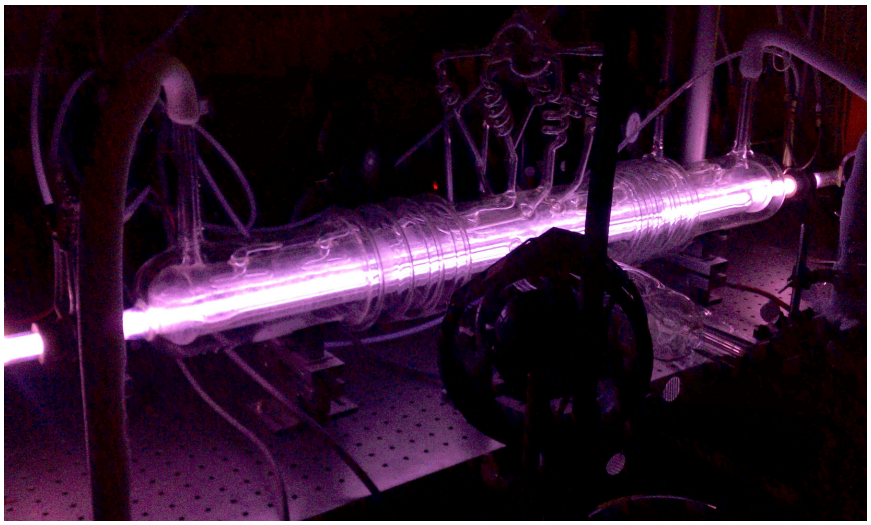

Figure 7.2: "Black Widow", the liquid nitrogen cooled positive column discharge cell acquired from Takeshi Oka and used for the work in this paper. The central bore, where the plasma discharge occurs, is surrounded by a sheath of flowing liquid nitrogen, which is in turn surrounded by a vacuum jacket to prevent ice from forming on the cell.

the cell to back-reflect the idler for a second pass through the cell. Approximately 30% of the reflected beam was then picked off with a silicon window and directed to a high-speed detector, the signal from which was demodulated first at the heterodyne frequency, then at twice the plasma frequency ($2f$), as opposed to the $1f$ demodulation that was used for the single-pass work. The linecenters determined from these scans are shown in 7.1, and compared to the calculated values from the fit parameters determined by the comb-calibrated work. All but one of the linecenters determined from these scans fall within the expected 70 MHz uncertainty from the wavemeter calibration. The one exception, P(17), is thought to be off by more than the uncertainty due to an inaccurate signal reading caused by poor optical alignment.

Transition	Observed (cm^{-1})	Calculated (cm^{-1})	Obs - Calc (MHz)
P(11)	3054.730	3054.73019(4)	-6
P(12)	3051.502	3051.49993(5)	62
P(13)	3048.245	3048.24688(6)	-57
P(14)	3044.969	3044.97111(7)	-63
P(15)	3041.672	3041.67269(8)	-21
P(16)	3038.354	3038.35169(9)	69
P(17)	3035.013	3035.00817(10)	145

Table 7.1: Previously unobserved wavemeter-calibrated scans of the P(11) through P(17) transitions. Uncertainties are ∼70 MHz, limited by the wavemeter uncertainties for the pump and signal frequencies added in quadrature. Calculations are based on ground state constants from Cazzoli *et al.*[16] and excited state constants determined from our comb-calibrated scans.

A few uncalibrated scans were collected with the cavity mirrors in place in a noise immune cavity enhanced

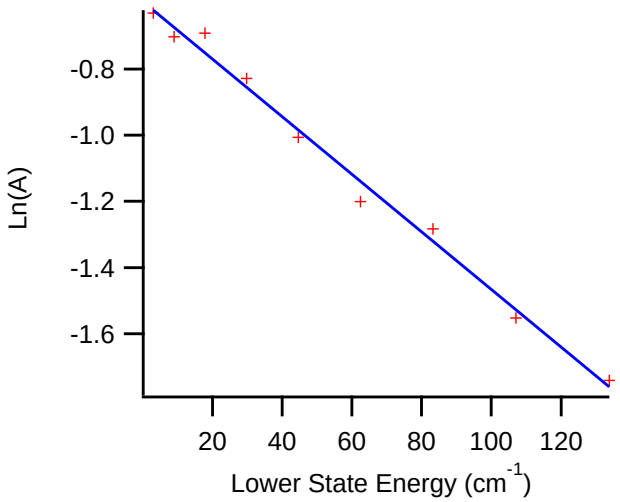

Figure 7.3: Boltzmann plot for R(1) through R(9), with the slope indicating a plasma temperature of ∼166 K. The vertical axis is the natural log of the line strength normalized peak-to-peak amplitude of a double-pass scan for each transition.

optical heterodyne velocity modulation spectroscopy (NICE-OHVMS)[90] configuration. One such scan, showing strong central Lamb dip features on top of the Doppler profile, is shown in 7.5. Unfortunately, the dielectric coatings on the mirrors were found to be hygroscopic, which led to poor laser coupling efficiency through the cavity in this wavelength range and degraded performance over time. To obtain optimal Lamb dip depth, the total cell pressure had to be decreased to ∼200 mTorr and the discharge current had to be turned down as low as possible while still maintaining a stable plasma, to ∼100 mA. Both the lower pressure and the lower discharge current produce lower overall density of HCO^+ within the cell. This decreased density combined with the poor laser transmission through the cavity cause the signal-to-noise in the NICE-OHMS scans to be significantly compromised compared to the single- and double-pass scans, despite the factor of ∼400 greater path length that NICE-OHMS provides through the plasma.

7.4 Results and Discussion

Each comb calibrated scan was fit to a second derivative of a Gaussian function, which approximates the convolution of heterodyne modulation with velocity modulation observed in the experiment. Between 4 and 7 scans were acquired of each transition, and the data acquired from those fits were used to compute the average linecenters and standard errors shown in 7.2. The errors varied somewhat from one transition to the next, but the average uncertainty was found to be ∼600 kHz.

As can be seen by the fit in 7.4, this fit function is not perfect, likely due to imperfect setting of the

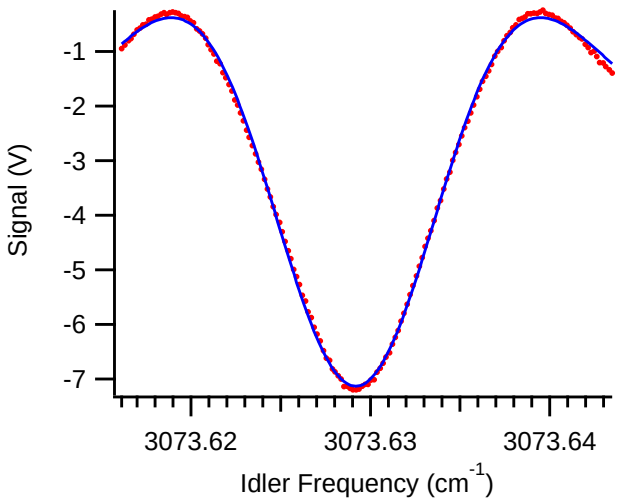

Figure 7.4: A typical comb-calibrated scan (red dots) of the P(5) transition of HCO^+, along with a fit to the data (blue line). Error bars for the points are not shown, as they would be smaller than the point size for both intensity and frequency.

detection phases. For this work, both the RF and plasma demodulation phases were set to maximize the signal-to-noise of a single detection channel out of the four channels that were acquired with each scan. It is likely that there is some dispersive component to the lineshape function, rather than it being purely absorptive. It is also likely that the velocity modulation of the ions is not purely sinusoidal and that the lock-in demodulation is not exactly in phase with the velocity modulation, and both of these factors can also affect the overall lineshape.

There is also a slight asymmetry in the observed lineshapes for several of the scans that is not fully understood at this time. By adding a slightly sloped baseline to the data, we can make it significantly more symmetric, and also make the fit slightly better. Symmetrizing the data in this way causes the determined linecenter to shift by less than 1 MHz for even the most asymmetric scans. Given that we do not know the physical cause of this phenomenon, we have taken the approach of manipulating the data as little as possible, so this symmetrizing was only done to estimate the potential error induced by the asymmetry. When asymmetry is present, it tends to manifest with the low-frequency lobe of the lineshape having a greater maximum than the high-frequency one. Such a systematic error would be mitigated by subtraction of observed linecenters, as is done in the combination differences analysis described in the following several paragraphs. Based on the errors in the calculation of rotational transitions, it appears that random scan-to-scan variability is the limiting factor in linecenter determination, and not the effects of this asymmetry.

For approximately half of the comb-calibrated scans, the determined linecenters disagreed with the previously measured HCO^+ transition frequencies [2] by greater than the specified accuracy of 30 MHz.

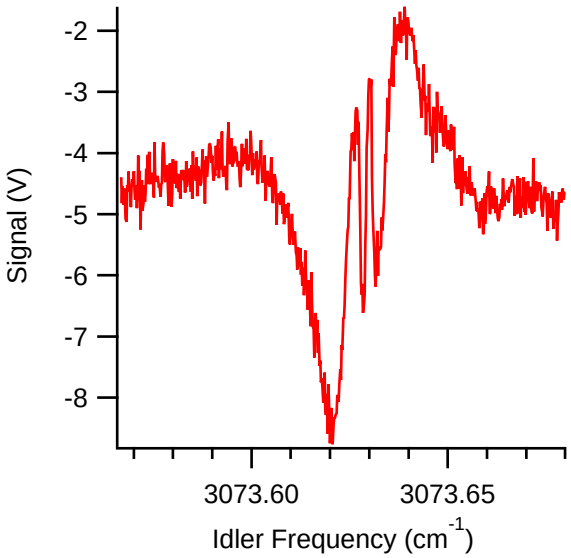

Figure 7.5: A roughly calibrated scan of the P(5) transition of HCO^+, showing the Lamb dips that are obtainable with cavity enhancement combined with lower cell pressure. The frequency calibration of this scan was based on the line center determined from the comb calibrated scans combined with the approximate scan voltage to frequency transfer function of the seed laser.

It was found that the source of the errors was incorrect comb mode number determination for either the signal or the pump beams due to inaccuracy of the wavemeter. These incorrectly calibrated scans were easily corrected by adding or subtracting a multiple of the comb repetition rate to or from the calculated idler frequency. After correcting the idler frequency calibration, it was found that all but two of the the observed transitions agreed with Amano's previous work to within 30 MHz. The two exceptions to the 30 MHz agreement were the R(0) and R(3) transitions, but those were both further verified by comparing the combination difference analysis with directly measured rotation transitions, as shown in 7.3. Any remaining error in the determination of comb mode numbers would appear as an error of ∼100 MHz, which is not observed.

A combination differences analysis was performed to demonstrate the accuracy of our comb-calibrated rovibrational compared to known rotational transitions. First, frequencies of transitions sharing the same upper state energy level, e.g. R(0) and P(2), were subtracted from one another to generate ground state energy level spacings for pairs of energy levels separated by two rotational energy levels. For example, the J=2←0 spacing was calculated from $f_{R(0)} - f_{P(2)}$, the J=3←1 spacing was calculated from $f_{R(1)} - f_{P(3)}$, and so forth for all observed transitions up to the J=10←8 spacing.

Then the directly measured J=1←0 transition was subtracted from the J=2←0 energy level spacing to indirectly compute the J=2←1 rotational transition frequency. This computed frequency was then subtracted

Line	Center (cm^{-1})	Previous [2] (cm^{-1})	Prev-Cur (MHz)
R(0)	3091.690432(16)	3091.6919(10)	44
R(1)	3094.618099(27)	3094.6181(10)	0
R(2)	3097.522054(07)	3097.5223(10)	7
R(3)	3100.402249(25)	3100.4034(10)	35
R(4)	3103.258604(21)	3103.2586(10)	0
R(5)	3106.090956(19)	3106.0909(10)	-2
R(6)	3108.899376(20)	3108.9002(10)	25
R(7)	3111.683680(04)	3111.6841(10)	13
R(8)	3114.443835(05)	3114.4445(10)	20
R(9)	3117.179881(41)	3117.1800(10)	4
P(1)	3085.763903(23)	3085.7646(10)	21
P(2)	3082.765487(53)	3082.7662(10)	21
P(3)	3079.743422(15)	3079.7437(10)	8
P(4)	3076.698005(05)	3076.6977(10)	-9
P(5)	3073.629188(16)	3073.6291(10)	-3
P(6)	3070.537136(19)	3070.5377(10)	17
P(7)	3067.421924(37)	3067.4224(10)	14
P(8)	3064.283464(10)	3064.2834(10)	-2
P(9)	3061.122045(18)	3061.1226(10)	17
P(10)	3057.937606(08)	3057.9380(10)	12

Table 7.2: A list of the comb-calibrated HCO^+ transition center frequencies (with associated uncertainties) observed in the current work, compared with previous measurements.

from the J=3←1 spacing to compute the J=3←2 transition frequency, and the process was repeated for higher rotational energy levels up to J=10←9. At each step, the calculated rotational transition from the previous step was used with a new energy level difference to compute a new rotational transition. The indirectly calculated rotational transitions in the current work are compared to the previously observed rotational transition frequencies in 7.3.

Such an analysis was also carried out for the ν_1 (C-H stretch mode) first vibrationally excited state. To our knowledge, the only directly observed rotational transition was J=3←2 [56]. This single transition, combined with our rovibrational data, is sufficient to compute the expected rotational transitions from J=1←0 up to J=10←9, as shown in 7.4. The comb-calibrated data were also fit using the previously determined ground state constants[16], and the following vibrationally excited state constants were determined: ν_1 = 3088.739009(5) cm^{-1}, B_1 = 44240.536(9) MHz, and D_1 = 82.31(9) kHz. These values agree within 2σ with the uncertainties those previously determined by Amano [3088.73951(31) cm^{-1}, 44240.34(33) MHz, and 80.3(33) kHz] using infrared spectroscopy [2], while disagreeing by 5σ with the B_1 and D_1 determined by an "all-inclusive" fit by Lattanzi *et al.* that used data from several microwave and infrared papers to determine constants across several vibrational states to determine B_1 = 44240.614(17) MHz and D_1 = 86.56(82) kHz. [56] Given that the only data for the ν_1 state included in the "all-inclusive" fit were Amano's

J'	J"	Calc. Freq. (MHz)	Obs. Freq.[16] (MHz)	Calc - Obs (MHz)
0	1	n/a	89188.5247	n/a
1	2	178374.6(17)	178375.0563	-0.5
2	3	267557.0(19)	n/a	n/a
3	4	356732.3(19)	356734.2230	-2.0
4	5	445903.9(21)	445902.8721	1.0
5	6	535061.0(23)	535061.5810	-0.5
6	7	624207.4(26)	624208.3606	-1.0
7	8	713344.0(27)	713341.2278	2.8
8	9	802455.7(27)	802458.1995	-2.5
9	10	891558.4(27)	891557.2903	1.1

Table 7.3: Indirectly calculated rotational transition frequencies derived from the data in 7.2 compared to the directly measured rotational transitions compiled by Cazzoli *et al.* [16].

infrared spectrum (which reported transitions with 30 MHz uncertainties) and a single rotational transition (J=3←2) [46], we do not currently understand the small magnitude of uncertainties reported by Lattanzi *et al.*

J'	J"	Calc. Freq. (MHz)	Uncertainty (MHz)
0	1	88486.7	1.9
1	2	176955.4	1.6
2	3	n/a	n/a
3	4	353900.7	0.9
4	5	442366.0	1.1
5	6	530813.3	1.3
6	7	619257.7	1.6
7	8	707676.3	1.9
8	9	796093.7	1.9
9	10	884477.9	2.4

Table 7.4: Pure rotational transitions for the vibrationally excited ν_1 state of HCO^+, calculated from the rovibrational data in 7.2 and the directly observed[56] J=3←2 rotational transition.

7.5 Conclusions

The current work demonstrates the ability of Doppler-broadened comb calibrated velocity modulation spectroscopy to determine linecenters with sub-MHz accuracy and precision. This accuracy has been verified by performing a combination differences analysis of the rovibrational data and comparing the results to the previously observed rotational spectrum of vibrational ground state HCO^+. The potential of extending the technique to sub-Doppler work has also been demonstrated. With a proper set of cavity mirrors, it should be possible to further improve the precision of this technique. From the current series of fits, the Doppler-limited linewidth is ∼450 MHz, and the uncertainty of a single fit is ∼350 kHz. From the Lamb dip scan of

HCO^+ shown in 7.5, the peak-to-peak linewidth of the central sub-Doppler feature is only ∼50 MHz, so it is reasonable to assume that the precision of a fit to sub-Doppler features would be approximately an order of magnitude more precise than one to a Doppler-broadened scan, assuming the S/N problem can be solved by a non-hygroscopic set of cavity mirrors. The investigation into whether the accuracy is also improved by the same factor will be the subject of future work.

One of the greatest advantages of this indirect approach over direct rotational spectroscopy is the generality of it. The chemistry within positive column discharge cells tends to be very rich, so it is possible to make a wide variety of molecular ions. The cell used in the current work was cooled with liquid nitrogen, but it could easily be cooled by water or air, or even heated to attain greater population in higher rotational levels and compute the rotational spectrum up to very high J values. The infrared source and detectors are also very versatile in terms of spectral coverage; entire rovibrational bands for a wide variety of ions lie within its tuning range, and can be observed without any changes to the optoelectronic system.

This work also has implications for astronomical searches for the astrophysically relevant ion HCO^+. While the ground vibrational state has been thoroughly studied, little work has previously been done in this vibrationally excited state. Rotational transitions in the vibrationally excited state could be of astrophysical interest, particularly in hot, dense environments such as hot cores and circumstellar envelopes. [12]

7.6 Acknowledgments

The authors would like to acknowledge an NSF grant (CHE 12-13811) and a NASA Laboratory Astrophysics grant for funding. BJM wishes to acknowledge support from a David & Lucile Packard Fellowship and a Camille Dreyfus Teacher-Scholar award. BMS would like to thank a NASA Earth and Space Science Fellowship (NESSF NNX11AO06H), and JNH is grateful for support by a Robert & Carolyn Springborn fellowship and an NSF Graduate Research Fellowship (DGE 11-44245 FLLW). The authors would also like to thank Takeshi Oka for supplying the discharge cell and associated electronics and pumps used for this work.

Appendix A

Precision Cavity Enhanced Velocity Modulation Spectroscopy

A.1 Abstract

The new technique of cavity enhanced velocity modulation spectroscopy has been further developed, incorporating a tighter cavity to laser lock and an optical frequency comb for absolute frequency calibration. Several N_2^+ transitions have been observed with much higher precision than previously possible, and transitions that were blended in earlier Doppler-limited experiments are now resolved. The full-width at half-maximum of the observed Lamb dips is ∼40 MHz, and appears to be dominated by a broadening due to the velocity modulation. Future extension of this technique into the mid-infrared should enable significant improvements in the sensitivity and resolution of vibrational spectroscopy of molecular ions.

A.2 Introduction

Ever since its development by Gudeman et al. in 1983 [41], velocity modulation spectroscopy has been the workhorse of molecular ion spectroscopy, because of its sensitive discrimination between ion and neutral signals. [39] In the past 25 years, this technique has been used to study nearly fifty different molecular ions, as reviewed in [93]. It has been implemented at wavelengths ranging from the UV to the millimeter-wave. [28, 84] The most sensitive velocity modulation spectrometers (e.g., [38, 71]) combine optical heterodyne modulation with a modified White cell for uni-directional multipassing. The S/N ratio of such experiments could be further improved by extending the optical path length using an external cavity, but the traditional $1f$ demodulated signal vanishes in such a cavity.

No major technological advances have been published on velocity modulation since it was last reviewed in [93]. However, additional molecular ions have been studied, including $FeCO^+$ [42] and FeO^+ [43] in

This chapter was first published as: A. A. Mills, B. M. Siller, and B. J. McCall,"Precision Cavity Enhanced Velocity Modulation Spectroscopy", *Chemical Physics Letters*, **501**, 1-5 (2010).[68]

the millimeter/submillimeter range, and D_2O^+ [26], SO^+ [57], and H_3O^+ [116] in the mid-infrared. Other molecules such as Cl_2^+ [110], CO^+ [112], and N_2^+ [111] have been studied in the visible/near-IR using the optical heterodyne magnetic rotation enhanced velocity modulation previously reviewed in [93].

In a recent paper [89], we demonstrated that ion-neutral discrimination can be achieved in an optical cavity, using phase-sensitive $2f$ detection. This work also showed that Lamb dips were observable due to the high intracavity power, thus opening the door to routine sub-Doppler spectroscopy of molecular ions. However, those experiments were limited by a poor laser to cavity lock and a lack of precise frequency calibration. Here, we present an improved system that uses a double-passed acousto-optic modulator (AOM) to achieve a tight lock of the cavity to the laser, and an optical frequency comb to obtain precise frequency calibration.

We demonstrate the method using the well-studied N_2^+ ion, which is abundant in atmospheric aurorae and nitrogen discharges [30]. The $A^2\Pi_u$-$X^2\Sigma_g^+$ system has been studied extensively. Several bands were observed in auroral storms by Meinel in 1950 [66], and the the 1-0 band was recorded in the laboratory by Benesh et al. in 1979 with a resolution of 1800 MHz [9]. Ferguson et al. recorded the Doppler-limited spectrum of several bands including the 1-0 band with a measurement precision of 60 MHz and an accuracy of 150 MHz [30]. These studies all relied on unmodulated sources, either DC positive column discharges or hollow cathodes. Other workers investigated higher vibrational levels by using velocity modulation [80, 20, 58].

Several groups [65, 94, 87, 64, 14, 95, e.g.] have used optical frequency combs to measure the absolute transition frequencies of molecular neutrals, in many cases combining them with sub-Doppler techniques to achieve a precision as good as ∼10 kHz. However, to our knowledge, the present work represents the first application of optical frequency combs to high-precision molecular ion spectroscopy.

A.3 Experimental Setup

The experimental setup is an improved version of the one described in [89], and is illustrated in Figure A.1. Molecular ions (N_2^+) were produced in an uncooled positive column discharge cell with a continuous flow of nitrogen at ∼0.5-4 Torr, as measured by a thermocouple gauge that was calibrated to a capacitance manometer. The ions were probed by the output of a Ti:Sapphire laser which was injected into an external cavity containing the discharge cell. An electro-optic modulator (EOM) added sidebands at 14 MHz, and the back-reflection off the cavity was used to generate a Pound-Drever-Hall error signal that represents the difference between the laser frequency and the cavity modes [25].

The low-frequency portion ($\lesssim$ 100 Hz) of this error signal was fed back to a piezo on the cavity, which

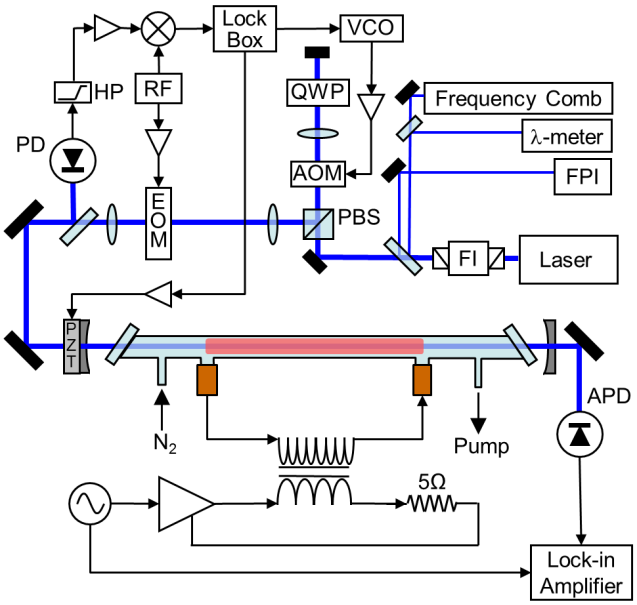

Figure A.1: Experimental layout, color online. Faraday isolator (FI), Fabry-Perot interferometer (FPI), acousto-optic modulator (AOM), polarizing beamsplitter (PBS), quarter-wave plate (QWP), radiofrequency generator (RF), electro-optic modulator (EOM), photodiode (PD), voltage controlled oscillator (VCO), avalanche photodiode (APD), high-pass filter (HP).

essentially locks the cavity to the laser; the laser itself is stabilized to an internal reference cavity which is temperature and pressure stabilized. The high-frequency portion of the error signal was fed to a voltage-controlled oscillator (VCO), which feeds a double-passed acousto-optic modulator (AOM; central frequency of 85 MHz) in a scheme similar to [24]. The frequency-shifted laser light was thereby locked to any fast fluctuations of the external cavity. This introduced a jitter of 1-2 MHz (as measured by fluctuations in the voltage input of the VCO while the system is locked), which is considerably smaller than the width of all of our observed transitions. The improved lock, compared to that in reference [89], enabled us to remove the intracavity iris which had been used to lower the finesse to ∼100, resulting in a higher finesse of ∼250 in the present experiment.

Before passing through the AOM (which blue-shifts the laser by 170 MHz), a portion of the laser beam was picked off and sent into a wavemeter (Bristol 621A-IR) with an accuracy of ±0.2 ppm (∼ ±65 MHz), which was used for rough calibration. Another portion was combined on a photodetector with an optical frequency comb (MenloSystems FC1500), and the beat note was counted with the comb electronics. The FC1500 is a fiber-based comb, which contains two locking systems to keep the repetition frequency (f_{rep}) and the carrier-envelope offset (f_{ceo}) stabilized. In our case, f_{rep} was locked near 100.005 MHz, and f_{ceo} was locked to ∼20 MHz. These frequencies are based on an input from a high-stability oven-controlled

crystal oscillator that is disciplined to the Global Positioning System (Endrun Technologies Tycho, HS-OCXO). Since the oscillator control loop averaging time constant is over 500,000 seconds, the stability of the oscillator's 10 MHz frequency reference is expected to be better than 1×10^{-12}. The output of the fiber comb is frequency doubled in a periodically poled lithium niobate crystal, and spectrally broadened with a photonic crystal fiber. Because the comb light passes through a sum-harmonic generation periodically poled lithium niobate crystal, f_{ceo} becomes $2f_{ceo}$.

The output of the cavity was directed onto a photodiode, the signal from which was demodulated by a lock-in amplifier referenced to twice the plasma frequency (with the phase set to be optimally sensitive to ion signals). The output of the lock-in was recorded, along with calibration data, by a custom LabView program over the course of each scan.

Scanning was performed in two different modes, which we refer to as high resolution and ultra-high resolution. In the high resolution scans, the laser was stepped in 5 MHz steps, with a 300 ms time constant and a 300 ms delay between points, and calibration was performed using only the wavemeter. In the ultra-high resolution scans, the laser was stepped in 1 MHz steps, with a 1 second time constant and delay time, and was calibrated using the frequency comb. For this purpose, the data acquisition computer recorded f_{rep}, $|f_{ceo}|$, and $|f_{beat}|$ from the comb's computer, for each frequency step in our scans. Because the measurement system for $|f_{beat}|$ has a bandwidth of only 19.5-25.5 MHz, it was necessary to ratchet f_{rep} by 1.2 Hz whenever $|f_{beat}|$ approached its limit in the course of a scan. This ensured continuous measurements of the beat frequency against the same comb mode throughout an entire scan, which was typically 0.9 GHz in length. In the future, this "soft lock" of the comb to the laser could be replaced by a system that directly locks the Ti:Sapphire laser to the comb; in such a scenario the laser could be scanned over long ranges simply by stepping f_{rep}.

The laser frequency can be determined using the equation $f_{Ti:S} = nf_{rep} + 2f_{ceo} + f_{beat}$. The difficulty in using the frequency comb for absolute calibration is that neither n (the comb mode participating in the beat) nor the signs of f_{ceo} and f_{beat} are known a priori. The sign of f_{beat} is easily determined by monitoring the change in $|f_{beat}|$ as the laser is tuned: if $|f_{beat}|$ increases as $f_{Ti:S}$ is increased, then its sign must be positive. The sign of f_{ceo} can only be determined by changing $|f_{ceo}|$ while watching $|f_{beat}|$ while the laser is held at a constant frequency. However, this last step was inadvertently omitted in the present experiment, so the sign of f_{ceo} is unknown in our measurements; however, all the ultra-high resolution scans reported here were recorded on two consecutive days, and the (unknown) sign of f_{ceo} was fixed by its lock, which was left on continuously during that period.

The value of the comb mode n was determined by using an estimate of $f_{Ti:S}$ from the wavemeter, which we

call f_{wm}. For each possible sign of f_{ceo}, an estimate of n was calculated using $n_{\pm} = (f_{wm} \mp 2f_{ceo} - f_{beat})/f_{rep}$. These estimates can be expected to differ from an integer by an amount as large as 0.65, which represents the absolute accuracy of the wavemeter divided by f_{rep}. We found that in all cases only a single integer was within 0.65 of n_-, so that the determination of the true integer value of n_- was unambiguous. This was also true in some cases for n_+; these cases were used to determine the difference between f_{wm} and $f_{Ti:S}$ under the assumption that f_{ceo} is positive. We found that the wavemeter's offset varied by $\lesssim$8 MHz over the course of a day, so that this could be used to "calibrate" the wavemeter and unambiguously determine the integer value of n_+. For all scans, we found that $n_+ = n_- - 1$, and consequently the two possible values of $f_{Ti:S}$ for the two signs of f_{ceo} differ only by $f_{rep} - 2|2f_{ceo}| = 20.005$ MHz. For the remainder of this paper, we adopt the value corresponding to a negative f_{ceo}, but we caution that all of our frequencies may be overestimated by 20.005 MHz as a result. In the future, this ambiguity can be resolved by a direct determination of the sign of f_{ceo} and/or by using a more accurate wavemeter. Nevertheless, the precision of the frequency determination at each step is $\sim$1 MHz.

A.4 Transition Frequencies

Ten transitions of the Q_{22} branch of the v=1$\leftarrow$0 band of the Meinel system $A^2\Pi_u$-$X^2\Sigma_g^+$ of N_2^+ were observed in ultra-high resolution scans. A representative set of high and ultra-high resolution scans of the $Q_{22}(14.5)$ line are shown in Figure A.2. The vertical line represents the previously reported line center from the Doppler limited work of Ferguson et al. [30], and the horizontal line represents their stated calibration uncertainty ($\pm$150 MHz). Of the ten observed transitions, eight were previously observed by [30], but $Q_{22}(0.5)$ and $Q_{22}(2.5)$ are reported here for the first time.

In the work of Ferguson et al. [30], many closely spaced transitions were unresolvable because of the Doppler-limited linewidths. Given the narrow sub-Doppler Lamb dips in the present work, many of these "blended" transitions are now resolvable. For example, the $R_{11}(10.5)$ transition was previously blended with the stronger $Q_{22}(11.5)$ transition. As shown in Figure A.3, the Lamb dips of these two transitions are clearly separated.

Each Lamb dip was fit to a Gaussian profile to determine the value of and the uncertainty in the line center frequency. Because of the relatively low S/N ratio of the wings of the Lamb dips, the profiles could be fit equally well to a Gaussian or a Lorentzian; a Gaussian fit was chosen because it was less sensitive to the noise in the wings of the observed dips. Table A.1 shows our line center frequencies, the differences between these and the previous measurements, and the differences between our frequencies and the predictions of an

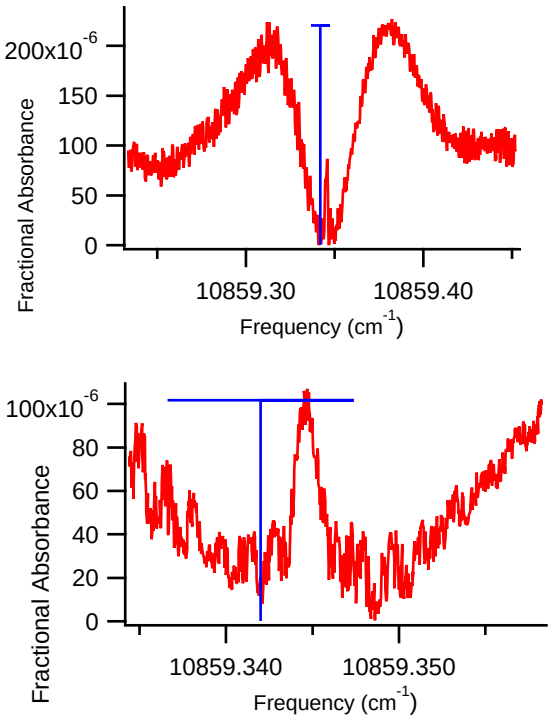

Figure A.2: High-resolution (wavemeter calibrated) and ultra high-resolution (comb calibrated) scans of the $Q_{22}(14.5)$ line. The vertical line represents the previously reported line center [30]. The Lamb dip occurs within the uncertainties of the previous measurement, which is represented by the horizontal line.

effective Hamiltonian fit.

The differences between our line centers and those of [30] are reasonably small, but are in some cases larger than the previous work's estimated precision of about 0.002 cm^{-1} (which may apply only to the stronger transitions of [30]). The higher precision of the present work is evident from the residuals from the effective Hamiltonian fit (which used the constants from [30]). These residuals are tightly clustered around $+0.003$ cm^{-1}, with a standard deviation of 0.0004 cm^{-1}. This suggests that the molecular constants of this widely used prototype ion could be significantly improved using this method of sub-Doppler spectroscopy.

A.5 Linewidth Investigation

In our initial report on cavity enhanced velocity modulation spectroscopy [89], the observed linewidth of the Lamb dips ($\sim$130 MHz) was dominated by the mechanical instability of the cavity, and the resulting frequency jitter in the laser (which was locked to the cavity). With our improved lock of the cavity to the laser, a considerably smaller Lamb dip linewidth (as low as 40 MHz) is observed. However, this width is still quite a bit larger than expected from pressure broadening, so we have investigated its dependence on

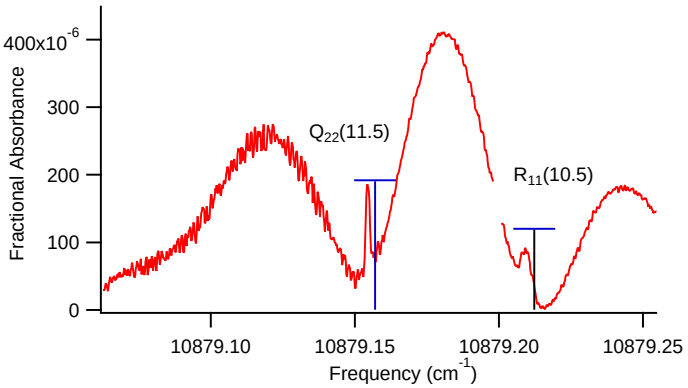

Figure A.3: The high resolution scan of the $Q_{22}(11.5)$ line shows a second Lamb dip where the previously blended and unreported $R_{11}(10.5)$ line is now clearly resolved. The vertical line near $R_{11}(10.5)$ represents the predicted position from an effective Hamiltonian fit, and the horizontal bar indicates the rms-error of the Hamiltonian fit. The lock-in time constant was increased half-way through the scan which reduced the noise of the scan and broadened the observed $R_{11}(10.5)$ Lamb dip.

J	Observed	Obs.−[30]	Obs.−Calc.
0.5	10924.65608(10)	—	0.00408
2.5	10919.46795(4)	—	0.00325
4.5	10912.92682(3)	0.00182	0.00322
6.5	10905.01953(3)	0.00853	0.00313
7.5	10900.54840(3)	0.00540	0.00310
8.5	10895.72876(3)	0.00076	0.00286
9.5	10890.55859(5)	0.00359	0.00299
11.5	10879.15394(3)	-0.00306	0.00294
12.5	10872.91398(3)	-0.00002	0.00288
14.5	10859.34469(3)	0.00269	0.00279

Table A.1: Doppler free transition frequencies (in cm^{-1}) of the $Q_{22}(J)$ series calibrated with a frequency comb, as well as the differences from the previously published values[30], and the differences from an effective Hamiltonian fit using the spectroscopic constants from [30]. Note that the observed frequencies may be systematically too high by 20 MHz due to an ambiguity in the sign of f_{ceo} (see text).

the cell pressure, rotational level, and laser power.

A graph of the FWHM of the $Q_{22}(14)$ transition at several pressures between 0.5 and 4.5 Torr is shown in Figure A.4. The calculated pressure broadening coefficient, assuming a Langevin collision rate and using the formulas in [75], is approximately 1.8 MHz/Torr. Not only is the slope of the observed pressure dependence (8 MHz/Torr) much higher than this, but there is also a significant linewidth (32 MHz) even at the limit of zero pressure. Clearly an effect other than pressure broadening is dominating the observed linewidth.

To investigate the possible role of hyperfine structure on the observed linewidth, we measured transitions from many rotational states at the same pressure of 0.35 Torr. No change in the FWHM as a function of the rotational quantum number was observed. To check for power broadening, we measured the FWHM of

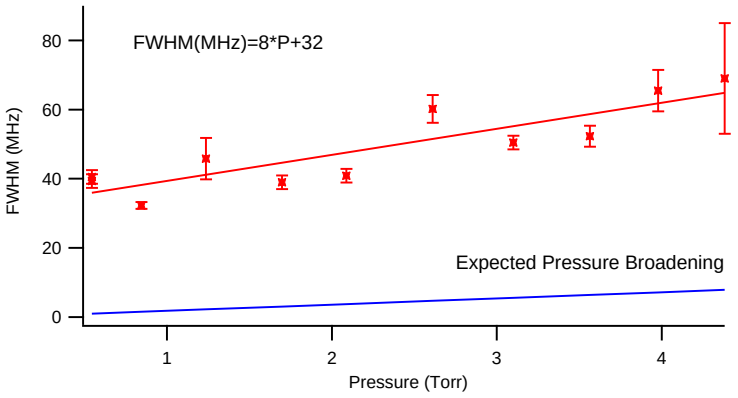

Figure A.4: Linewidth as a function of cell pressure shows that the actual linewidth is much larger than the expected pressure broadening. Line of best fit: FWHM(MHz)=8×p (Torr) + 32

the $Q_{22}(14.5)$ transition at incident optical powers between 7 and 30 mW, and observed no change over this range.

It seems clear that some other process is dominating the linewidth of the Lamb dips. We propose a lifetime broadening mechanism, based on the amount of time that a particular ion will be resonant with both counter-propagating laser beams (and thus participate in the Lamb dip) before its velocity is significantly changed by the AC field of the velocity modulation.

To estimate the order of magnitude of this effect, we assume that the drift velocity of the ions is proportional to the instantaneous voltage applied to the discharge cell. From the observed Doppler shift between the line center and the maxima of the velocity-modulated line profiles, we estimate the peak drift velocity to be ∼72000 cm/s, which corresponds to a peak Doppler shift of ∼800 MHz. In order for an ion to be probed by both directions of the laser beam in the cavity, its velocity along the cavity axis must be close enough to zero that its Doppler shift with respect to both beams is smaller than the cavity linewidth (∼0.5 MHz). Since the Doppler shift changes from ∼800 MHz to 0 MHz in one quarter of a discharge cycle (∼6 μs), the ion has an effective "lifetime" of only ∼4 ns, which corresponds to a lifetime broadening of ∼40 MHz, in rough agreement with our observations. The origin of the observed pressure dependence is unclear at the present time.

A.6 Saturation Parameter

Figure A.5 shows the experimentally observed Lamb dip depth as a function of the laser power incident on the cavity, which was adjusted by a variable attenuator on the RF input of the AOM (which changed its

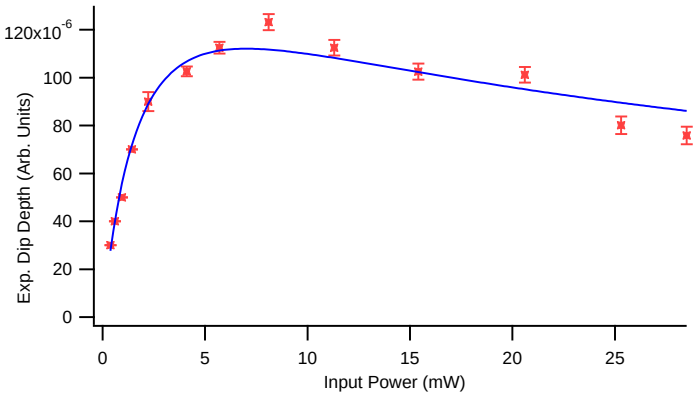

Figure A.5: Experimentally observed Lamb dip depth, together with theoretical fit.

diffraction efficiency) while keeping all other experimental parameters constant. Theoretically [4], one would expect the ratio of the dip depth to the Doppler-limited absorption depth to be equal to $(1+S)^{-1/2} - (1+2S)^{-1/2}$, where S is the saturation parameter. Since the Doppler-limited absorption depth is independent of power, and S is proportional to the incident power, we fit the observed dip depth to the expression $A\left[(1+kP_{in})^{-1/2} - (1+2kP_{in})^{-1/2}\right]$. As seen in Figure A.5, the fit is quite good; the resulting constant of proportionality is $k = 0.20 \pm 0.01$ mW^{-1}.

The saturation parameter S can be conveniently defined as Ω^2/Γ^2, where Ω is the angular Rabi frequency and Γ is the relaxation rate. Given that $\Omega = \mu E/\hbar$ (where μ is the transition dipole moment and E is the electric field strength), that the field intensity $I = E^2 c/8\pi$, and also that the field intensity inside the cavity can be expressed as $I = F\eta P_{in}/\pi r_0^2$ (where F is the cavity finesse, η is the coupling efficiency into the cavity [or the ratio P_{out}/P_{in}], and r_0 is the beam radius inside the cavity), we can write S in terms of P_{in} as

$$S = kP_{in} = \frac{8\pi}{c\hbar^2}\frac{\mu^2}{\Gamma^2}\frac{\eta F}{\pi r_0^2}P_{in} \tag{A.1}$$

or, given an experimentally determined constant of proportionality k, we can write

$$\frac{\mu^2}{\Gamma^2} = k\frac{c\hbar^2}{8\pi}\frac{\pi r_0^2}{\eta F}. \tag{A.2}$$

Substituting in the appropriate values for our case ($F = 250$, $\eta = 0.008$, $r_0 = 0.07$ cm, and $k = 2\times10^{-5}$ s erg^{-1}), we find that $\mu/\Gamma = 0.090$ Debye/MHz.

According to lifetime measurements [76], the Einstein coefficient for the 1-0 Meinel band is $\sim 7\times10^4$ s^{-1}; this is in good agreement with the theoretical value [37] of 5.9×10^4 s^{-1}. Combining this with the linestrength

of the $Q_{22}(14)$ transition used for these measurements (computed from PGopher [104]), the transition dipole moment is expected to be $\mu = 0.38$ Debye. This suggests a relaxation rate $\Gamma \approx 4.2$ MHz. This demonstrates the ability of cavity enhanced velocity modulation Lamb dip spectroscopy to determine the ratio μ/Γ.

A.7 Conclusions and Outlook

We have demonstrated that cavity enhanced velocity modulation spectroscopy can be used to make high precision (∼1 MHz) measurements of molecular ion spectra, when used in conjunction with an optical frequency comb. This method provides considerably higher precision than conventional Doppler-limited spectroscopy, and consequently offers the prospect of more accurate determinations of molecular constants. Quantitative measurements of the Lamb dip depth also offer the possibility of experimentally determining transition dipole moments.

Although our initial demonstration of this method has utilized an electronic transition of a molecular ion, we see no reason why this method could not be extended to vibrational spectroscopy in the mid-infrared. Typical vibrational dipole moments are on the order of 0.15 D, and this vibronic dipole moment was only 0.43 D, therefore the power density would only need to be about 10 times higher. This increased intracavity power could be achieved by using a higher finesse cavity or a higher power laser (e.g., a cw OPO). In such a case, frequency calibration could be performed either with a mid-infrared comb [1], or by upconverting the mid-infrared laser to the near-infrared by sum frequency generation with a stabilized Nd:YAG laser in a periodically poled lithium niobate crystal.

The widths of the Lamb dips are comparable to the kinematically compressed linewidths of ion beam instruments [17], therefore similar precision can be obtained with the current type of instrument. Ion beam instruments are considerably more complex and suffer from reduced ion density, but do offer other advantages, including simultaneous mass spectrometry, mass identification spectral lines, and the possibility of rotational cooling when used with supersonic ion sources.

High-precision sub-Doppler vibrational spectroscopy of molecular ions would enable determination of molecular constants with near-microwave precision, which could in turn facilitate the prediction of pure rotational transitions. This could be very useful in reducing the classic "search problem" in rotational spectroscopy, and could also facilitate astronomical observations of molecular ions that have not been measured in the microwave, sub-mm, or THz regions. Furthermore, the high precision of this method would facilitate the identification of four-line combination differences in complex spectra (such as, for example, CH_5^+ [105, 83]) and thereby provide additional information to enable their assignment.

A.8 Acknowledgments

The authors are grateful to Prof. Benjamin Lev and Mr. Mingwu Lu for very helpful advice regarding laser locking electronics and techniques. This work has been supported by the NASA Laboratory Astrophysics program (NNX08AN82G), by an NSF CAREER award (CHE-0449592), by an Air Force Young Investigator award (FA9550-07-1-0128), and by the David and Lucile Packard Foundation.

Appendix B

Sub-Doppler Mid-Infrared Spectroscopy of Molecular Ions

B.1 Abstract

The technique of velocity modulation spectroscopy has recently been combined with cavity enhancement and frequency modulation methods into a technique called noise-immune cavity-enhanced optical heterodyne velocity modulation spectroscopy (NICE-OHVMS). We have implemented NICE-OHVMS with a cw-optical parametric oscillator (OPO) tunable from 3.2-3.9 μm, and used it to record spectra of the $R(1,0)$ and $R(1,1)^u$ transitions of the ν_2 fundamental band of H_3^+. The high optical power and cavity enhancement enable saturation of rovibrational transitions, which allows for line center frequencies to be measured with a precision of 70 kHz.

B.2 Introduction

Molecular ions play a key role as intermediates in chemical reactions, and a detailed understanding of their structure and intramolecular dynamics in the gas phase, generally obtained by spectroscopy, is a critical first step toward understanding their behavior in more complicated systems. The primary technique used for ion spectroscopy over the past 30 years has been velocity modulation spectroscopy (VMS). [40, 41] In VMS, ions are produced in an AC positive column plasma whose polarity is alternated at frequency f_{vm}. The average drift velocity of the ions in the plasma is shifted toward the cathode from the applied electric field, while neutral molecules are generally unaffected. As the polarity is reversed, the average ion drift velocity also reverses, resulting in a periodic oscillation in the ion velocity distribution at f_{vm}. By interrogating the ions with a laser beam passing in one direction through the plasma, the absorption profiles are alternately red- and blue-shifted with respect to their rest frequencies, and phase-sensitive detection at f_{vm} allows for selective retrieval of ionic signals. VMS therefore addresses one of the main challenges of

This chapter was first published as: K. N. Crabtree, J. N. Hodges, B. M. Siller, A. J. Perry, J. E. Kelly, P. A. Jenkins II, and B. J. McCall,"Sub-Doppler Mid-Infrared Spectroscopy of Molecular Ions", *Chemical Physics Letters*, **551**, 1-6 (2012).[19]

ion spectroscopy, i.e., detection of ionic species that are only $\sim 10^{-5}$-10^{-6} as abundant as neutral molecules. Well over 40 unique molecular ions (not including isotopologues) have been detected with VMS; these have been extensively reviewed by Stephenson and Saykally. [93]

Recently, the use of a Fabry-Perot optical cavity to enhance the optical path length was demonstrated by Siller et al. (cavity-enhanced velocity modulation spectroscopy, CEVMS), who locked a Ti:Sapphire laser to an optical cavity surrounding a velocity modulated positive column cell and detected the transmitted light. [89] Because the light in the cavity is bidirectional, red and blue Doppler shifts are simultaneously superimposed, encoding the velocity modulation (VM) signal at $2f_{vm}$. Initially, this was believed to be problematic because any neutral molecules produced or excited by the discharge are concentration modulated (CM) at $2f_{vm}$; that is, the population of the excited species varies with the magnitude of the applied voltage, but not the sign of the voltage. By also encoding the ion signal at $2f_{vm}$, it was thought the concentration modulation signal of neutral molecules would overwhelm the ion velocity modulation signal. Siller et al. showed that the ion and neutral signals occurred at different phases with respect to the plasma voltage, thereby preserving ion-neutral discrimination through phase-sensitive detection. Additionally, the power enhancement from the optical cavity enables saturation spectroscopy and precise line-center determination. [68] A related technique has also been employed using an optical frequency comb as the light source and a unidirectional ring cavity surrounding a plasma cell, effectively converting VMS to a broadband technique while preserving the high resolution of laser spectroscopy. [91]

Cavity enhanced absorption spectroscopy suffers from the fact that frequency noise in the laser is directly converted into intensity noise as a result of reduced cavity transmission. This limitation was overcome by Ye et al. with noise-immune cavity-enhanced optical heterodyne molecular spectroscopy (NICE-OHMS). [114] In this technique, the laser is phase modulated at f_h (typically $\sim$100s of MHz), effectively generating an FM triplet consisting of a carrier (at the optical frequency f_o) and a pair of sidebands with opposite phase at $f_o \pm f_h$. The triplet is coupled into the optical cavity by setting f_h equal to an integer multiple of the cavity free spectral range (FSR). In the absence of any intracavity absorption or dispersion, the beat notes between each sideband beating with the carrier are balanced in both amplitude and phase, so there is no net signal at f_h. However, in the presence of an intracavity absorber or disperser, the beat notes are unbalanced in amplitude and/or phase, yielding a net signal. By encoding absorption/dispersion information at a high frequency, $1/f$ technical noise is reduced. Another advantage is that any laser frequency noise affects the cavity coupling efficiency of the carrier and both sidebands equally, which keeps the beat notes of each sideband with the carrier balanced, and eliminates direct conversion of laser frequency noise to noise in the final spectrum. The disadvantages are the complexity of the technique, particularly the demands of

maintaining the laser-cavity lock, and the requirement of a detector whose bandwidth is at least f_h. An extensive review of the NICE-OHMS technique has been published by Foltynowicz et al. [33]

CEVMS and NICE-OHMS have been combined into a technique called noise-immune cavity enhanced optical heterodyne velocity modulation spectroscopy (NICE-OHVMS) in the near-infrared with a Ti:Sapphire laser. [90] Because f_h and f_{vm} are at significantly different frequencies (typically ∼100 MHz and ∼10 kHz, respectively), the detector signal is first demodulated at f_h, and then sent on to further phase-sensitive detection at $2f_{vm}$. NICE-OHVMS preserves the ion-neutral discrimination afforded by VMS, and takes advantage of the ultra-high sensitivity, saturation, and noise immunity of NICE-OHMS.

However, the technical demands of the NICE-OHMS technique have largely precluded its use in the mid-infrared spectral region in which VMS has been successfully exploited. The high bandwidth detectors and phase modulators required for NICE-OHMS are not as readily available in the mid-IR compared with the visible/near-IR. The only published mid-IR NICE-OHMS work was done with a quantum cascade laser near 8.5 μm, and was limited by the detector bandwidth and the phase modulation characteristics of the device. [96] Work is currently underway in our laboratory to extend NICE-OHMS into the mid-IR using a difference frequency generation (DFG) source in the 3-5 μm region [78], which is particularly attractive for a general-purpose ion spectrometer because the vast majority of molecules have at least one fundamental vibrational band in that portion of the spectrum.

Here we report the first mid-IR NICE-OHVMS spectrometer, which uses a commercially available cw-optical parametric oscillator (OPO) tunable from 3.2-3.9 μm. The high optical power of the OPO (∼1 W) allows for use of high bandwidth mid-IR detectors that are not sensitive enough to be used with many other lower-power cw lasers in this region. This technique enables all of the advantages of the NICE-OHVMS technique to be brought to bear on fundamental vibrational transitions of molecular ions, including high precision sub-Doppler spectroscopy.

Our initial demonstration of this instrument focuses on the study of H_3^+, which is the simplest polyatomic molecular ion and serves as the primary initiator of ion-molecule chemistry in interstellar clouds. [101, 45] Its infrared spectrum was first observed by Oka in 1980, [72] and since then it has been extensively studied spectroscopically (see, for instance, the review in Ref. [59]). More recent research on H_3^+ focuses on spectroscopy above the so-called "barrier to linearity," at which point the molecule adopts a linear geometry that induces a singularity in the Hamiltonian, complicating its theoretical treatment. [71] Nevertheless, for the lowest-lying energy levels, the agreement between experiment and ab initio theory is good to spectroscopic accuracy. [99] Measuring the energy level spacings experimentally with higher precision and accuracy would present a greater challenge for ab initio theory, possibly spurring new developments. The NICE-OHVMS

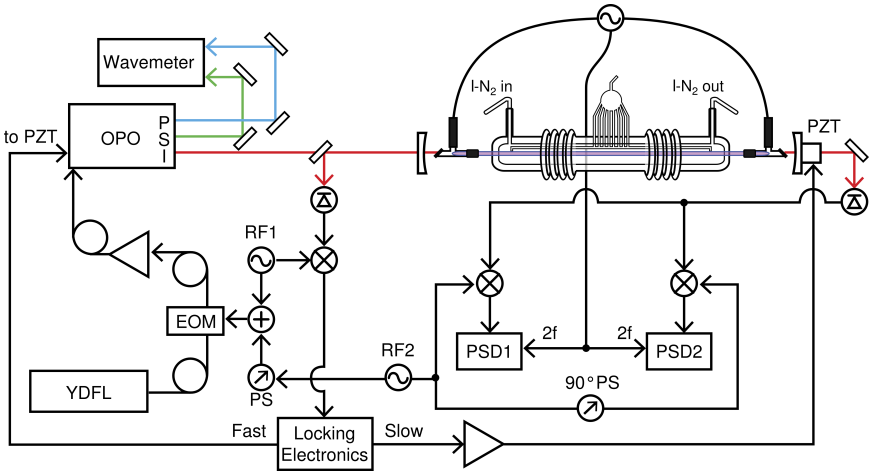

Figure B.1: Block diagram of NICE-OHVMS instrument. Details of its operation are given in the main text. YDFL: Ytterbium-doped fiber laser; EOM: electro-optic modulator; OPO: optical parametric oscillator with pump (P, blue), signal (S, green) and idler (I, red) beams; PZT: piezoelectric transducer, PS: phase shifter; PSD: phase sensitive detector; •: signal splitter.

technique opens the possibility of measuring such energy level spacings in H_3^+.

As a demonstration of the capabilities of this instrument, we present in this paper spectra of the ν_2 fundamental band of H_3^+ at 3.67 μm. In section B.3 we describe the instrumental details, and in section B.4 we discuss NICE-OHVMS lineshapes and present spectra acquired with the instrument. Finally, in section B.5, the performance of the instrument is assessed, and future directions are discussed.

B.3 Experimental Details

Our NICE-OHVMS instrument is outlined in Figure B.1. A Ytterbium-doped fiber laser (YDFL, Koheras Adjustik Y-10), which acts as the seed laser, is sent through a fiber EOM (EOSPACE PM-0K5-00-PFU-PFU-106-S), amplified (IPG Photonics YAR-10K-1064-LP-SF), and used to pump a singly-resonant OPO (Aculight Argos 2400 SF). The pump (1.064 μm) and signal (1.5-1.6 μm) beams are sent to a wavemeter (Burleigh WA-1500) for frequency calibration. The idler (3.2-3.9 μm) is locked with the Pound-Drever-Hall (PDH) technique to a 1.9-m-long optical cavity consisting of two 1 m radius of curvature concave Si mirrors dielectric coated for 99.7% reflectivity over 3.1-3.4 μm surrounding a plasma cell. Cavity reflection and transmission are monitored by photodiodes (Boston Electronics Vigo PVM-10.6-1x1) with an effective bandwidth of ~125 MHz.

Heterodyne and PDH sidebands are generated by applying voltages at their respective frequencies to the fiber EOM on the seed laser simultaneously. The resultant frequency spectrum of the pump laser is imprinted on the idler beam. A PDH error signal used for cavity locking is generated by demodulating the

cavity reflection signal at the frequency RF1 (typically 2-20 MHz). The error signal is sent to feedback electronics which stabilize the length of the cavity on slow timescales via a piezoelectric transducer (PZT) attached to one of the cavity mirrors, and apply fast corrections to the idler frequency by a PZT mounted to one of the signal cavity mirrors inside the OPO head. The cavity transmission detector signal is sent to a pair of mixers $\sim 90^\circ$ out of phase with one another, and each is demodulated at frequency RF2 (equal to the cavity FSR of 79.12 MHz). The overall phase of the heterodyne detection is adjusted by phase shifting the RF signal driving the EOM using cables of appropriate lengths. The demodulated signal from each mixer is then sent to a lock-in amplifier referenced to twice the frequency used to drive the plasma, and the in-phase and quadrature outputs of each amplifier are digitized and stored on a computer.

Ions are produced in a liquid-nitrogen-cooled multi-inlet multi-outlet positive column discharge cell, which is placed between the two free-standing mirrors of the optical cavity. [60] Intracavity radiation is admitted into the cell by means of CaF_2 windows aligned at Brewster's angle. The plasma is driven by a 40 kHz sine wave voltage produced by amplifying the output of an arbitrary waveform generator with an audio amplifier (Techron 7780) and a step-up transformer. H_3^+ was produced at a pressure of 200 mTorr and a discharge current of 170 mA. The outputs of the two mixers were each demodulated at 80 kHz with a lock-in amplifier set to a 10 ms time constant (16 Hz detection bandwidth).

Typical operation begins by filling the cooling jacket of the cell with liquid nitrogen and igniting the plasma. The cavity length is adjusted to bring it into resonance with the laser, and the laser-cavity lock is established. The idler frequency is tuned by applying a voltage to an internal PZT on the YDFL, and the cavity length is controlled with the locking electronics to maintain the resonance condition. When the cavity PZT reaches the end of its travel, the laser-cavity lock is electronically interrupted, the cavity length is reset to the other end of its travel, a new resonance is found, and the lock is reestablished. In this manner, the spectrometer can scan without manual intervention over the entire range of the YDFL PZT (around 100 GHz), although in practice a scan is generally much shorter. It is in principle possible to extend the automated tuning range further by electronic control of the intracavity etalon of the OPO and the nonlinear crystal position/temperature, but the practical utility of such efforts would likely be minimal.

B.4 Results and Analysis

B.4.1 Lineshapes

The overall Doppler lineshape for NICE-OHVMS in both absorption and dispersion has odd symmetry, and qualitatively appears similar to the third derivative of a Gaussian absorption profile. A detailed analysis of

the lineshape is beyond the scope of this paper and will be the subject of a future work, but a qualitative description follows. Consider a general NICE-OHMS lineshape such as that shown in panels a and b of Figure 2 in Ref. [33]. If the signal belongs to an ion, then the AC voltage of the plasma causes velocity modulation (VM), Doppler shifting the lineshape at the plasma frequency. As a result of the bidirectional nature of light in our optical cavity, the lineshape is simultaneously Doppler shifted to the red and to the blue by the same amount at each point in time along the plasma voltage cycle. Consequently, the time-dependent signal repeats itself every plasma half-cycle, or at twice the AC plasma frequency ($2f_{vm}$). In addition to VM, an ion also experiences concentration modulation (CM) at $2f_{vm}$, and CM may be phase shifted with respect to VM. Thus, in addition to a periodic Doppler shift at $2f_{vm}$ from VM, the lineshape amplitude varies at $2f_{vm}$ from CM. The net signal observed comes in 4 channels corresponding to the even and odd second order Fourier coefficients of the absorption and dispersion profiles affected by VM and CM.

The sub-Doppler lineshape is more straightforward. As has been discussed in regard to previous NICE-OHMS setups [34, 5, 90], the carrier and sidebands can each act as pumps and probes for saturation spectroscopy. The Lamb dips arising from the Bennet holes burned in the population appear at half-integer multiples of the carrier-sideband spacing f_h, i.e. at all frequencies at which forward- and reverse-propagating beams sample the same velocity component of the Doppler distribution. At the line center ν_0, when the zero-velocity distribution is both pumped and probed by the carrier, a signal only appears in dispersion as the heterodyne detection scheme employed by NICE-OHMS is insensitive to absorption of the carrier. In the current work, the heterodyne modulation index (β) is small enough (~ 0.63) that only the carrier has sufficient power to saturate transitions, while the sidebands can only act as probes. The dispersion signal therefore contains Lamb dips at ν_0 and $\nu_0 \pm f_h/2$, while the absorption signal contains them at $\nu_0 \pm f_h/2$.

While VM and CM have a strong influence on the lineshape of the Doppler profile, they do not affect the sub-Doppler features in the same way. Because Bennet holes are only burned in the population at or spaced evenly around the zero-velocity component of the ion distribution, VM effectively changes the abundance of ions with the appropriate velocity. In that way, VM effectively behaves like CM, and the net effect is to influence the amplitude of the Lamb dip lineshape and the relationship between the amplitudes of the even and odd Fourier coefficients within absorption or dispersion. Neglecting any change of the ions' collision rate with changing velocity, VM and CM do not affect the sub-Doppler profile beyond its amplitude. The

sub-Doppler lineshape function [90] is

$$\begin{aligned}\chi(\nu_d) = &\left(A_1\left[\chi_a\left(\nu_d - \frac{f_h}{2}\right) - \chi_a\left(\nu_d + \frac{f_h}{2}\right)\right]\right)\sin\theta_h \\ &+ \Bigg(-2A_0\chi_d(\nu_d) + \\ &A_1\left[\chi_d\left(\nu_d - \frac{f_h}{2}\right) + \chi_d\left(\nu_d + \frac{f_h}{2}\right)\right]\Bigg)\cos\theta_h, \end{aligned} \tag{B.1}$$

where ν_d is the frequency detuning from the transition center frequency, θ_h is the heterodyne detection phase, A_0 is the effective amplitude of the central (carrier-carrier) dispersion Lamb dip, and A_1 is the effective amplitude of the carrier-sideband Lamb dips for absorption and dispersion. $\chi_a(\omega)$ is a Lorentzian lineshape function for absorption, and $\chi_d(\omega)$ is a lineshape function for dispersion related to $\chi_a(\omega)$ by the Kramers-Kronig relations. These are defined as

$$\begin{aligned}\chi_a(\omega) =& \frac{1}{1+\gamma^2(\omega-\omega_0)^2} \quad \text{and} \\ \chi_d(\omega) =& \frac{-(\omega-\omega_0)\gamma}{1+\gamma^2(\omega-\omega_0)^2},\end{aligned}$$

where ω_0 is the center and γ is the inverse of the half-width at half-maximum. When using this fit function, f_h is held at the cavity FSR (79.12 MHz), the amplitudes are constrained such that $A_0 > A_1$, and the Doppler profile near the line center is approximated by a third-order polynomial with the quadratic term set to 0.

B.4.2 H_3^+ Spectra

A sample spectrum of the $R(1,0)$ and $R(1,1)^u$ transitions of the ν_2 fundamental band of H_3^+ is shown in Figure B.2. The signals in the top and bottom panels are the demodulated in-phase (black) and quadrature (red, offset) components of the two mixers, which in our setup we measure to be 96° out of phase with one another. The in-phase components of the $R(1,0)$ transition are shown in greater detail in Figure B.3. The overall lineshape is slightly asymmetric; the blue side of the transition is stronger than the red side, particularly in mixer 2. The origin of this asymmetry is unknown, and its impact on the spectroscopic accuracy will be discussed below.

A simultaneous fit of the $R(1,0)$ sub-Doppler features in all four detection channels to Equation B.1 is shown in Figure B.4. A number of constraints were employed to ensure that the fit parameters were all internally consistent. The line center frequency and Lamb dip width were forced to be equal for all four data

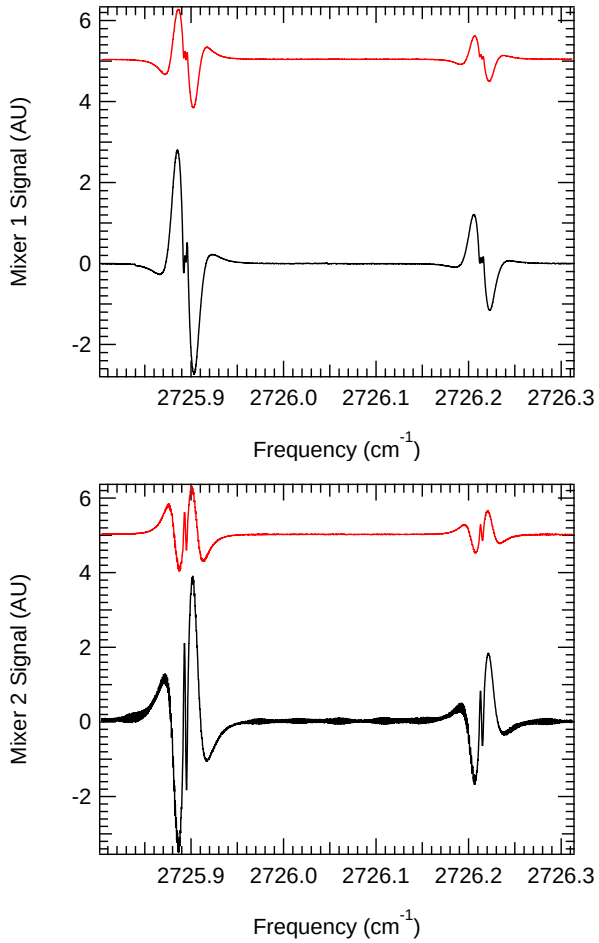

Figure B.2: NICE-OHVMS spectrum of the $R(1,0)$ and $R(1,1)^u$ transitions of the ν_2 fundamental band of H_3^+. Each panel shows the in-phase (black, bottom) and quadrature (red, top) outputs of a lock-in amplifier demodulating the indicated mixer's signal.

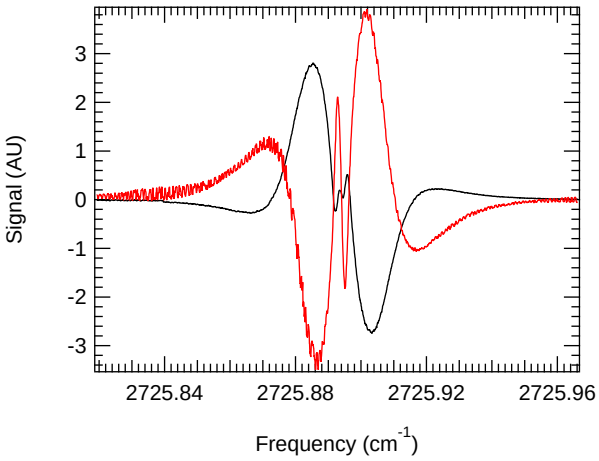

Figure B.3: NICE-OHVMS spectrum of the $R(1,0)$ transition of the ν_2 fundamental band of H_3^+. The black trace is the in-phase output of mixer 1, and the red is the in-phase output of mixer 2.

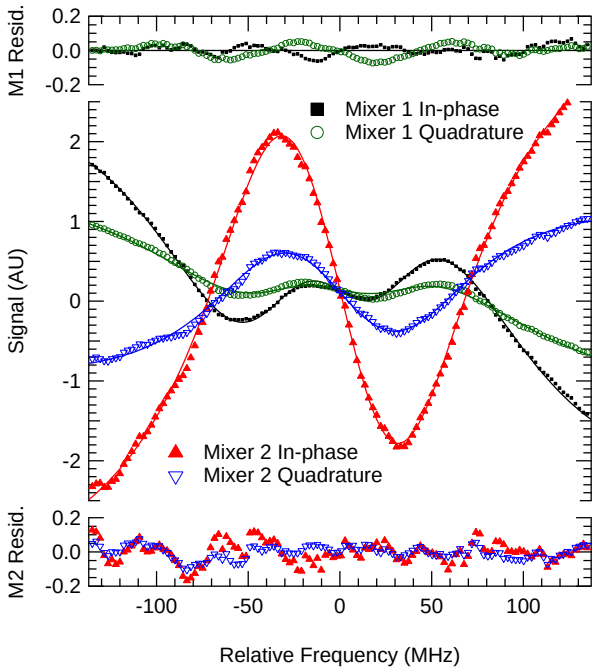

Figure B.4: A simultaneous fit of the central sub-Doppler region of the H_3^+ $R(1,0)$ transition from all four data channels to Equation B.1. The symbols in the central portion of the graph are the data, and the solid lines are the fit results. The residuals of the fits are shown in the upper panel for mixer 1 and in the lower panel for mixer 2; in each case the symbols correspond to those in the central panel.

channels. Mixers 1 and 2 were held at 96° apart, and the sideband spacing with held equal to the cavity FSR of 79.12 MHz. Because the in-phase and quadrature components of each mixer sample different blends of CM and VM, the Lamb dip amplitudes were allowed to be different for the in-phase channels and the quadrature channels. However, the two in-phase channels were forced to have equal Lamb-dip amplitudes, and likewise for the two quadrature channels. After all of these constraints, there are a total of 19 fit parameters for the entire data set: the line center frequency ν_0, the Lamb dip full width at half maximum $(2/\gamma)$, the overall detection phase θ_h, Lamb dip amplitudes A_0 and A_1 for the in-phase channels and the quadrature channels, and baseline terms of the form $c_0 + c_1 x + c_3 x^3$ to approximate the central portion of the Doppler profile in each channel.

The overall quality of the fit is quite good; the residuals are composed primarily of fringing evident on top of the spectrum (especially mixer 2) with the notable exception of the quadrature channel of mixer 1, which has some small systematic deviations on the Lamb dips. The line center ν_0 derived from the fit is $2725.89401954 \pm 0.0000023$ cm^{-1}, but the absolute accuracy is limited by the $> 2 \times 10^{-3}$ cm^{-1} accuracy of the wavemeter, so the exact frequency should not be trusted. More important is the uncertainty of the line center determination, which is ∼70 kHz; this represents the maximum potential accuracy of the

technique provided suitable frequency calibration is made (but see the discussion below about the effects of the asymmetry). The overall detection phase θ_h was found to be 132°, indicating a blend of absorption and dispersion in each mixer. Because the Lamb dip widths (full width at half maximum of ∼110 MHz as indicated by our fit) are much broader than the Lamb dip spacing of 39.56 MHz ($f_h/2$), the individual Lamb dips for absorption and dispersion cannot be resolved at any RF detection phase. Rather than tuning the phase to separate absorption from dispersion in the two mixers, a phase of 132° was chosen because it was found to isolate the fringing as much as possible in a single detection channel (mixer 2 in-phase), thus minimizing the fringing in the other 3 channels.

B.5 Discussion

The most interesting aspect of the NICE-OHVMS technique is the presence of Lamb dips which enables high precision measurements of line center frequencies. As demonstrated above with H_3^+, the precision of the line center determination is on the order of 70 kHz. In its present implementation, the technique's accuracy is limited by the wavemeter, and also by slow drifts in the frequency of the signal and idler beams caused by thermal fluctuations of the OPO cavity. Use of an optical frequency comb to stabilize and measure the frequencies of the pump and signal beams would reduce the accuracy uncertainty to < 100 kHz. Ultimately, the total uncertainty of the technique will be determined by the reproducibility of line center determinations once appropriately calibrated.

The asymmetry observed in the overall NICE-OHVMS lineshape can adversely affect the overall accuracy. As mentioned above, the origin of this asymmetry is unknown, although it varies with heterodyne detection phase; similar effects were not observed in the near-IR implementation of NICE-OHVMS. [90] Nevertheless, we have performed simulations of the effects of the asymmetry by synthesizing skewed profiles and comparing the results of our fit function to the actual location of the Lamb dips. Based on the fitting of our simulations, we estimate that the magnitude of this line center shifting to be less than a few MHz, even for Doppler profiles that are much more asymmetric than those shown in this paper. Further study of this phenomenon will be possible with an optical frequency comb, and such work is envisioned in the near future.

The width of the Lamb dips (∼110 MHz FWHM from the fitting) is fairly broad. We have varied the intracavity laser power and the cell pressure, but any differences in the linewidth were not observable. However, the ranges of the power and pressure measurements were limited: the intracavity power could only be changed by a factor of 2 before the laser-cavity lock was adversely affected, and the plasma could only give stable operation over 200-600 mTorr. Such wide Lamb dips were also observed in the NICE-OHVMS

experiment performed on N_2^+ in the near-IR [90]; in that study, the authors were able to observe a change in linewidth with pressure, but extrapolating to zero pressure still gave a linewidth of ∼30 MHz. Assuming that the linewidth is related to the time an ion spends at zero velocity, it is perhaps unsurprising that a less massive ion like H_3^+ has a broader linewidth than N_2^+, as its velocity may be more easily altered by weak long-range interactions.

The fringing apparent in the figures above limits the sensitivity of the present measurements in 2 of the 4 detection channels. The origin of the fringing is not fully understood; however, it appears to have a definite phase with respect to both the heterodyne detection and the plasma modulation. When the plasma is turned off, the fringing does not appear in a scan, and if the cavity transmission detector is blocked while a signal originating from a single fringe is present on a lock-in channel, the signal vanishes. Thus, it appears that the fringing is the result of the plasma interacting with the laser light rather than a purely electronic effect. One possibility is that residual amplitude modulation (RAM) in the heterodyne sidebands is being modulated by the plasma. RAM is an imbalance in the amplitude and/or phase of the sidebands with respect to one another. When demodulated, RAM appears as a DC offset in the heterodyne signal; because of our detection scheme using velocity modulation and $2f$ detection, the NICE-OHVMS would ordinarily be insensitive to such an offset. However, if the refractive index of the plasma varies at $2f$, the DC signal from RAM will be modulated at $2f$ as well, resulting in a net NICE-OHVMS signal. Because RAM is also affected by the presence of etalons in the optical system and the optical frequency, a fringing pattern could possibly result as a function of laser frequency. Testing whether this is truly the origin of the fringing is difficult; however, it is probable that the fringing would be reduced by employing a RAM compensation scheme via temperature and voltage control of the fiber EOM. [88]

The sensitivity of the technique at the experimental detection bandwidth of 16 Hz, as determined from the noise-equivalent absorption in the baseline of the in-phase component of mixer 1 (which has the least fringing of the 4 detection channels), is 3.4×10^{-9} cm^{-1}. which is about two orders of magnitude above the shot noise limit of 3.9×10^{-11} cm^{-1} calculated from

$$\alpha_{min} = \frac{\pi}{2F}\sqrt{\frac{eB}{\eta P_0}}\frac{1}{J_0(\beta)J_1(\beta)L}, \tag{B.2}$$

where F is the cavity finesse (120), e the fundamental electric charge, B the detection bandwidth (16 Hz), η the detector responsivity, P_0 the power incident on the detector, $J_n(\beta)$ the nth order Bessel function for modulation index β (0.63), and L the cavity length (190 cm). While NICE-OHMS has been able to achieve a noise level within a factor of 2 of the shot noise limit in one implementation [114], the performance achieved

by NICE-OHVMS relative to the shot noise limit is already comparable to a number of other NICE-OHMS setups (see the extensive discussion in section 4 of [33]).

Ultimately, the absolute sensitivity can be improved by identifying and eliminating noise sources and by increasing the cavity finesse. An increase in cavity finesse leads to additional technical challenge in maintaining the laser-cavity lock, and may make the system even more susceptible to the fringing effects that have already been observed. Such challenges can likely be overcome by improving the bandwidth of the laser frequency corrections (currently limited to the 10 kHz bandwidth of the signal cavity PZT), and correcting for RAM as discussed above.

B.6 Conclusions

In this paper, we have demonstrated sub-Doppler spectroscopy of molecular ions in the mid-infrared spectral region using the NICE-OHVMS technique with a cw-OPO. By phase modulating the seed laser with a fiber EOM prior to amplification and optical parametric oscillation, the mid-infrared idler is also phase modulated without requiring a mid-IR EOM. The high optical power of the idler beam allows use of high-bandwidth detectors, which in turn make ultra-sensitive spectroscopy via NICE-OHMS possible. Velocity modulation spectroscopy is then combined with NICE-OHMS to afford ion-neutral discrimination, and the intracavity laser power is sufficient for saturating fundamental rovibrational transitions as demonstrated by spectroscopy of H_3^+. By fitting the sub-Doppler spectral features, the center frequencies of individual rovibrational lines can be measured with a precision of 70 kHz, and the maximum achieved sensitivity is within a factor of $\sim$90 of the shot noise limit. Improvements to the technique, such as addition of an optical frequency comb for accurate wavelength calibration, technical modifications to improve its sensitivity, and expanding the frequency coverage of the OPO from 3.2-3.9 μm to 2.8-4.8 μm, are envisioned.

The authors would like to thank Takeshi Oka for providing the liquid nitrogen cooled plasma cell and its associated pumps and plasma electronics. KNC and BMS acknowledge support from a NASA Earth and Space Science Fellowship. JNH acknowledges support from a Springborn Fellowship and a National Science Foundation Graduate Research Fellowship (DGE 11-44245 FLLW). This work has been supported by the National Science Foundation (PHY 08-55633), the NASA Laboratory Astrophysics program (NNX08AN82G), and a David and Lucile Packard Fellowship.

Appendix C

Broadly Tunable Mid-Infrared NICE-OHMS Spectrometer

C.1 Abstract

The sensitive spectroscopic technique noise immune cavity enhanced optical heterodyne molecular spectroscopy (NICE-OHMS) has been successfully used in a variety of systems; however, no broadly tunable setup has been developed for the mid-infrared. To this end, we have integrated a difference frequency generation (DFG) system into a NICE-OHMS setup. Initial optimization and characterization was completed with ro-vibrational spectroscopy of methane. Doppler-broadened frequency modulated-NICE-OHMS spectra were recorded at a sensitivity of 2×10^{-7} cm^{-1} Hz$^{-1/2}$. Sub-Doppler saturation signals (Lamb dips) were also observed using wavelength modulated-NICE-OHMS, achieving a sensitivity of $\sim6\times10^{-9}$ cm^{-1} Hz$^{-1/2}$.

C.2 Introduction

Noise immune cavity enhanced optical heterodyne molecular spectroscopy (NICE-OHMS) is the most sensitive direct absorption technique developed. First reported by Ye et al.[114], this technique combines the increased absorption due to path length enhancement of cavity enhanced absorption spectroscopy[27, 4] with the low noise of frequency modulation/heterodyne spectroscopy[10]. Not only does NICE-OHMS allow for high sensitivity detection, but it can also probe sub-Doppler saturation features. Rigorous theoretical analyses of the NICE-OHMS signal, both Doppler-broadened and sub-Doppler, have been reported in several works[63, 5]. Variants of NICE-OHMS setups have also been developed, such as wavelength-modulated NICE-OHMS[98] and the ion-specific velocity-modulation NICE-OHMS[90].

Additionally, NICE-OHMS has evolved through its integration with different laser systems. Nd:YAG[114], Ti:sapphire[62], laser diode[47], and fiber-laser[85, 86] based NICE-OHMS spectrometers have been built, but

This chapter was first published as: M. W. Porambo, B. M. Siller, J. M. Pearson, and B. J. McCall, "Broadly Tunable Mid-Infrared Noise-Immune Cavity-Enhanced Optical Heterodyne Molecular Spectrometer", *Optics Letters*, **37**, 4422-4424 (2012).[78]

little work has been done on NICE-OHMS in the mid-infrared (3–10 μm) spectral region. To our knowledge, the only setup reported in this wavelength range is based on a quantum cascade laser (QCL)[96]. QCLs, however, suffer from limited tunability.

Other laser systems offer broader tunability in the mid-infrared. Difference frequency generation (DFG) produces a beam at the frequency difference between two input lasers using a nonlinear crystal, with the tunability only limited by the most tunable of the lasers and the transparency of the crystal. Similarly, continuous wave optical parametric oscillators (cw OPOs) emit mid-infrared radiation tunable from ~2.3 to 4.6 μm. To extend its tunability in the mid-infrared, we have integrated NICE-OHMS with a DFG setup, enabling use of this unique, high-sensitivity spectroscopy continuously in the ~3–5 μm region.

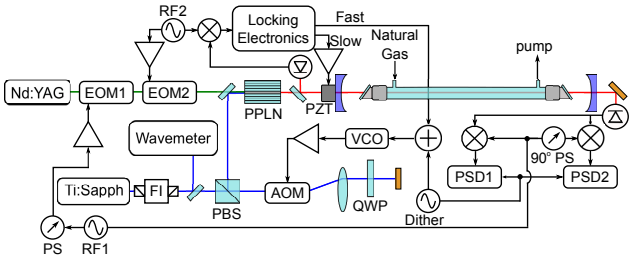

Figure C.1: Experimental Layout. FI: Faraday isolator; PBS: polarizing beam splitter; AOM: acousto optic modulator; QWP: quarter wave plate; VCO: voltage controlled oscillator; EOM: electro-optic modulator; PZT: piezoelectric transducer; RF: radio frequency generator; PS: phase shifter; PSD: phase sensitive detector; PPLN: periodically poled lithium niobate crystal; △: RF amplifier.

C.3 Experimental

The experimental setup is illustrated in Fig. C.1. A ring Ti:sapphire laser (Sirah-Matisse TS) whose wavelength is measured with a Bristol 621A-IR wavemeter is sent through a double-pass acousto-optic modulator (AOM)[24] that is resonant at ~85 MHz, which redshifts the laser by ~170 MHz and results in no change to the beam pointing upon altering the AOM driving frequency. A Nd:YAG laser (1064 nm) is passed through two electro-optic modulators (EOM). The first EOM (New Focus 4003, MgO:$LiNbO_3$) is resonant at ~112.5 MHz and generates sidebands at the cavity free spectral range (FSR) used for heterodyne detection; the modulation index is 0.79. The second EOM (ThorLabs EO-PM-NR-C1, MgO:$LiNbO_3$) produces additional sidebands at ~6 MHz, which are used to generate the error signal in a Pound-Drever-Hall locking scheme[25]. The processed error signal is split into two correction pathways. Slow corrections (up to 70 Hz) are sent to the cavity piezoelectric transducer (PZT), while fast corrections (up to 60 kHz) are sent to the voltage controlled oscillator (VCO) of the AOM. The Ti:sapphire and Nd:YAG are combined in a periodically poled lithium niobate (PPLN) crystal, which results in a mid-infrared beam at the difference between

the frequencies of the two input lasers. This beam can be tuned between 2.8 and 4.8 μm by tuning the Ti:sapphire laser frequency (for NICE-OHMS, the wavelength-dependent reflectivity of the optical cavity mirrors limits the tuning range to 3.0–3.4 μm, but multiple mirror sets could be used to extend the tunability to 2.8–4.8 μm).

The mid-IR DFG is then coupled into a cavity with a finesse of ∼300. The cavity transmission is captured on a 120 MHz bandwidth InSb detector (Kolmar). Then, the signal is split and demodulated with two RF mixers that are both referenced to the heterodyne RF frequency, but are 90° out of phase with one another to separate the absorption and dispersion signals.

The sample cell used in this work was equipped with turbomolecular pumps and operated as a flow cell. Natural gas was leaked into the cell from the building supply. Light was coupled through CaF_2 Brewster windows on either end of the cell, which was isolated from the cavity mirrors to reduce vibrational noise.

Two different modulation techniques were performed during this work. The first was frequency modulated (fm)-NICE-OHMS. The second was wavelength modulated (wm)-NICE-OHMS, in which a 50 Hz dither was applied to the AOM VCO to induce a peak-to-peak modulation of 1.7 MHz, and phase sensitive detectors (that is, lock-in amplifiers) demodulated the resulting signal.

C.4 Results and Discussion

Demonstration and characterization of the DFG NICE-OHMS system was conducted by ro-vibrational spectroscopy of methane in natural gas. The heterodyne phase was adjusted such that one mixer output would be approximately tuned to the absorption phase and the other approximately tuned to the dispersion phase. A representative Doppler-broadened spectrum of a methane ro-vibrational transition (containing the absorption and dispersion channels) is shown in Fig. C.2.

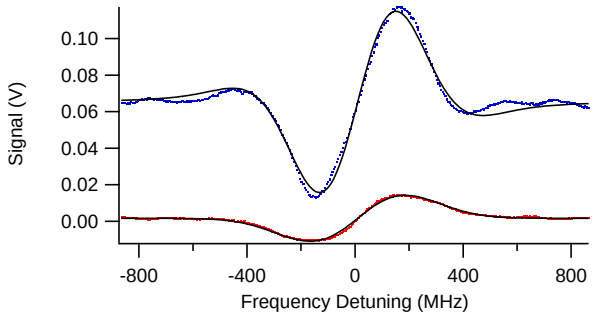

Figure C.2: Doppler-broadened fm-NICE-OHMS dispersion (top) and absorption (bottom) signals from the P(9) A_2 transition of the ν_3 fundamental band of CH_4 at a pressure of $\sim 6\times10^{-5}$ Torr. Raw data are given as dots, fits to the data are given in solid curves. The dispersion curve is offset vertically for clarity.

A fit equation based on Equation 1 of Ref. [33] was used to fit the data:

$$S = y_0 + A\Big[\left(\chi_{-1}^{abs} - \chi_1^{abs}\right)\cos\theta + \left(2\chi_0^{disp} - \chi_1^{disp} - \chi_{-1}^{disp}\right)\sin\theta\Big] \tag{C.1}$$

where

$$\chi_j^{abs} = \frac{1}{\sqrt{1+G}} e^{-x^2} \tag{C.2}$$

$$\chi_j^{disp} = \frac{2}{\sqrt{\pi}} e^{-x^2} \int_0^x e^{t^2}\,\mathrm{d}t \tag{C.3}$$

and $x = \frac{2\sqrt{\ln 2}(\Delta\nu + j\nu_m)}{\delta\nu}$. Furthermore, θ is the heterodyne detection phase, A is the amplitude, G is the saturation parameter, y_0 is an offset parameter, $\Delta\nu = \nu - \nu_0$ is the detuning of the source frequency ν from the transition line center ν_0, ν_m is the heterodyne modulation frequency, and $\delta\nu$ is the transition line width (FWHM). A global analysis fit was performed on both channels simultaneously with θ, ν_m, G, and A constrained to be equal for both detection channels and y_0 allowed to float independently. ν_m is held fixed at 112.5 MHz.

The fractional noise equivalent absorption (NEA) is calculated to be $\sim 1 \times 10^{-6}$ cm^{-1} Hz$^{-1/2}$ and $\sim 2 \times 10^{-7}$ cm^{-1} Hz$^{-1/2}$ for the dispersion and absorption detection channels, respectively. Low frequency noise is observed in the baseline, which appear to be phase-dependent; this noise is more pronounced in the dispersion channel than in the absorption channel. This noise is suspected to be from etalons in the optical setup, residual amplitude modulation due to the heterodyne EOM, or a combination of these. Both of these effects can be phase-dependent[106, 108], which may explain why one channel contains more noise. Attenuation of the absorption signal due to optical saturation is observed, consistent with published theoretical descriptions[63]. The saturation parameter was determined to be ∼70 by the global fit to the data.

Not only does this optical saturation attenuate the Doppler-broadened signal amplitude[63], but it also leads to sub-Doppler Lamb dips. The Lamb dips are the result of two modes of the phase-modulated light (a forward-propagating mode and a counter-propagating mode) interacting with the same velocity group of molecules. Lamb dips are observed in the Doppler-broadened spectrum at the line center for dispersion signals and at multiples of half the heterodyne frequency for both dispersion and absorption. As generally the center dispersion Lamb dip is the strongest of the Lamb dips, the scan parameters were varied to maximize the amplitude of this Lamb dip. Optimization of the center dispersion Lamb dip was aided by the fact that

no Lamb dip at line center should be observed in the absorption detection phase; thus, the heterodyne phase was varied until the center Lamb dip in one detection channel was completely eliminated. An optimized center dispersion Lamb dip is shown in Fig. C.3.

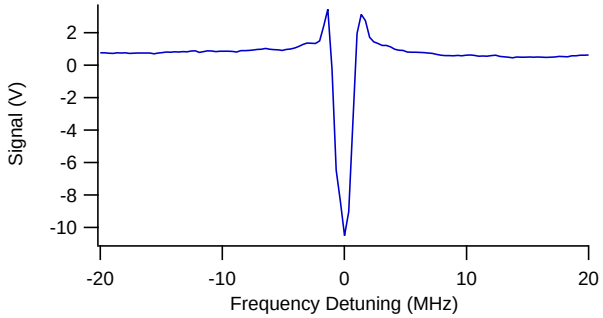

Figure C.3: Center dispersion Lamb dip of the P(12) A_1 transition of the ν_3 fundamental band of CH_4 observed at a pressure of $\sim 6\times10^{-5}$ Torr.

The sub-Doppler signals were obtained using wm-NICE-OHMS, as described earlier. Wavelength modulation broadened the sub-Doppler lineshape sufficiently to observe the signal while taking ~350 kHz steps on the DFG (by tuning the Ti:sapphire laser). This detection scheme also results in higher sensitivity than that of fm-NICE-OHMS. With wm-NICE-OHMS, the NEA is calculated to be 6×10^{-9} cm^{-1} $Hz^{-1/2}$, which is about 250 times the shot noise limit. This value is about a factor of 60 less sensitive than what was observed for the QCL-based NICE-OHMS spectrometer[96].

Several issues seem to impact the ultimate sensitivity and performance of the spectrometer. Etalons formed between the transmission detector and the optical cavity and between the optical cavity and the DFG PPLN crystal decrease the sensitivity. For the Doppler-broadened scans, these etalons were significantly mitigated by using heat guns across the respective beam paths and averaging for ~1 s per point, as accomplished in [52]. Furthermore, the lineshapes of the signals are somewhat distorted by drifts in the frequencies of the pump and signal lasers of the DFG process. To prevent this drifting in the future, we plan to stabilize the frequencies of both lasers by locking the Nd:YAG to an iodine hyperfine transition and the Ti:sapphire to an optical frequency comb.

C.5 Conclusions

In summary, we present the first broadly tunable NICE-OHMS spectrometer in the mid-infrared. Coherent mid-infrared radiation is produced through difference frequency generation with a Nd:YAG laser and a tunable Ti:sapphire laser combined in a periodically poled lithium niobate crystal. The instrument was

characterized and optimized by probing ro-vibrational transitions of methane present in natural gas. Doppler-broadened fm-NICE-OHMS absorption and dispersion signals were acquired and fit. Sub-Doppler signals were observed using wm-NICE-OHMS. We have recently integrated this DFG NICE-OHMS system to the fast ion beam spectrometer described in [69]. Additionally, our research group has completed development of a similar mid-infrared NICE-OHMS system based on a cw OPO[19]. Both of these systems will be used to study ro-vibrational spectra of molecular ions.

The authors wish to thank Craig Riccardo and Joe Puhr for their help in acquiring spectra for this study. This work has been supported by the National Science Foundation (PHY-08-55633), the NASA Laboratory Astrophysics program (NNX08AN82G), and a David and Lucile Packard Fellowship. M.W.P. has been supported by a Robert C. and Carolyn J. Springborn Fellowship from the University of Illinois.

Appendix D

Applications of NICE-OHMS to Molecular Spectroscopy

D.1 Introduction

Noise Immune Cavity Enhanced Optical Heterodyne Molecular Spectroscopy (NICE-OHMS) is the most sensitive direct absorption technique, as it combines the advantages of cavity enhancement and heterodyne detection for very long effective path lengths through samples and (typically) near shot noise limited detection. Since its first demonstration by Ye et al. [114] in 1998, it has been implemented with a variety of laser systems to study a number of different molecules to extract various information from the obtained spectra.

The technique of NICE-OHMS is discussed thoroughly in another chapter in this book, so only a brief description will be given here. A generic NICE-OHMS experimental setup is shown in Figure D.1. The two distinguishing features of NICE-OHMS are an optical cavity and heterodyne detection, with the heterodyne sidebands coupled into separate cavity modes. The optical cavity provides path length enhancement by a factor of $2 \times F/\pi$ compared to a single-pass setup, where F is the cavity finesse, which has ranged from 120 [19] to 100,000 [114] in the various NICE-OHMS implementations.

The laser is modulated at some multiple of the cavity free spectral range (FSR), effectively creating a set of heterodyne sidebands that can be coupled into separate cavity modes, as shown in Figure D.2. A second, typically weaker, set of sidebands is added to the laser frequency to enable locking of the laser frequency to the cavity length to constantly keep the carrier frequency on resonance with one of the cavity modes using the Pound-Drever-Hall method. [25] In some NICE-OHMS setups, these two sets of sidebands are also used for locking the sideband spacing to the cavity FSR using the DeVoe-Brewer method [22], to avoid frequency mismatch induced by the cavity FSR changing as its length is scanned.

The frequency modulation is typically applied using a pair of electro-optic modulators (EOM), as in [114], though both sets of sidebands can be applied by a single EOM if it is capable of simultaneously modulating

This is the draft of a chapter to appear in the book "Cavity Enhanced Spectroscopy and Sensing", edited by Peter Loock and Gianluca Gagliardi, published by Springer.

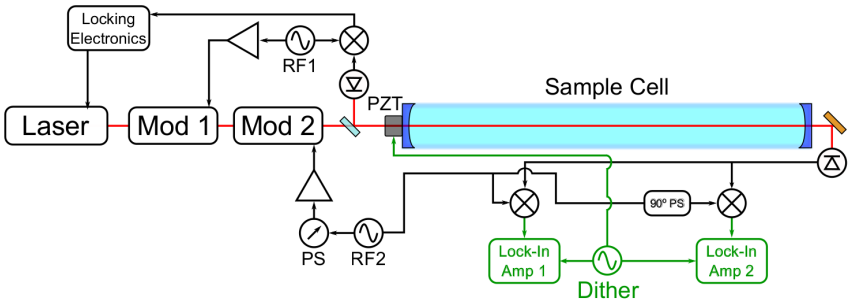

Figure D.1: A generic NICE-OHMS experimental layout. The green components are utilized only in wavelength modulated (wm-NICE-OHMS) setups. For fm-NICE-OHMS, the final experimental signals are taken directly from the mixer outputs. Alternatively, in velocity modulation setups, as described in Sections D.3.2 and D.3.2, the 'dither' is applied to the discharge voltage (not pictured here) across the cell, inducing an alternating Doppler shift of the ions within the cell.

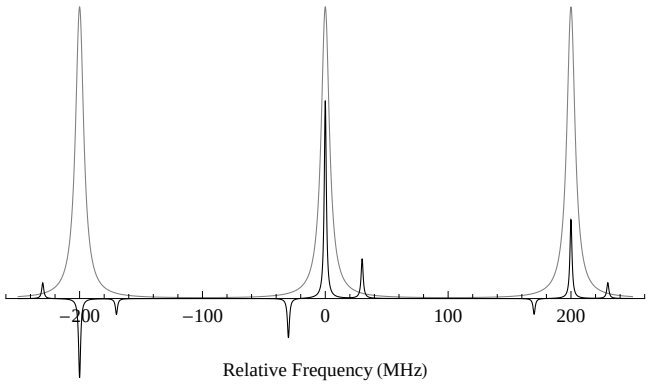

Figure D.2: The spectrum of a laser modulated for use in a NICE-OHMS setup overlaid with three optical cavity modes. Note the two sets of sidebands on the laser, in this example spaced at 30 MHz for cavity locking and 200 MHz for heterodyne detection. The second set of sidebands must be spaced at an integer multiple times the cavity FSR. They are most commonly spaced at a single FSR, but can be spaced at two [8] or even nine [90] or more times the free spectral range.

at two different frequencies with appropriate modulation depths. [85] Or, if the laser frequency can be modulated directly at sufficiently high frequencies, the modulation can be applied to the laser directly, as in [96].

D.2 Laser Systems

NICE-OHMS has been implemented with a fairly wide variety of laser systems, both in the near- and mid-infrared spectral regions.

D.2.1 Near-Infrared

To date, the vast majority of NICE-OHMS experimental setups have worked in the near-IR spectral region. Near-infrared optical components are generally less expensive, more readily available, and have better performance than the corresponding components designed for the mid-infrared, in part due to the large amount of research and development invested in the field by the telecommunications industry. Component selection is particularly important when it comes to the optical components that need to work at radio frequencies of $\gtrsim$100 MHz, namely a high-speed detector and a method of modulating the laser frequency for heterodyne spectroscopy. Dielectric coatings for cavity mirrors also tend to be better-developed and higher performing in the near-infrared than in the mid-infrared, with losses of up to an order of magnitude lower than the best mid-infrared coatings available.

One disadvantage of working in the near-IR is that no fundamental vibrational bands for molecules lie in this region, so NICE-OHMS spectrometers in this region need to observe overtones or combination bands, which tend to be much weaker than fundamental bands. Since NICE-OHMS is such a sensitive technique, these detections are still possible, but it makes the detection limit in terms of quantity of analyte required for detection significantly larger than it would be for a spectrometer of the same sensitivity observing fundamental band transitions.

Neodymium:YAG

NICE-OHMS was first demonstrated by Ye et al. with a Neodymium:YAG (Nd:YAG) laser, and this first demonstration remains to this day the most sensitive NICE-OHMS implementation yet recorded, with a detection sensitivity of 1×10^{-14} cm^{-1} Hz$^{-1/2}$. [114, 62] This extreme sensitivity was obtained through a combination of very high finesse (100,000) cavity, with a very stable, well-locked laser (down to 1 mHz relative frequency), and a sensitive detection system that allowed for an observed noise level that was within a factor of 1.4 of the shot noise limit. Although an impressive feat, not much work has been done with Nd:YAG laser systems since, primarily because they are not very widely tunable and thus can't be used to observe a very wide variety of chemical species.

Ytterbium:YAG

Ye et al. have also implemented NICE-OHMS with a Ytterbium:YAG (Yb:YAG) laser at 1030 nm. [115] The primary purpose of this work was stabilization of the laser frequency at both short and long timescales, since no precision reference existed at the Yb:YAG wavelength. To that end, a very narrow transition is needed at an absolute frequency. In this work, the R(29) transition of the $3\nu_3$ band of acetylene was used

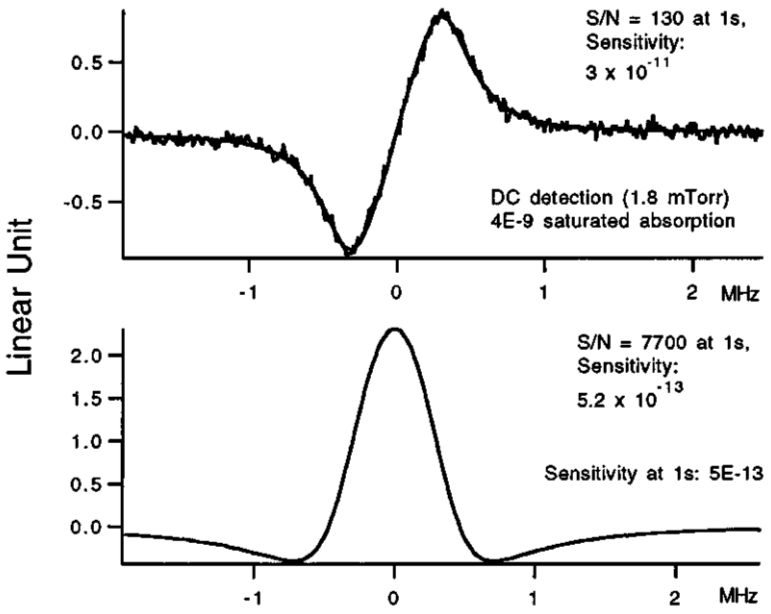

Figure D.3: The initial demonstration of NICE-OHMS by Ye et al, from Ref. [114]. Both scans were collected with wavelength-modulated detection of a Lamb dip of acetylene. The top scan is a direct DC detection of the dither signal, while the bottom utilized NICE-OHMS using the same cavity and dither. Fourteen years later, this spectrometer still retains the record for NICE-OHMS detection, with a sensitivity of 5×10^{-13}.

as the absolute frequency reference.

The Yb:YAG beam was sent through a double-pass acousto-optic modulator (AOM), which shifts the frequency of the beam by ∼160 MHz without changing the pointing of the beam as the AOM modulation frequency changes. The laser was locked to a stable optical cavity of finesse 75,000 using the Pound-Drever-Hall method. Most of the locking corrections up to 150 kHz control bandwidth were sent to the voltage-controlled oscillator (VCO) that controls the AOM frequency, while the very slow ($\lesssim$1 Hz) corrections were sent to the Yb:YAG temperature controller. Using these two controls, the absolute laser frequency was stabilized to the cavity to within ∼1 kHz relative linewidth, limited primarily by vibrations in the cavity.

For long-term stabilization against drift, a small dither was added to the cavity length, which the laser frequency followed, and a second-harmonic wm-NICE-OHMS signal of the central dispersion Lamb dip was used as an error signal, as it has antisymmetric symmetry. For optimal stabilization, the error signal should have as high a S/N and as narrow a linewidth as possible. In this work, a S/N of 900 was obtained from the sensitivity of 7×10^{-11} at 1 s averaging, and the full width at half maximum (FWHM) linewidth of the signal was ∼500 kHz, limited by a convolution of transit-time, pressure broadening, and the applied dither. The drift-correction error signal was processed and sent to the piezo-electric transducer on which one of the cavity mirrors was mounted to control the cavity length to prevent the laser frequency from drifting by any

more than ∼1 kHz over long timescales.

Titanium:Sapphire

Shortly after its initial demonstration with a Nd:YAG, NICE-OHMS was implemented with a titanium sapphire (Ti:Sapph) laser near 790 nm by Ma et al., and it's performance was directly compared to that of the Nd:YAG setup. [62] The Ti:Sapph system has the advantage of being much more broadly tunable than the Nd:YAG one, which makes it a much more versatile tool for molecular spectroscopy. Because of this versatility, several other research groups have since implemented Ti:Sapph-based NICE-OHMS spectrometers at wavelengths ranging from 730 nm to 930 nm. [32, 90]

The biggest disadvantage of the Ti:Sapph-based system compared to the Nd:YAG one is that the Ti:Sapph has a significantly broader free-running linewidth and cannot be stabilized as tightly to the optical cavity. To extend the bandwidth of the laser-cavity lock, double-pass AOMs have been used to provide a higher-frequency transducer to the system. [62, 90] To extend the bandwidth even further, a third EOM can be used with a sweeping applied voltage to change the laser frequency even faster than the AOM allows, since the EOM is not limited by the propagation time of an acoustic wave through a crystal, as an AOM is. [62] With both of these extra frequency transducers, Ma et al. were able to stabilize the Ti:Sapph laser to a cavity of finesse 17,000 to within a relative linewidth of 400 mHz. This is more than satisfactory for performing NICE-OHMS, but is still a factor of ∼300 worse than they were able to achieve with the Nd:YAG setup and cavity with 100,000 finesse.

External Cavity Diode Lasers

NICE-OHMS has also been implemented with different types of diode lasers, including external-cavity diode lasers (ECDL) and distributed feedback (DFB) diode lasers. Both of these types of diode lasers have the advantages of being relatively inexpensive and much more broadly tunable than the relatively fixed-frequency YAG-based lasers.

For example, Bell et al. build an ECDL-based NICE-OHMS spectrometer for studying the HO_2 radical (see Section D.3.2), and also used it to study CH_4 and CO_2 for diagnostic tests of their system. [8] In working with their system, they found that the sensitivity varied significantly with wavelength; they attributed this to the response of the laser varying as the wavelength was tuned, particularly with respect to the locking corrections being sent to the laser current. At 6596 cm^{-1}, where they optimized the system, they could achieve a sensitivity of 3×10^{-11} $cm^{-1}$with wm-NICE-OHMS, but tuning the laser by ∼40 cm^{-1} to the red limited their sensitivity to 2×10^{-10} cm^{-1}. This is still very sensitive in absolute terms, but is nearly an

order of magnitude worse than their optimal value; this shows that optimizing a NICE-OHMS system under a particular set of conditions does not necessarily optimize it over a broad range of conditions.

Gianfrani et al. used a similar ECDL-based setup to study molecular oxygen (see Section D.3.1). [36] One unique aspect of their setup was the way in which they locked the heterodyne frequency to the cavity FSR. Rather than using the common DeVoe-Brewer method, they applied a small dither to the RF frequency at 70 kHz, demodulated the cavity back-reflection signal at that frequency, and used the resulting signal as an error signal for locking the sideband spacing to exactly the cavity FSR with a locking bandwidth of ∼10 kHz. They also found that the locking corrections being sent to the laser injection current produced significant intensity noise, so to combat this effect, they used an AOM in another feedback loop to keep the laser power as constant as possible. They did this because while in principle, the noise-immune property of NICE-OHMS prevents laser intensity noise from contributing to the net spectroscopic signal, in practice, residual amplitude modulation (RAM) is always present, and can cause laser intensity noise to couple through the entire detection train and into the final signal. This effect of RAM often makes it worth taking the time to clean up whatever intensity noise there is, rather than relying on the noise-immune property to maximize the sensitivity of the instrument. The intensity stabilizer not only improved their sensitivity, but also allowed them to collect broad scans (up to 8 GHz wide) with very flat baselines.

Distributed Feedback Diode Lasers

NICE-OHMS has also been implemented with a distributed feedback (DFB) diode laser. [35] Compared to ECDLs, DFB lasers are more robust, since they don't rely on an external grating that is susceptible to mechanical vibrations, so they have greater potential for use in more robust spectrometers. The DFB laser used in this work has the additional advantage of having a fiber-coupled output, which makes it easier to use the fiber-coupled acousto-optic and electro-optic modulators that were used for modulation and locking. Compared to free-space components, fiber components tend to be significantly easier to align and use, and often have better performance than their free-space counterparts.

Fiber Lasers

Fiber lasers offer excellent frequency stability and mode structure, which makes them well-suited for efficient coupling into and locking to optical cavities. Since the laser is fiber-coupled to start with, and exits the fiber in free space before entering the optical cavity, the instrument designer has a choice of using either fiber or free-space components for laser frequency modulation and control. Fiber EOMs are particular attractive for NICE-OHMS since they are much more efficient (lower half-wave voltage) compared to free space EOMs

without the need for a resonant electronic circuit to amplify effective RF voltages. This allows for the laser frequency to be modulated at essentially any frequency up to several GHz with almost arbitrary depth of modulation. It is also possible to apply both of the modulation signals needed (for locking and for heterodyne detection) to a single EOM by using a simple RF combiner. Schmidt et al. demonstrated NICE-OHMS with an erbium-doped fiber laser, and observed acetylene with a sensitivity of 2.4×10^{-9} cm^{-1}, which was about a factor of 1000 above the shot noise limit. [85] In a follow-up paper in which they used a different EOM with shorter fibers and used an active temperature controller for the temperature of the EOM and fibers, they improved the sensitivity to 5×10^{-11} cm^{-1} Hz$^{-1/2}$, which is within a factor of 26 of the shot noise limit. [33]

D.2.2 Mid-Infrared

NICE-OHMS hasn't been implemented nearly as often in the mid-infrared as it has in the near-infrared, in part because high performance mid-infrared components are not very readily available, but the mid-infrared does offer the significant advantage of being the region of fundamental vibrational modes for many molecules. In the decade following the initial discovery of NICE-OHMS, only a single demonstration was done at wavelengths beyond 2 μm, which used a quantum cascade laser (QCL) at $\sim$8.5 μm. Recently, mid-infrared systems have been implemented using nonlinear processes to frequency-shift near-IR lasers into the mid-IR. This allows for all laser processing to be done on the near-IR systems, meaning the only specialized mid-IR components required are cavity mirrors with appropriate coatings and fast detectors.

Quantum Cascade Lasers

Quantum cascade lasers (QCL) offer the advantage of being available at wavelengths ranging from 3.5 to 20 μm, a range inaccessible by most laser systems. Taubman et al. demonstrated a QCL-based NICE-OHMS spectrometer at $\sim$8.5 μm with a sensitivity of 9.7×10^{-11} cm^{-1} Hz$^{-1/2}$. [96] They had two major difficulties in setting up this system: modulating the QCL, and detecting the resulting heterodyne beat signal, both of which typically need to operate with bandwidths of hundreds of MHz.

Frequency modulating the QCL was accomplished by modulating its injection current. They found that the modulation efficiency fell proportional to $1/f$, where f is the modulation frequency, up to $\sim$100 MHz, and dropped proportional to $1/f^2$ above 100 MHz. They did, however find a resonance in their QCL at 387.5 MHz where the modulation efficiency was significantly higher than nearby frequencies, so they chose this as their heterodyne frequency and designed their optical cavity length to match. They didn't offer a physical explanation for the resonance, but note that resonant frequencies vary between different lasers,

even for lasers on the same chip. In this paper is also described a scheme for modulating a QCL with an injection-locking scheme using two lasers, a master and a slave, and they showed that this method reduced the observed RAM level by 49 dB compared to the current modulation scheme that was used for spectroscopy. Although this modulation scheme has not yet been used in a NICE-OHMS system, it is promising for future work.

The other challenge they faced was finding and characterizing a detector fast enough for optimal heterodyne detection. They used a mercury-cadmium-telluride (MCT) detector, and to determine its frequency response, they used two separate QCLs, tuned them to slightly different frequencies, and combined them onto the detector element. This gave them a heterodyne beat that should have constant amplitude over the ∼800 MHz that they tuned the frequency difference. By recording the detector output signal versus the heterodyne frequency, they found that the net detector signal at 387 MHz was attenuated by 35 dB compared to the DC response, and they attribute this detector inefficiency as the reason for their detection sensitivity being an order of magnitude above the shot noise limit.

One of the limitations of working with QCL systems is the limited tunability, which can be anywhere from ∼20 cm^{-1} (for stand-alone QCL systems such as the one used for NICE-OHMS) to ∼200 cm^{-1} (for external-cavity systems).

Difference Frequency Generation

Recently, NICE-OHMS has been implemented with a broadly tunable mid-IR source through difference frequency generation (DFG). [78] The DFG process works by combining two lasers within a nonlinear material to produce a beam whose frequency is the difference of the two input lasers' frequencies. This experimental setup was based around a fixed-frequency Nd:YAG laser and a tunable Ti:Sapph laser, which were combined in a periodically poled lithium niobate (PPLN) crystal. Because near-IR components typically have better performance, lower prices, and are more readily available than their mid-IR counterparts, all laser frequency control was done on the near-IR pump lasers before generating the mid-IR DFG, so the only mid-IR specific components that were needed were the detectors for cavity transmission and back-reflection, and the cavity mirrors, which were specified for the 3.0-3.4 μm range. The 2.8-4.8 μm tuning range of the laser system, limited by the poling periods of the PPLN crystal, is a particularly attractive range for fundamental vibrational modes of many molecules.

To minimize the effects of frequency-dependent RAM and etalon effects on the ultimate signal from the instrument, the two EOMs were both placed on the fixed-frequency Nd:YAG rather than the tunable Ti:Sapph. The system remains sensitive to any etalons on the mid-IR beam after the PPLN crystal, but it

is insensitive to those effects on either of the two near-IR beams.

This DFG system was used to acquire spectra of methane with both fm- and wm-NICE-OHMS. The fm-NICE-OHMS setup was used to acquire Doppler-broadened scans, and its sensitivity of 2×10^{-7} cm^{-1} Hz$^{-1/2}$ was limited primarily by etalons in the mid-IR beam path, particularly between the PPLN crystal and the cavity input mirror and between the cavity output mirror and the detector. In the wm-NICE-OHMS setup, a 50 Hz dither was added with a 1.7 MHz peak-to-peak modulation to observe just the sub-Doppler features of methane. In this configuration, the sensitivity was over an order of magnitude better: 6×10^{-9} cm^{-1} Hz$^{-1/2}$, approximately a factor of 60 above the shot noise limit.

Optical Parametric Oscillators

Recently, NICE-OHMS has also been implemented with an optical parametric oscillator (OPO), which relies on a nonlinear process similar to that used in the DFG system. [19] A 1064 nm ytterbium-doped fiber laser is used as the seed. This beam is passed through a fiber EOM that applies both the locking and heterodyne sidebands before the beam is sent to a fiber amplifier, which amplifies the total laser power to ∼10 W to be used as the pump of the OPO.

The OPO consists of a fan PPLN, which enables continuous tuning of the poling periods across its range by translating the crystal, and a singly resonant cavity, that is resonant with just the signal beam of the OPO. The signal is tunable from 1.5-1.6 μm, while the idler is tunable from 3.2-3.9 μm. Because the locking and heterodyne sidebands on the pump beam are not spaced at an exact multiple of the FSR of the OPO signal cavity, the signal beam remains a single frequency. Due to conservation of energy, this means that the sidebands get transferred entirely to the idler beam.

The NICE-OHMS cavity used in this work had a fairly low finesse, ∼120, but with the idler power of ∼1 W, there was more than enough intracavity power to enable sub-Doppler spectroscopy of molecular ions. Velocity modulation was coupled with NICE-OHMS in a technique referred to as noise immune cavity enhanced optical heterodyne velocity modulation spectroscopy (NICE-OHVMS). Not only does velocity modulation help to combat some of the difficulties associated with DC detection (e.g. RAM and etalons), but it also affords discrimination of ionic signals from neutral ones through phase sensitive detection. After RF demodulation to separate absorption from dispersion followed by a second level of demodulation at twice the plasma drive frequency, a total of four data channels were collected simultaneously. There was some significant fringing in the signals from three of the detection channels, and the quietest of the channels exhibited a sensitivity of 3.9×10^{-9} cm^{-1}.

D.3 Molecules

Several different molecules have been observed with the NICE-OHMS spectrometers described Section D.2. Many of these have been chosen to demonstrate and optimize spectrometers because they have bands that coincide with the spectral coverage of the laser systems used, while others were observed based on scientific interest and NICE-OHMS was the technique of choice due to its sensitivity and resolution. This section is intended to give an overview of the molecules observed with NICE-OHMS to date, briefly mentioning the molecules that were used as tests to demonstrate the capabilities of instruments, while discussing more in depth the studies from which new molecular information was extracted from NICE-OHMS spectra.

D.3.1 Closed-Shell Neutral Molecules

The vast majority of NICE-OHMS papers that have been published to date have demonstrated the detection of closed-shell neutral molecules. Typically, these spectrometers have a static sample cell, often made of Invar, Zerodur, or some other material with a low coefficient of thermal expansion, with the cavity mirrors permanently affixed to the cell, and one mirror mounted on a piezo-electric transducer.

Acetylene (C_2H_2)

For many of the papers whose primary purpose was to demonstrate the technique of NICE-OHMS and to characterize and optimize the various aspects of the technique, acetylene and its isotopologues have been favorite targets. [114, 86, 13, 63, 85] Several vibrational combination bands have been observed at wavelengths ranging from 730 nm to 1530 nm.

Methane (CH_4)

Bell et al. observed an unassigned methane transition at 6610.06 cm^{-1}as a diagnostic of their NICE-OHMS spectrometer described in Section D.3.2, recording the pressure broadening in helium to verify the linearity of their spectrometer. [8] Their pressure-broadening coefficient of 1.5±0.1 MHz/Torr (HWHM) agreed well with the literature values for the $2\nu_3$ band of methane at 1.65 μm.

Ishibashi et al. observed several lines of the $2\nu_3$ band of methane with their ECDL-based wm-NICE-OHMS spectrometer with sub-Doppler resolution. [47] They also observed several lines of $^{13}CH_4$, and used their acquired spectra to determine that their sensitivity was 9.5×10^{-11} cm^{-1}, which is within a factor of 2.6 of the shot noise limit, and that their spectral resolution was 320 kHz, limited primarily by transit time, but with a small contribution from residual frequency noise in the system.

Porambo et al. used methane to demonstrate the capabilities of their DFG-based NICE-OHMS spectrometer. [78] They performed both Doppler broadened scans with fm-NICE-OHMS, and sub-Doppler scans with wm-NICE-OHMS. They observed several transitions of the ν_3 fundamental band of CH_4, and found that they could obtain a sensitivity of $\sim 6 \times 10^{-9}$ cm^{-1} Hz$^{-1/2}$.

Methyl Iodide (CH_3I)

Ishibashi et al. also used their ECDL-based NICE-OHMS setup to observe the $2\nu_4$ band of CH_3I centered around 1.65 μm. [48] They observed a total of 56 rovibrational transitions from the P, Q, and R branches with $\sim$1 MHz resolution. This allowed them to achieve full resolution of the electric quadrupole hyperfine components for the P and R branch lines, while the Q branch hyperfine components were partially blended. Because the hyperfine splitting pattern differs for different spectral lines, they found that hyperfine resolution was useful for assigning their acquired spectra.

Nitric Oxide (NO)

Bood et al. studied the sixth overtone band of nitric oxide near 797 nm in order to determine its transition dipole moment. [13] This high overtone band is too weak for most direct absorption techniques, which is why NICE-OHMS was chosen. They observed a total of 15 rovibrational transitions of the $2\Pi_{1/2} - 2\Pi_{1/2}$ sub-band of this vibrational band at a pressure of 75 Torr, and from their data, they extracted absolute intensities of individual lines, the vibrational transition dipole moment, and Herman-Wallis coefficients. Comparing the transition dipole moment of 3.09 μD for this band to the lower overtone bands indicated a significant influence from anharmonicity at the ν=7 vibrational level. They also parametrized the electric dipole moment of NO for bond lengths ranging between 0.91 and 1.74 Å more accurately than had previously been done.

Molecular Oxygen (O_2)

Gianfrani et al. used an ECDL and a cavity of finesse 6,000 to perform NICE-OHMS of molecular oxygen with a sensitivity of 6.9×10^{-11} cm^{-1} Hz$^{-1/2}$, a factor of 30 above the shot noise limit. [36] They studied weak magnetic-dipole transitions of the $b^1\Sigma_g^+(\nu'=0) \leftarrow X^3\Sigma_g^-(\nu''=0)$ band near 762 nm. They started by characterizing their spectrometer in both fm- and wm-NICE-OHMS modes of operation using the ^{P}Q(13) line of $^{16}O_2$ with 50 mTorr of pressure, looking at both lineshapes and sensitivity compared to direct CEAS detection.

They then went on to look for the $^{16}O_2$ ^{P}P(12) forbidden transition. As a consequence of the sym-

metrization postulate of quantum mechanics, transitions starting from even rotational quantum numbers are forbidden, so they used their NICE-OHMS spectrometer to look for one of these forbidden transitions as a test of this postulate. They saw no trace of a signal at up to 200 Torr of pressure, so based on their calculated sensitivity, they could set the upper limit on the violation of the symmetrization postulate for O_2 at 5×10^{-8}, which is about an order of magnitude lower than the previous upper limit.

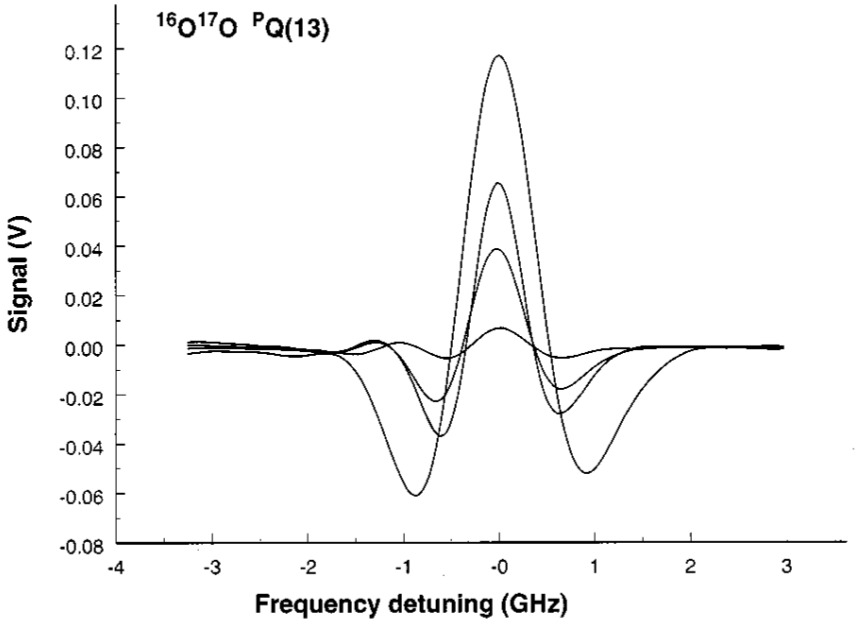

Figure D.4: NICE-OHMS signal from Gianfrani et al. [36] of the $^{P}Q(13)$ line of $^{16}O^{17}O$ in its natural abundance (0.037%) at 764.489 nm for four different pressures ranging from 660 to 1.3×10^4 Pa.

They also observed some weak lines of $^{16}O^{18}O$ and $^{16}O^{17}O$ in their natural abundances (0.2% and 0.037%, respectively), and noted some nonlinearity with pressure that they attributed to two factors: the onset of pressure broadening at higher pressures, and the decreasing modulation depth of their constant-amplitude dither as linewidths broadened at higher pressures.

Nitrous Oxide (N_2O)

Taubman et al. characterized their QCL-based NICE-OHMS spectrometer with a nitrous oxide line at 1174.9515 cm^{-1}. [96] They used the observed spectra to determine that their experimental sensitivity was 9.72×10^{-11} cm^{-1} $Hz^{-1/2}$, and compared the obtained NICE-OHMS signals to those obtained with CEAS, showing the drastic noise reduction enabled by the technique.

Bell et al. performed spectroscopy of the R28(e) transition of the ν_3 band of N_2O as another diagnostic of their spectrometer described in Section D.3.2. [8] They found the pressure-broadening coefficient of

2.2±0.1 MHz to be in good agreement for the literature value of the P(26) transition of the same band, and furthermore verified the linearity of their detection system, as indicated by the linear fit of the linewidth versus pressure plot.

Carbon Dioxide (CO_2)

Bell et al. also performed spectroscopy on the $\nu_1+\nu_2+2\nu_3$ band of carbon dioxide at 6646.58 cm^{-1} as a diagnostic test of their ECDL-based NICE-OHMS spectrometer whose primary purpose was spectroscopy of HO_2 radical (see Section D.3.2). They achieved a sensitivity of 2×10^{-10} cm^{-1}in 10 s of averaging, which was two orders of magnitude more sensitive than their CEAS setup with the same cavity.

D.3.2 Radicals and Ions

More recently, NICE-OHMS has been used to observe HO_2, N_2^+, and H_3^+. The sensitivity of NICE-OHMS is very well suited to detection of these species, since under the conditions used to generate these species, radicals and ions are often orders of magnitude less abundant than their precursor molecules.

Hydroperoxyl Radical (HO_2)

The HO_2 radical, which is of interest to atmospheric chemistry, has recently been studied using NICE-OHMS by Bell et al. [8] NICE-OHMS was chosen as the optimal technique due to its species-specific detection (as opposed to some other indirect techniques that have been used for this molecule), its capability of extracting absolute number densities from spectra, and its extremely high sensitivity. The first vibrational overtone of the OH stretch ($2\nu_1$) band, centered at 6649 cm^{-1}, was studied in this work, as it falls within the range of the ECDL used (1480-1540 nm).

Both fm- and wm-NICE-OHMS were performed. Heterodyne sidebands were spaced at ∼219 MHz, twice the ring cavity's FSR, and this frequency was locked using the DeVoe-Brewer method. For the wavelength-modulated work, a 60 Hz dither was applied to one of the cavity mirrors to induce a frequency dither with 100 MHz amplitude. By performing cavity-enhanced absorption spectroscopy (CEAS) of a known transition of methane at 6595.90 cm^{-1}within their spectrometer, the authors determined that their cavity finesse was 2100±100.

Within the vacuum chamber, 2 cm above the ring cavity, five UV lamps were used for photolysis of Cl_2. The generated Cl atoms then reacted with methanol to form CH_2OH, which then reacted with O_2 to form HO_2 and formaldehyde. The authors performed a detailed chemical analysis of all reactions to take place within the chamber to predict the abundance of HO_2 as well as that of any potentially interfering species.

Two transitions of the first vibrational overtone of the OH stretch ($2\nu_1$) were studied: the $^qP_1(12)$ transition at 6623.32 cm^{-1}, and the $^qP_2(10)$ transition at 6623.57 cm^{-1}. fm-NICE-OHMS was performed, and background scans were collected and subtracted by turning off the UV lamps for ∼10 s and repeating the scans. A sensitivity of 1.8×10^{-9} cm^{-1}was achieved, which corresponded to a minimum detectable concentration of $\sim 4 \times 10^{10}$ radicals/cm^3.

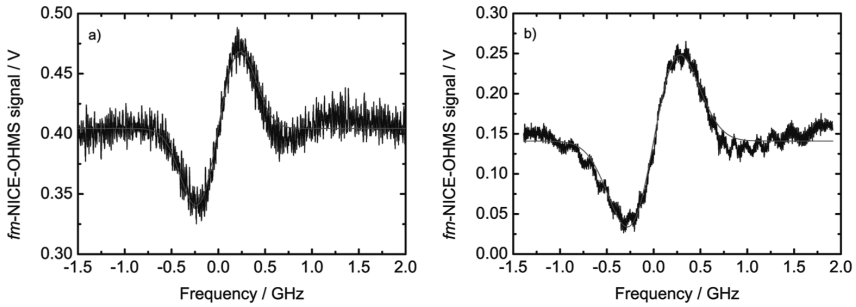

Figure D.5: fm-NICE-OHMS spectra of HO_2 with fits from Bell et al. [8] (a) $^qP_1(12)$ transition at 6623.32 cm^{-1}(b) $^qP_2(10)$ transition at 6623.57 cm^{-1}.

Kinetic studies were performed by turning off either the chlorine gas flow or the UV lamps, and observing the rate at which the observed signal decayed. The observed signal loss rate combined with kinetic modeling provided further evidence that the observed lines were, in fact, from the HO_2 radical and not some other species in the sample cell. The authors also used the decay rate to estimate the rate at which HO_2 is broken down by the walls of the chamber.

Molecular Nitrogen Cation (N_2^+)

N_2^+ has recently been studied with NICE-OHMS in both positive column [90] and ion beam [69] experiments. Both of these experiments relied on the same Ti:Sapph laser system, and because the cavity mirrors were physically separated from the sample cells, the positive column cell and the ion beam chamber could be moved in and out of the cavity without the need for a full optical realignment.

The cavity in both experiments had a finesse of ∼300 and a free spectral range of ∼113 MHz, and both experiments observed several transitions in the $\nu = 1 \leftarrow 0$ band of the Meinel system ($A^2\Pi_u$-$X^2\Sigma_u^+$) of N_2^+. Both also used a form of velocity modulation in addition to the usual NICE-OHMS heterodyne modulation.

In the positive column work, a plasma discharge cell was placed within the cavity, and light was coupled through Brewster windows mounted on either side of the cell. Two different heterodyne configurations were used: one with sidebands spaced at 1.02 GHz, 9 times the cavity free spectral range, and the other with sidebands spaced at 113 MHz, a single cavity free spectral range.

The plasma discharge voltage was modulated at 40 kHz, and the net signal was demodulated at twice that frequency to extract both the velocity- and concentration-modulated components of the ion signals, and the concentration-modulated signals of any excited neutral species. The 9-FSR setup was used to collect wide Doppler broadened scans of N_2^+ and N_2^* (an electronically excited state of neutral N_2), while the 1-FSR setup was used to primarily to collect scans of the sub-Doppler features at the center of the N_2^+ lineshapes. The Lamb dips were found to have much steeper pressure broadening (∼8 MHz/Torr) than that of typical neutral molecules, as well as an extrapolated zero-pressure linewidth of ∼32 MHz, which isn't fully understood at this point.

Sub-Doppler scans were calibrated with an optical frequency comb, and with the extreme absolute accuracy afforded by comb calibration and the precision afforded by sub-Doppler resolution, line centers were determined with an absolute accuracy of ∼300 kHz, which is approximately two orders of magnitude more precise than traditional Doppler-broadened, wavemeter-calibrated velocity modulation spectroscopy.

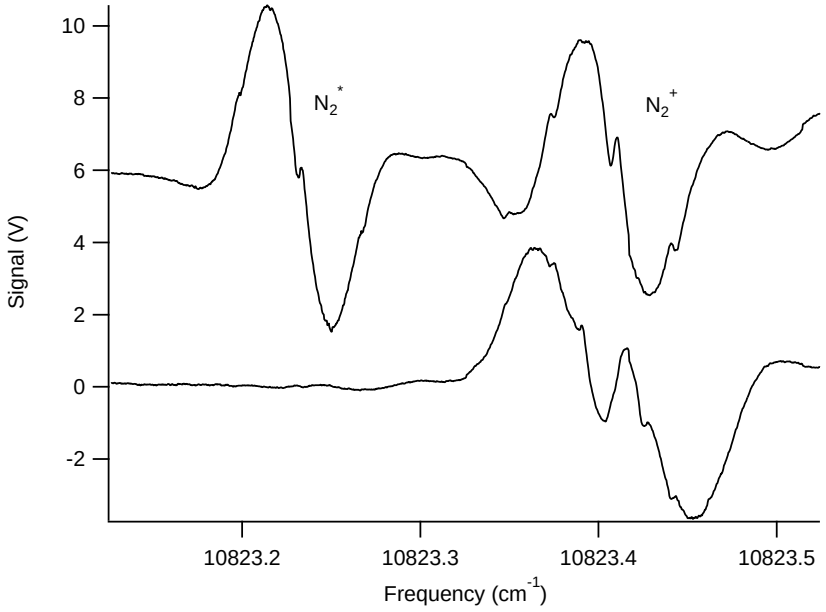

Figure D.6: A signal from the NICE-OHVMS system with a nitrogen plasma. The two traces are from the X and Y outputs of the lock-in amplifier. For this scan, the heterodyne sidebands were spaced at ∼1 GHz, so Lamb dips are spaced at ∼500 MHz on top of the Doppler profiles. Two spectral lines are shown, one from N_2^+ that is both concentration- and velocity-modulated, and the other from N_2^* that is just concentration-modulated. The RF detection phase was tuned to show primarily the dispersion signal, as evidenced by the strong central Lamb dips, and the plasma detection phase was tuned to isolate all of the N_2^* signal in a single detection phase.

For the ion beam work, the plasma discharge cell was removed from the optical cavity, and was replaced by a large vacuum chamber containing the ion beam and its associated ion optics. To avoid vibrations from the turbo pumps coupling into the cavity mirrors (and thus making locking more difficult), the ion beam

chamber was mechanically separated from the optical setup, resting directly on the lab floor while all of the optics, including the cavity mirrors, were mounted on a floated optics table. Again, light was coupled through Brewster windows that were mounted on the sides of the chamber, and the ion beam within the chamber was made collinear with the intracavity laser beam by moving the chamber (for coarse control) and steering the ion beam by tuning voltages on the various ion optics (for fine control).

The ions were extracted from the source and accelerated through a 3.8 kV potential drop before being steered through a metal tube along the collinearity path of the ion and laser beams. Velocity modulation was accomplished by applying a 4 kHz 2 V peak-to-peak square wave voltage to the metal drift tube. The NICE-OHMS signal was then demodulated at this modulation frequency to extract the ion signal. Because the modulation voltage required in this setup was quite small, very little electrical interference was introduced by it, as opposed to the positive column cell that used kV-level modulation voltages. Also, the modulation is completely independent of the laser, unlike wm-NICE-OHMS, which can still be somewhat sensitive to RAM and etalons. This allowed this spectrometer to obtain a noise-equivalent absorption of $\sim 2 \times 10^{-11}$ cm^{-1} Hz$^{-1/2}$, within a factor of 1.5 of the shot noise limit.

The lines observed by this instrument are Doppler-shifted by $\sim$6 cm^{-1} from their rest frequencies, and the linewidths obtained are narrowed through kinematic compression to $\sim$120 MHz, which was limited by the beam energy spread of the ions extracted from the source into the beam. With frequency comb calibration, transition rest frequencies were determined to within $\sim$8 MHz of those determined by the NICE-OHVMS work [90], which measured transition rest frequencies directly. The accuracy was limited by the asymmetry observed in the lineshapes, which is thought to be cause by imperfect alignment of the two beams and the beam energy stability over time.

Trihydrogen Cation (H_3^+)

The technique of NICE-OHVMS, which combines NICE-OHMS with velocity modulation spectroscopy within a positive column discharge cell, has been extended into the mid-infrared using an OPO, as described in Section D.2.2, and its capabilities were demonstrated by observing H_3^+ in a liquid nitrogen cooled discharge cell, which lowered the rotational temperature of the ions to $\sim$300 K, compared to the 600-700 K temperatures that are typical for air-cooled cells. [19]

Like the N_2^+ work, the detector signal was demodulated twice, first at the heterodyne frequency with two RF mixers, then at twice the plasma frequency using a pair of dual-channel lock-in amplifiers. Since the technique of NICE-OHVMS is sensitive to both concentration and velocity modulated signals, all four detection channels had some signal, and these signals were not completely separable from one another. This

makes fitting the Doppler profiles of the acquired signals difficult, so it was not attempted in this work.

Because Lamb dips probe only the zero-velocity population, velocity modulation of the overall ion population does not have the same effect on the signal as it does for the Doppler profile. Rather, the zero-velocity population increases and decreases throughout the cycles of the plasma discharge, so both velocity- and concentration-modulated signals appear as concentration modulation when just the zero-velocity population of the ions is considered.

Both the R(1,0) and R(1,1)^u lines of H_3^+, which are separated by $\sim$0.3 cm^{-1}, were collected in a continuous scan. The overall continuous tuning range of this system is $\sim$8 cm^{-1}, limited by the tuning range of the fiber seed laser, and the overall wavelength coverage of the OPO system is 3.2-3.9 μm, though with additional OPO modules, the tuning range could be extended to 2.2-4.6 μm, limited by the transparency of lithium niobate.

Finer resolution scans were collected of just the R(1,0) line, and the four data channels acquired from each scan were fit simultaneously to find a linecenter. Although the accuracy of linecenter determination was limited to $\sim$100 MHz by the wavemeter calibration, the precision of the fit was found to be $\sim$70 kHz, which represents the ultimate limit that could be obtained if one were to calibrate the spectra with a more accurate method, e.g. with an optical frequency comb. The Lamb dips were found to each be $\sim$110 MHz wide (FWHM), so each individual Lamb dip was not resolvable, since the Lamb dips are spaced by FSR/2, $\sim$40 MHz.

D.4 Future Prospects

Even though NICE-OHMS has been implemented by a number of research groups over the past 13 years, we have still only begun to scratch the surface of what NICE-OHMS makes possible. The recent developments extending NICE-OHMS into the mid-infrared hold promise to enable the detection of strong fundamental bands of a greater variety of molecules. There has also been a good deal of work attempting to make NICE-OHMS a more robust technique, one that has the potential in being deployed in more robust instruments to observe trace gases in a wider variety of environments rather than being confined to a laboratory setting.

References

[1] Florian Adler, Kevin C. Cossel, Michael J. Thorpe, Ingmar Hartl, Martin E. Fermann, and Jun Ye. Phase-stabilized, 1.5 w frequency comb at 2.8–4.8 μm. *Opt. Lett.*, 34(9):1330–1332, 2009.

[2] Takayoshi Amano. The ν_1 fundamental band of HCO^+ by difference frequency laser spectroscopy. *J. Chem. Phys.*, 79(7):3595, 1983.

[3] D. T. Anderson, S. Davis, T. S. Zwier, and D. J. Nesbitt. An intense slit discharge source of jet-cooled molecular ions and radicals (T-rot<30k). *Chem. Phys. Lett.*, 258(1-2):207–212, August 1996.

[4] K. Anzai, X. M. Gao, H. Sasada, and N. Yoshida. Narrow lamb dip of 3.4 μm band transition of methane with difference frequency generation and enhancement cavity. *Japanese Journal of Applied Physics Part 1-regular Papers Brief Communications & Review Papers*, 45(4A):2771–2775, April 2006.

[5] Ove Axner, Weiguang Ma, and Aleksandra Foltynowicz. Sub-doppler dispersion and noise-immune cavity-enhanced optical heterodyne molecular spectroscopy revised. *J. Opt. Soc. Am. B: Opt. Phys.*, 25(7):1166–1177, July 2008.

[6] J. M. B. Bakker. Beam-modulated time-of-flight mass-spectrometer .1. theoretical considerations. *Journal of Physics E-scientific Instruments*, 6(8):785–789, 1973.

[7] J. M. B. Bakker. Beam-modulated time-of-flight mass-spectrometer .2. experimental work. *Journal of Physics E-scientific Instruments*, 7(5):364–368, 1974.

[8] Claire L. Bell, Jean-Pierre H. van Helden, Tom P. J. Blaikie, Gus Hancock, Nicola J. van Leeuwen, Robert Peverall, and Grant A. D. Ritchie. Noise-immune cavity-enhanced optical heterodyne detection of HO_2 in the near-infrared range. *J. Phys. Chem. A*, 116(21):5090–5099, May 2012.

[9] W. Benesch, D. Rivers, and J. Moore. High-resolution spectrum of the N_2^+ Meinel system to 11250 å. *J. Opt. Soc. Am.*, 70(7):792–799, 1980.

[10] G.C. Bjorklund, M.D. Levenson, W. Lenth, and C. Ortiz. Frequency modulation (FM) spectroscopy. *Appl. Phys. B*, 32:145–152, 1983.

[11] E. D. Black. An introduction to pound-drever-hall laser frequency stabilization. *Am. J. Phys.*, 69(1):79–87, January 2001.

[12] G. A. Blake, K. B. Laughlin, R. C. Cohen, K. L. Busarow, and R. J. Saykally. Laboratory measurement of the pure rotational spectrum of vibrationally excited HCO^+ ($\nu_2 = 1$) by far-infrared laser sideband spectroscopy. *Astrophys. J.*, 316:L45–L48, May 1987.

[13] Joakim Bood, Andrew McIlroy, and David L. Osborn. Measurement of the sixth overtone band of nitric oxide, and its dipole moment function, using cavity-enhanced frequency modulation spectroscopy. *J. Chem. Phys.*, 124(8):084311, 2006.

[14] S. Borri, S. Bartalini, I. Galli, P. Cancio, G. Giusfredi, D. Mazzotti, A. Castrillo, L. Gianfrani, and P. De Natale. Lamb-dip-locked quantum cascade laser for comb-referenced ir absolute frequency measurements. *Opt. Express*, 16(15):11637–11646, July 2008.

[15] D Buhl and L E Snyder. Unidentified interstellar microwave line. *Nat.*, 228(5268):267–9, October 1970.

[16] Gabriele Cazzoli, Lino Cludi, Giovanni Buffa, and Cristina Puzzarini. Precise THz measurements of HCO^+, N_2H^+, and CF^+ for astrophysical observations. *Astrophys. J. Sup.*, 203(1):11, November 2012.

[17] J. V. Coe, J. C. Owrutsky, E. R. Keim, N. V. Agman, D. C. Hovde, and R. J. Saykally. Sub-doppler direct infrared laser absorption spectroscopy in fast ion beams: The fluorine hyperfine structure of HF^+. *J. Chem. Phys.*, 90(8):3893–3902, 1989.

[18] K. N. Crabtree, C. A. Kauffman, and B. J. McCall. Note: A modular and robust continuous supersonic expansion discharge source. *Rev. Sci. Instrum.*, 81(8):086103, August 2010.

[19] Kyle N. Crabtree, James N. Hodges, Brian M. Siller, Adam J. Perry, Joseph E. Kelly, Paul A. Jenkins II, and Benjamin J. McCall. Sub-doppler mid-infrared spectroscopy of molecular ions. *Chem. Phys. Lett.*, 551(0):1 – 6, 2012.

[20] D. T. Cramb, A. G. Adam, D. M. Steunenberg, A. J. Merer, and M. C. L. Gerry. Electronic absorption-spectroscopy of N_2^+ using velocity modulation - rotational structure in the (6, 1) and (13, 6) vibrational bands of the A-X system. *J. Mol. Spectrosc.*, 141(2):281–289, June 1990.

[21] S. Davis, M. Farnik, D. Uy, and D. J. Nesbitt. Concentration modulation spectroscopy with a pulsed slit supersonic discharge expansion source. *Chem. Phys. Lett.*, 344(1-2):23–30, August 2001.

[22] R. G. DeVoe and R. G. Brewer. Laser-frequency division and stabilization. *Phys. Rev. A*, 30:2827–2829, Nov 1984.

[23] Thomas A. Dixon and R. Claude Woods. Microwave absorption spectrum of the CO^+ ion. *Phys. Rev. Lett.*, 34:61–63, Jan 1975.

[24] E. A. Donley, T. P. Heavner, F. Levi, M. O. Tataw, and S. R. Jefferts. Double-pass acousto-optic modulator system. *Rev. Sci. Instrum.*, 76(6):063112, June 2005.

[25] R. W. P. Drever, J. L. Hall, F. V. Kowalski, J. Hough, G. M. Ford, A. J. Munley, and H. Ward. Laser phase and frequency stabilization using an optical resonator. *Appl. Phys. B: Lasers Opt.*, 31:97–105, 1983. 10.1007/BF00702605.

[26] Chuanxi Duan, Rui Zheng, Song Li, Ruibo Wang, and Guangming. Huang. Infrared laser spectroscopy of the ν_2 fundamental band of D_2O^+. *J. Mol. Spectrosc.*, 251(1-2):22–26, 2008.

[27] Richard Engeln, Giel Berden, Rudy Peeters, and Gerard Meijer. Cavity enhanced absorption and cavity enhanced magnetic rotation spectroscopy. *Rev. Sci. Instrum.*, 69(11):3763–3769, 1998.

[28] Wai Yip Fan and Peter A. Hamilton. Velocity and magnetic modulation methods applied to emission spectroscopy. *Chem. Phys. Lett.*, 230(6):555 – 560, 1994.

[29] J. W. Farley. Theory of the resonance line-shape in velocity-modulation spectroscopy. *J. Chem. Phys.*, 95(8):5590–5602, October 1991.

[30] D. W. Ferguson, K. N. Rao, P. A. Martin, and G. Guelachvili. High-resolution infrared fourier-transform emission-spectra of the $^{14}N_2^+$ Meinel system - $A^2\Pi_u$-$X^2\Sigma_g^+$. *J. Mol. Spectrosc.*, 153(1-2):599–609, May 1992.

[31] E. E. Ferguson and F. Arnold. Ion chemistry of the stratosphere. *Acc. Chem. Res.*, 14(11):327–334, 1981.

[32] A. Foltynowicz, F. M. Schmidt, W. Ma, and O. Axner. Noise-immune cavity-enhanced optical heterodyne molecular spectroscopy: Current status and future potential. *Appl. Phys. B: Lasers Opt.*, 92(3):313–326, September 2008.

[33] Aleksandra Foltynowicz, Weiguang Ma, and Ove. Axner. Characterization of fiber-laser-based sub-doppler nice-ohms for quantitative trace gas detection. *Opt. Express*, 16(19):14689–14702, 2008.

[34] Aleksandra Foltynowicz, Weiguang Ma, Florian M. Schmidt, and Ove Axner. Doppler-broadened noise-immune cavity-enhanced optical heterodyne molecular spectrometry signals from optically saturated transitions under low pressure conditions. *J. Opt. Soc. Am. B: Opt. Phys.*, 25(7):1156–1165, July 2008.

[35] Aleksandra Foltynowicz, Junyang Wang, Patrick Ehlers, and Ove Axner. Distributed-feedback-laser-based nice-ohms in the pressure-broadened regime. *Opt. Express*, 18(18):18580–18591, August 2010.

[36] Livio Gianfrani, Richard W. Fox, and Leo Hollberg. Cavity-enhanced absorption spectroscopy of molecular oxygen. *J. Opt. Soc. Am. B: Opt. Phys.*, 16(12):2247–2254, Dec 1999.

[37] F. R. Gilmore, R. R. Laher, and P. J. Espy. Franck-condon factors, r-centroids, electronic-transition moments, and einstein coefficients for many nitrogen and oxygen band systems. *J. Phys. Chem. Ref. Data*, 21(5):1005–1107, September 1992.

[38] J. L. Gottfried, B. J. McCall, and T. Oka. Near-infrared spectroscopy of H_3^+ above the barrier to linearity. *J. Chem. Phys.*, 118(24):10890–10899, June 2003.

[39] C S Gudeman and R J Saykally. Velocity modulation infrared laser spectroscopy of molecular ions. *Annu. Rev. Phys. Chem.*, 35(1):387–418, 1984.

[40] Christopher Gudeman, Marianne Begemann, Jürgen Pfaff, and Richard Saykally. Velocity-modulated infrared laser spectroscopy of molecular ions: The ν_1 band of HCO^+. *Phys. Rev. Lett.*, 50(10):727–731, March 1983.

[41] Christopher S. Gudeman, Marianne H. Begemann, Jrgen Pfaff, and Richard J. Saykally. Velocity-modulated infrared laser spectroscopy of molecular ions: The ν_1 band of HCO^+. *Phys. Rev. Lett.*, 50(10):727–731, March 1983.

[42] D. T. Halfen and L. M. Ziurys. Laboratory detection of $FeCO^+$ ($X^4\Sigma^-$) by millimeter/submillimeter velocity modulation spectroscopy. *Astrophys. J.*, 657(1, Pt. 2):L61–L64, 2007.

[43] D. T. Halfen and L. M. Ziurys. Millimeter/submillimeter velocity modulation spectroscopy of FeO^+ ($X^6\Sigma^+$): Characterizing metal oxide cations. *Chem. Phys. Lett.*, 496(1-3):8–13, 2010.

[44] M. Havenith, M. Schneider, W. Bohle, and W. Urban. Sub-doppler faraday lmr spectroscopy: first applications to NO and DBr^+. *Molecular Physics: An International Journal at the Interface Between Chemistry and Physics*, 72(5):1149–1158, 1991.

[45] E. Herbst and W. Klempere. Formation and depletion of molecules in dense interstellar clouds. *Astrophys. J.*, 185(2):505–533, 1973.

[46] Eizi Hirota and Yasuki Endo. Microwave spectroscopy of hco+ and dco+ in excited vibrational states. *J. Mol. Spectrosc.*, 127(2):527 – 534, 1988.

[47] Chikako Ishibashi and Hiroyuki Sasada. Highly sensitive cavity-enhanced sub-doppler spectroscopy of a molecular overtone band with a 1.66 μm tunable diode laser. *Japanese Journal of Applied Physics*, 38(Part 1, No. 2A):920–922, 1999.

[48] Chikako Ishibashi and Hiroyuki. Sasada. Near-infrared laser spectrometer with sub-doppler resolution, high sensitivity, and wide tunability. a case study in the 1.65 μm region of ch3i spectrum. *J. Mol. Spectrosc.*, 200(1):147–149, 2000.

[49] M. F. Jagod, C. M. Gabrys, M. Rosslein, D. Uy, and T. Oka. Infrared-spectrum of CH_3^+ involving high rovibrational levels. *Can. J. Phys.*, 72(11-12):1192–1199, November 1994.

[50] E. R. Keim, M. L. Polak, J. C. Owrutsky, J. V. Coe, and R. J. Saykally. Absolute infrared vibrational band intensities of molecular-ions determined by direct laser-absorption spectroscopy in fast ion-beams. *J. Chem. Phys.*, 93(5):3111–3119, September 1990.

[51] Eric Roll Keim. *Infrared Laser Absorption Spectroscopy of Fast Ion Beams: Cluster Ions.* PhD thesis, University of California at Berkeley, July 1992.

[52] J. F. Kelly, R. L. Sams, T. A. Blake, M. Newburn, J. Moran, M. L. Alexander, and H. Kreuzer. A capillary absorption spectrometer for stable carbon isotope ratio ($^{13}C/^{12}C$) analysis in very small samples. *Rev. Sci. Instrum.*, 83(2):023101, 2012.

[53] William Klemperer. Carrier of the interstellar 89.190 GHz line. *Nat.*, 227(5264):1230–1230, September 1970.

[54] H. Kreckel, H. Bruhns, K. A. Miller, E. Wahlin, A. Davis, S. Hockh, and D. W. Savin. A simple double-focusing electrostatic ion beam deflector. *Rev. Sci. Instrum.*, 81(6):063304, June 2010.

[55] R. DE L. Kronig. On the theory of dispersion of x-rays. *J. Opt. Soc. Am.*, 12(6):547–556, June 1926.

[56] Valerio Lattanzi, Adam Walters, Brian J Drouin, and John C Pearson. Rotational spectrum of the formyl cation, HCO^+, to 1.2 THz. *Astrophys. J.*, 662(1):771–778, June 2007.

[57] Song Li, Rui Zheng, Guangming Huang, and Chuanxi. Duan. Mid-infrared diode laser spectroscopy of SO^+. *J. Mol. Spectrosc.*, 252(1):22–24, 2008.

[58] B. Lindgren, P. Royen, and M. Zackrisson. The rotational structure of the (8, 3) band of the $A_2\Pi_u$-$X_2\Sigma_g^+$ system of N_2^+ studied by velocity modulation laser spectroscopy. *J. Mol. Spectrosc.*, 146(2):343–350, 1991.

[59] C.Michael Lindsay, Ronald M. Rade Jr., and Takeshi Oka. Survey of H_3^+ transitions between 3000 and 4200 cm^{-1}. *J. Mol. Spectrosc.*, 210(1):51–59, November 2001.

[60] C.Michael Lindsay, Edmund T. White, and Takeshi Oka. Measurement of the H_3^+ destruction rate due to ambipolar diffusion in an AC positive column discharge. *Chem. Phys. Lett.*, 328(1 - 2):129 – 134, 2000.

[61] H Liszt and R Lucas. Mm-wave HCO^+, hcn and co absorption toward NGC+1052. *Astron. Astrophys.*, 428(2):445–450, December 2004.

[62] LS Ma, J Ye, P Dube, and JL Hall. Ultrasensitive frequency-modulation spectroscopy enhanced by a high-finesse optical cavity: theory and application to overtone transitions of C_2H_2 and C_2HD. *J. Opt. Soc. Am. B: Opt. Phys.*, 16(12):2255–2268, DEC 1999.

[63] Weiguang Ma, Aleksandra Foltynowicz, and Ove Axner. Theoretical description of doppler-broadened noise-immune cavity-enhanced optical heterodyne molecular spectroscopy under optically saturated conditions. *J. Opt. Soc. Am. B: Opt. Phys.*, 25(7):1144–1155, July 2008.

[64] P. Malara, P. Maddaloni, G. Gagliardi, and P. De Natale. Absolute frequency measurement of molecular transitions by a direct link to a comb generated around 3 μm. *Opt. Express*, 16(11):8242–8249, May 2008.

[65] D. Mazzotti, S. Borri, P. Cancio, G. Giusfredi, and P. De Natale. Low-power lamb-dip spectroscopy of very weak CO_2 transitions near 4.25 μm. *Opt. Lett.*, 27(14):1256–1258, July 2002.

[66] A. B. Meinel. A new band system of N_2^+ in the infrared auroral spectrum. *Astrophys. J.*, 112:562–563, 1950.

[67] S N Milam, C Savage, L M Ziurys, and S Wyckoff. HCO^+ observations toward comet hale-bopp (C/1995 O1): Ion-molecule chemistry and evidence for a volatile secondary source. *Astrophys. J.*, 615(2):1054–1062, November 2004.

[68] Andrew A. Mills, Brian M. Siller, and Benjamin J. McCall. Precision cavity enhanced velocity modulation spectroscopy. *Chem. Phys. Lett.*, 501(1-3):1 – 5, 2010.

[69] Andrew A. Mills, Brian M. Siller, Michael W. Porambo, Manori Perera, Holger Kreckel, and Benjamin J. McCall. Ultra-sensitive high-precision spectroscopy of a fast molecular ion beam. *J. Chem. Phys.*, 135(22):224201, December 2011.

[70] John H. Moore, Christopher C. Davis, and Michael A. Coplan. *Building Scientific Aparatus*. Perseus Books, 2002.

[71] Christopher P. Morong, Jennifer L. Gottfried, and Takeshi Oka. as the benchmark for rigorous ab initio theory. *J. Mol. Spectrosc.*, 255(1):13–23, May 2009.

[72] Takeshi Oka. Observation of the infrared spectrum of H_3^+. *Phys. Rev. Lett.*, 45:531–534, Aug 1980.

[73] Takeshi Oka and Mary-Frances Jagod. Infrared spectrum of H as an astronomical probe. *J. Chem. Soc., Faraday Trans.*, 89(13):2147–2154, 1993.

[74] J. C. Owrutsky, E. R. Keim, J. V. Coe, and R. J. Saykally. Absolute IR intensities of the ν_1 bands of HN_2^+ and HCO^+ determined by direct laser-absorption spectroscopy in fast ion-beams. *J. Phys. Chem.*, 93(16):5960–5963, August 1989.

[75] J. C. Pearson, L. C. Oesterling, E. Herbst, and F. C. De Lucia. Pressure broadening of gas-phase molecular-ions at very-low temperature. *Phys. Rev. Lett.*, 75(16):2940–2943, October 1995.

[76] J. R. Peterson and J. T. Moseley. Time-of-flight determination of lifetimes of $N_2^+(A\Pi_u)$ - Meinel band system. *J. Chem. Phys.*, 58(1):172–177, 1973.

[77] J. R. Pierce. Rectilinear electron flow in beams. *J. Appl. Phys.*, 11(8):548–554, 1940.

[78] M. W. Porambo, B. M. Siller, J. M. Pearson, and B.J. McCall. Broadly tunable mid-infrared noise-immune cavity-enhanced optical heterodyne molecular spectrometer. *Opt. Lett.*, In Press:In Press, 2012.

[79] C. R. Purcell, R. Balasubramanyam, M. G. Burton, a. J. Walsh, V. Minier, M. R. Hunt-Cunningham, L. L. Kedziora-Chudczer, S. N. Longmore, T. Hill, I. Bains, P. J. Barnes, a. L. Busfield, P. Calisse, N. H. M. Crighton, S. J. Curran, T. M. Davis, J. T. Dempsey, G. Derragopian, B. Fulton, M. G. Hidas, M. G. Hoare, J.-K. Lee, E. F. Ladd, S. L. Lumsden, T. J. T. Moore, M. T. Murphy, R. D. Oudmaijer, M. B. Pracy, J. Rathborne, S. Robertson, a. S. B. Schultz, J. Shobbrook, P. a. Sparks, J. Storey, and T. Travouillion. A CH_3CN and HCO^+ survey towards southern methanol masers associated with star formation. *Mon. Not. R. Astron. Soc.*, 367(2):553–576, April 2006.

[80] M. B. Radunksy and R. J. Saykally. Electronic absorption-spectroscopy of molecular-ions in plasmas by dye-laser velocity modulation - the A-X system of N_2^+. *J. Chem. Phys.*, 87(2):898–901, July 1987.

[81] F. Roux, F. Michaud, and J. Verges. High-resolution fourier spectrometry of $^{14}N_2^+$ infrared emission spectrum: Extensive analysis of the b-a system. *J. Mol. Spectrosc.*, 97(2):253 – 265, 1983.

[82] C. Sanchez Contreras and R Sahai. Physical structure of the protoplanetary nebula CRL 618. ii. interferometric mapping of millimeter-wavelength HCN J = 1-0, HCO^+ J = 1-0, and continuum emission. *Astrophys. J.*, 602(2):960–977, February 2004.

[83] C. Savage, F. Dong, and Nesbitt D. J. Toward a quantum-mechanical understanding of the high-resolution infrared spectrum of CH_5^+. In *International Symposium on Molecular Spectroscopy 61st Meeting*, number talk TA5, Columbus, OH, June 2006. The Ohio State University.

[84] C. Savage and L. M. Ziurys. A millimeter/submillimeter velocity modulation spectrometer for studies of molecular ions. *Rev. Sci. Instrum.*, 76(4):043106, 2005.

[85] Florian M. Schmidt, Aleksandra Foltynowicz, Weiguang Ma, and Ove Axner. Fiber-laser-based noise-immune cavity-enhanced optical heterodyne molecular spectrometry for doppler-broadened detection of C_2H_2 in the parts per trillion range. *J. Opt. Soc. Am. B: Opt. Phys.*, 24(6):1392–1405, June 2007.

[86] Florian M. Schmidt, Aleksandra Foltynowicz, Weiguang Ma, Tomas Lock, and Ove Axner. Doppler-broadened fiber-laser-based NICE-OHMS - improved detectability. *Opt. Express*, 15(17):10822–10831, August 2007.

[87] I. Sherstov, S. Liu, C. Lisdat, H. Schnatz, S. Jung, H. Knockel, and E. Tiemann. Frequency measurements in the $b^3\Pi(0_u^+)$-$X^1\Sigma_g^+$ system of K_2. *European Physical Journal D*, 41(3):485–492, March 2007.

[88] Isak Silander, Patrick Ehlers, Junyang Wang, and Ove Axner. Frequency modulation background signals from fiber-based electro optic modulators are caused by crosstalk. *J. Opt. Soc. Am. B: Opt. Phys.*, 29(5):916–923, May 2012.

[89] B. M. Siller, A. A. Mills, and B. J. McCall. Cavity-enhanced velocity modulation spectroscopy. *Opt. Lett.*, 35(8):1266–1268, April 2010.

[90] Brian M. Siller, Michael W. Porambo, Andrew A. Mills, and Benjamin J. McCall. Noise immune cavity enhanced optical heterodyne velocity modulation spectroscopy. *Opt. Express*, 19(24):24822–24827, November 2011.

[91] Laura C. Sinclair, Kevin C. Cossel, Tyler Coffey, Jun Ye, and Eric A. Cornell. Frequency comb velocity-modulation spectroscopy. *Phys. Rev. Lett.*, 107:093002, Aug 2011.

[92] S. K. Stephenson and R. J. Saykally. Velocity modulation spectroscopy of ions. *Chem. Rev.*, 105(9):3220–3234, September 2005.

[93] Serena K. Stephenson and Richard J. Saykally. Terahertz laser velocity modulation spectroscopy of ions. *J. Mol. Spectrosc.*, 231(2):145–153, 2005.

[94] Z. D. Sun, Q. Liu, R. M. Lees, L. H. Xu, M. Y. Tretyakov, and V. V. Dorovskikh. Saturation-dip measurements in the $2\nu_2$ overtone band of OCS with a CO_2-laser/microwave-sideband spectrometer. *Appl. Phys. B*, 78(6):791–795, April 2004.

[95] Keisuke Takahata, Takumi Kobayashi, Hiroyuki Sasada, Yoshiaki Nakajima, Hajime Inaba, and Feng-Lei Hong. Absolute frequency measurement of sub-doppler molecular lines using a 3.4-mum difference-frequency-generation spectrometer and a fiber-based frequency comb. *Phys. Rev. A.*, 80(3):032518, September 2009.

[96] Matthew S. Taubman, Tanya L. Myers, Bret D. Cannon, and Richard M. Williams. Stabilization, injection and control of quantum cascade lasers, and their application to chemical sensing in the infrared. *Spectrochimica Acta Part A: Molecular and Biomolecular Spectroscopy*, 60(14):3457 – 3468, 2004.

[97] John S. Toll. Causality and the dispersion relation: Logical foundations. *Phys. Rev.*, 104:1760–1770, Dec 1956.

[98] N. J. van Leeuwen and A. C. Wilson. Measurement of pressure-broadened, ultraweak transitions with noise-immune cavity-enhanced optical heterodyne molecular spectroscopy. *J. Opt. Soc. Am. B: Opt. Phys.*, 21(10):1713–1721, October 2004.

[99] Luis Velilla, Bruno Lepetit, Alfredo Aguado, J. Alberto Beswick, and Miguel Paniagua. The H_3^+ rovibrational spectrum revisited with a global electronic potential energy surface. *J. Chem. Phys.*, 129(8):084307, 2008.

[100] H. Verbraak, A. K. Y. Ngai, S. T. Persijn, F. J. M. Harren, and H. Linnartz. Mid-infrared continuous wave cavity ring down spectroscopy of molecular ions using an optical parametric oscillator. *Chem. Phys. Lett.*, 442(1-3):145–149, July 2007.

[101] W. D. Watson. The rate of formation of interstellar molecules by ion-molecule reactions. *Astrophys. J.*, 183:L17, July 1973.

[102] S. L. W. Weaver, M. B. Wiczer, B. Negru, J. P. DiGangi, B. A. Tom, and B. J. McCall. Continuous-wave cavity ringdown spectroscopy of the N_2^+ Meinel system (2,1) band. *J. Mol. Spectrosc.*, 249(1):14–22, May 2008.

[103] G. K. Wertheim, M. A. Butler, K. W. West, and D. N. E. Buchanan. Determination of the gaussian and lorentzian content of experimental line shapes. *Rev. Sci. Instrum.*, 45(11):1369–1371, 1974.

[104] C. M. Western. Pgopher, a program for simulating rotational structure. http://pgopher.chm.bris.ac.uk, July 2009.

[105] E. T. White, J. Tang, and T. Oka. CH_5^+: The infrared spectrum observed. *Science*, 284(5411):135–137, April 1999.

[106] E. A. Whittaker, M. Gehritz, and G. C. Bjorklund. Residual amplitude-modulation in laser electro-optic phase modulation. *Journal of the Optical Society of America B*, 2(8):1320–1326, 1985.

[107] William Wing, George Ruff, Willis Lamb, and Joseph Spezeski. Observation of the infrared spectrum of the hydrogen molecular ion HD^+. *Phys. Rev. Lett.*, 36(25):1488–1491, June 1976.

[108] N. C. Wong and J. L. Hall. Servo control of amplitude modulation in frequency-modulation spectroscopy: demonstration of shot-noise-limited detection. *J. Opt. Soc. Am. B: Opt. Phys.*, 2(9):1527–1533, Sep 1985.

[109] R. Woods, Thomas Dixon, Richard Saykally, and Peter Szanto. Laboratory microwave spectrum of HCO^+. *Phys. Rev. Lett.*, 35(19):1269–1272, November 1975.

[110] Ling Wu, Xiaohua Yang, and Yangqin. Chen. Rotational analysis of the (4, 8) band in the A-X system of $^{35}Cl_2^+$. *Journal of Quantitative Spectroscopy & Radiative Transfer*, 109(9):1586–1589, 2008.

[111] Y. D. Wu, J. W. Ben, L. Li, L. J. Zhen, Y. Q. Chen, and X. H. Yang. Study of (2,0) band of $A^2\Pi_u$ - $X^2\Sigma_g^+$ system of N_2^+ by optical heterodyne detected velocity modulation spectroscopy. *Chin. J. Chem. Phys.*, 20(3):285–290, June 2007.

[112] Yandan Wu, Xiaohua Yang, Yingchun Guo, and Yangqin. Chen. Rotational analysis of the (3,6) band in the comet-tail (A2-X2) system of CO^+. *J. Mol. Spectrosc.*, 248(1):81–84, 2008.

[113] Jun Ye. *Ultrasensitive high resolution laser spectroscopy and its application to optical frequency standards.* Dissertation, University of Colorado Department of Physics, April 1997.

[114] Jun Ye, Long-Sheng Ma, and John L. Hall. Ultrasensitive detections in atomic and molecular physics: demonstration in molecular overtone spectroscopy. *J. Opt. Soc. Am. B: Opt. Phys.*, 15(1):6–15, Jan 1998.

[115] Jun Ye, Long-Sheng Ma, and John L. Hall. High-resolution frequency standard at 1030 nm for Yb:YAG solid-state lasers. *J. Opt. Soc. Am. B: Opt. Phys.*, 17(6):927–931, Jun 2000.

[116] Rui Zheng, Rui-Bo Wang, Song Li, Guang-Ming Huang, and Chuan-Xi. Duan. Extended measurement of the ν_2 (1^- - 0^+) band of H_3O^+ by mid-infrared diode laser spectroscopy. *Chin. Phys. Lett.*, 24(9):2569–2571, 2007.